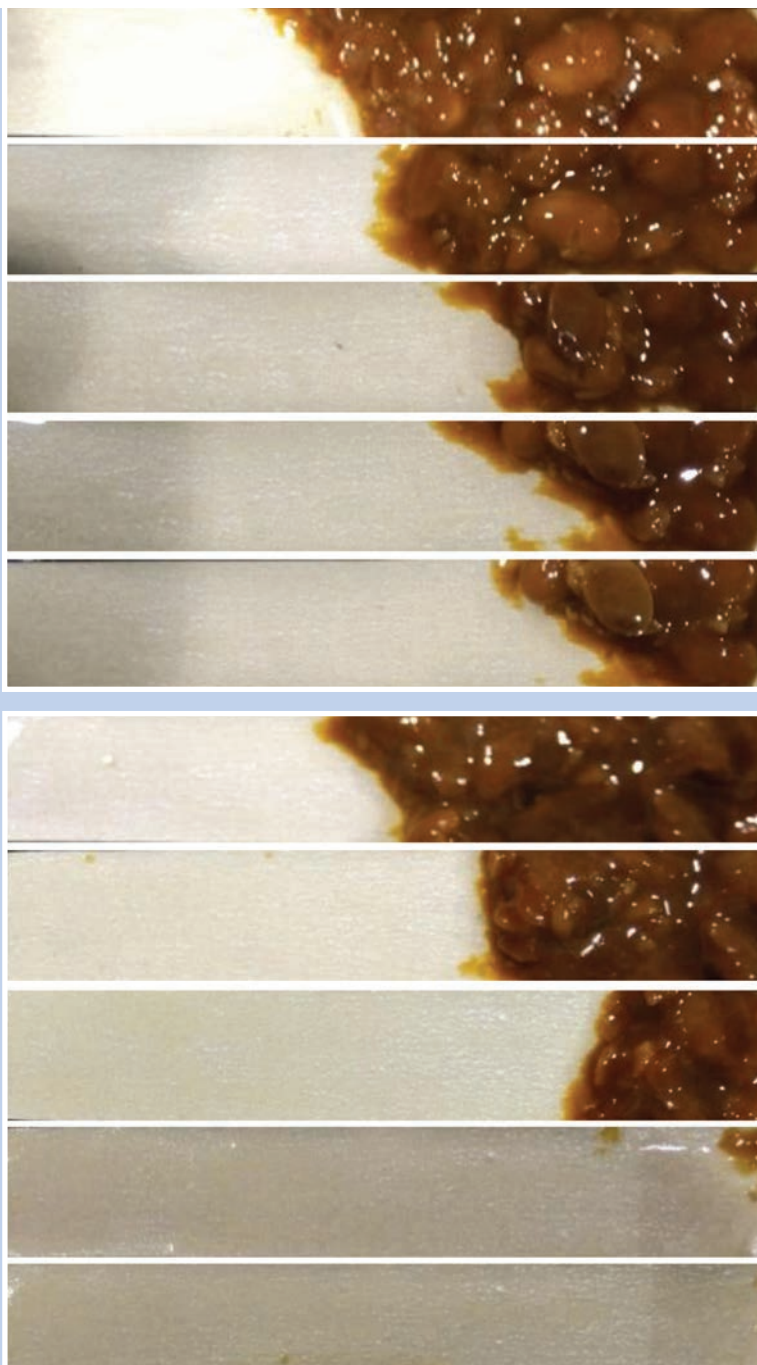




Strojniški vestnik

Journal of Mechanical Engineering

no. **3**
year **2021**
volume **67**



Strojniški vestnik – Journal of Mechanical Engineering (SV-JME)

Aim and Scope

The international journal publishes original and (mini)review articles covering the concepts of materials science, mechanics, kinematics, thermodynamics, energy and environment, mechatronics and robotics, fluid mechanics, tribology, cybernetics, industrial engineering and structural analysis.

The journal follows new trends and progress proven practice in the mechanical engineering and also in the closely related sciences as are electrical, civil and process engineering, medicine, microbiology, ecology, agriculture, transport systems, aviation, and others, thus creating a unique forum for interdisciplinary or multidisciplinary dialogue.

The international conferences selected papers are welcome for publishing as a special issue of SV-JME with invited co-editor(s).

Editor in Chief

Vincenc Butala

University of Ljubljana, Faculty of Mechanical Engineering, Slovenia

Technical Editor

Pika Škraba

University of Ljubljana, Faculty of Mechanical Engineering, Slovenia

Founding Editor

Bojan Kraut

University of Ljubljana, Faculty of Mechanical Engineering, Slovenia

Editorial Office

University of Ljubljana, Faculty of Mechanical Engineering

SV-JME, Aškerčeva 6, SI-1000 Ljubljana, Slovenia

Phone: 386 (0)1 4771 137

Fax: 386 (0)1 2518 567

info@sv-jme.eu, <http://www.sv-jme.eu>

Print: Demat d.o.o., printed in 250 copies

Founders and Publishers

University of Ljubljana, Faculty of Mechanical Engineering, Slovenia

University of Maribor, Faculty of Mechanical Engineering, Slovenia

Association of Mechanical Engineers of Slovenia

Chamber of Commerce and Industry of Slovenia,

Metal Processing Industry Association

President of Publishing Council

Mitjan Kalin

University of Ljubljana, Faculty of Mechanical Engineering, Slovenia

Vice-President of Publishing Council

Bojan Dolšak

University of Maribor, Faculty of Mechanical Engineering, Slovenia

International Editorial Board

Kamil Arslan, Karabuk University, Turkey

Hafiz Muhammad Ali, King Fahd U. of Petroleum & Minerals, Saudi Arabia

Josep M. Bergada, Politechnical University of Catalonia, Spain

Anton Bergant, Litostroj Power, Slovenia

Miha Boltežar, University of Ljubljana, Slovenia

Filippo Cianetti, University of Perugia, Italy

Janez Diaci, University of Ljubljana, Slovenia

Anselmo Eduardo Diniz, State University of Campinas, Brazil

Igor Emri, University of Ljubljana, Slovenia

Imre Felde, Obuda University, Faculty of Informatics, Hungary

Imre Horvath, Delft University of Technology, The Netherlands

Aleš Hribernik, University of Maribor, Slovenia

Soichi Ibaraki, Kyoto University, Department of Micro Eng., Japan

Julius Kaplunov, Brunel University, West London, UK

Iyas Khader, Fraunhofer Institute for Mechanics of Materials, Germany

Jernej Klemenc, University of Ljubljana, Slovenia

Milan Kljajin, J.J. Strossmayer University of Osijek, Croatia

Peter Krajnik, Chalmers University of Technology, Sweden

Janez Kušar, University of Ljubljana, Slovenia

Gorazd Lojen, University of Maribor, Slovenia

Darko Lovrec, University of Maribor, Slovenia

Thomas Lübben, University of Bremen, Germany

George K. Nikas, KADMOS Engineering, UK

Tomaž Pepelnjak, University of Ljubljana, Slovenia

Vladimir Popović, University of Belgrade, Serbia

Franci Pušavec, University of Ljubljana, Slovenia

Mohammad Reza Safaei, Florida International University, USA

Marco Sortino, University of Udine, Italy

Branko Vasić, University of Belgrade, Serbia

Arkady Voloshin, Lehigh University, Bethlehem, USA

General information

Strojniški vestnik – Journal of Mechanical Engineering is published in 11 issues per year (July and August is a double issue).

Institutional prices include print & online access: institutional subscription price and foreign subscription €100,00 (the price of a single issue is €10,00); general public subscription and student subscription €50,00 (the price of a single issue is €5,00). Prices are exclusive of tax. Delivery is included in the price. The recipient is responsible for paying any import duties or taxes. Legal title passes to the customer on dispatch by our distributor. Single issues from current and recent volumes are available at the current single-issue price. To order the journal, please complete the form on our website. For submissions, subscriptions and all other information please visit: <http://www.sv-jme.eu>.

You can advertise on the inner and outer side of the back cover of the journal. The authors of the published papers are invited to send photos or pictures with short explanation for cover content.

We would like to thank the reviewers who have taken part in the peer-review process.

The journal is subsidized by Slovenian Research Agency.

Strojniški vestnik - Journal of Mechanical Engineering is available on <https://www.sv-jme.eu>.



Cover:

The self-excited pulsed air-water jet offers many advantages over other jets and has a large number of practical and industrial applications. Experimental testing of its cleaning performance is necessary. The cleaned area ratio was calculated from acquired images by using image analysis software through image pre-processing, greying, image segmentation, calibration, and area calculation.

Image courtesy:

Research Center of Fluid Machinery Engineering and Technology, Jiangsu University, Zhenjiang, China

ISSN 0039-2480, ISSN 2536-2948 (online)

© 2021 Strojniški vestnik - Journal of Mechanical Engineering. All rights reserved. SV-JME is indexed / abstracted in: SCI-Expanded, Compendex, Inspec, ProQuest-CSA, SCOPUS, TEMA. The list of the remaining bases, in which SV-JME is indexed, is available on the website.

Contents

Strojniški vestnik - Journal of Mechanical Engineering
volume 67(2021 , number 3
Ljubljana, March 2021
ISSN 0039-2480

Published monthly

Papers

- Yong Wang, Xiaolin Wang, Zilong Zhang, Yu Li, Houlin Liu, Xiang Zhang, Marko Hočevar: Optimization of a Self-Excited Pulsed Air-Water Jet Nozzle Based on the Response Surface Methodology 75
- Manuel Javier Rosel Solis, José Omar Dávalos Ramírez, Javier Molina Salazar, Juan Antonio Ruiz Ochoa, Antonio Gómez Roa: Optimization of Running Blade Prosthetics Utilizing Crow Search Algorithm Assisted by Artificial Neural Networks 88
- Omar Dávalos, Uzziel Caldiño-Herrera, Delfino Cornejo-Monroy, Oscar Tenango-Pirin, Juan Carlos García, M.A. Basurto-Pensado: Reduction of Stresses and Mass of an Engine Rubber Mount Subject to Mechanical Vibrations 101
- Bin Wang, Chenxiao Yan, Jubo Li, Peiyao Feng, Shuaipu Wang, Shuo Chen, Jianxin Su: Residual Stress and Deformation Analysis in Machining Split Straight Bevel Gears 114
- Sandino Torres, Roberto Ortega, Pablo Acosta, Edison Calderón: Hot Incremental Forming of Biocomposites Developed from Linen Fibres and a Thermoplastic Matrix 123

Optimization of a Self-Excited Pulsed Air-Water Jet Nozzle Based on the Response Surface Methodology

Yong Wang¹ – Xiaolin Wang¹ – Zilong Zhang¹ – Yu Li¹ – Houlin Liu^{1,*} – Xiang Zhang² – Marko Hočevar³

¹Jiangsu University, Research Center of Fluid Machinery Engineering and Technology, China

²Xihua University, Key Laboratory of Fluid and Power Machinery, China

³University of Ljubljana, Faculty of Mechanical Engineering, Slovenia

A self-excited pulsed air-water jet (SEPAWJ) offers many advantages over other jets and has a large number of practical and industrial applications. In order to take better advantage of the SEPAWJ, response surface methodology (RSM) models were established with the experimental impact force characteristics as the dependent variable and three key nozzle parameters as the independent variable. Single and coupling factor effects of these three parameters (oscillation chamber length, oscillation chamber height, and diameter of the downstream nozzle) on performance of nozzle are analysed, and the structural parameters of optimum performance are calculated using RSM models. The external flow field, impact force and cleaning performance of SEPAWJ before and after optimization are analysed and compared experimentally. It is found that the significance levels of established average impact force and impact force amplitude RSM models are lower than 0.05, and their error ratios between calculation and experiment under the optimum construction are both less than 5 %, which confirms their considerable reliability. Meanwhile, the final large water mass of optimized SEPAWJ is formed much earlier, and is more intensive and more concentrated. Compared with the original SEPAWJ nozzle, the impact force and impact force amplitude of optimized SEPAWJ nozzle are increased by 52.00 % and 38.26 %, respectively. In addition, the cleaned area ratio of nozzle before and after optimization is 76 % and 100 % at 50 seconds, respectively, with an increase of 22.4 %.

Keywords: multiphase flow, impact force, cleaning performance, optimization, pulsed jet

Highlights

- The collapse of air bubbles and water surface tension transform continuous air-water mixed jet to discrete water masses with different speeds.
- At the same mass flow rate and time duration, bigger water masses from a pulsed jet offer larger volume and less number water masses which improves impact force amplitude and lowers impact force frequency.
- Multiphase periodic flow in the oscillation chamber of the pulsed air-water jet nozzle consists of shear layer flow formation, air suction from holes, air-water vorticity ring formation, air bubble breakage, and air mixing with the main stream.
- A self-excited pulsed air-water jet nozzle is optimized on the basis of Response Surface Methodology.
- Models are established with the experimental impact force characteristics as the dependent variable and three geometric dimensions as the independent variable.

0 INTRODUCTION

The high energy enabled by breaking of a continuous jet into a series of pulses has been widely used. Guha et al. [1] experimentally, numerically and theoretically investigated the very high speed water jet (80 m/s to 200 m/s) cleaning process, and the pressure distribution on the cleaning surface was assessed. Li et al. [2] investigated the effects of nozzle inner surface roughness on the cavitation erosion characteristics of submerged cavitating jets through experiments to push the erosion capability to a maximum, Chahine et al. [3] studied the Helmholtz nozzle and concluded that when the jet pulse frequency is consistent with the cavity's natural frequency, resonance will occur and the jet intensity will be improved. Scholars have studied the mechanism of pulsed jets through theoretical and experimental methods. Its most significant characteristic is periodic ejected water

mass rather than continuous flow. Labus and Savanick determined that the peak value of pulsed air-water jet dynamic pressure is several times that of the steady and continuous water jet under the same working conditions, which greatly improves the cleaning effect. Researchers created many mechanical methods for producing high-energy water pulses repeatedly, such as rotating, reciprocating, or wobbling mechanisms. Glenn [5] mentioned an impulsive water cannon that can produce high energy. Grinspan and Gnanamoorthy [6] studied the high efficiency pulsed water jet acting on rock targets. Although these devices could drive large scale oscillations of the water flow and improve the erosion effect, they required high levels of mechanical maintenance which limits durability in harsh industrial environments. The complexity-related short life-time of the mentioned mechanical devices have prevented the development of a high-pressure pulsed water jet systems. However, "self-resonating

*Corr. Author's Address: Jiangsu University, Research Center of Fluid Machinery Engineering and Technology, Zhengjiang, China, 1429685398@qq.com

jet” can be generated by the instability of shear flow, which could produce pulsed jets. Dehkhoda and Hood [7] mentioned the Helmholtz oscillator, which can form self-excited pulsed water jets. The vortices generated by the disturbed shear layer are continuously formed, enhanced, and weakened. The energy of the oscillation disturbance will increase significantly when the frequency of the process equals the natural frequency of the oscillator.

Many researchers have studied the self-excited water pulsed jet in many aspects. Tang et al. [8] built an oscillation frequency model of jet on the basis of hydro-acoustics and fluid dynamics for better understanding the principle of increasing jet pressure amplitude. He found that the oscillation frequency increased while increasing pump pressure and decreased while increasing cavity length, while there was an optimum cavity-length corresponding to the pressure peak value of the SEPAWJ. Hu [9] discussed the correlation of time-frequency distribution between the cervix cavity pressure pulsation signal and the shock pressure pulse signal in self-excited pulsed jet nozzle. He focused on the time-frequency rule of the pressure pulse signal, especially the inherent characteristic of frequency component. In order to improve the performance of the self-resonating cavitating waterjet under ambient pressures, Li et al. [10] experimentally studied the effects of the nozzle inner surface roughness by impinging the jets on pure aluminium specimens at various standoff distances. In addition, Chen et al. [11] investigated and compared the spray atomization properties and droplet turbulence characteristics of a twin-fluid nozzle with and without a self-excited vibrating cavity through a phase doppler particle analyser. He found that the self-excited vibrating cavity profoundly influenced the droplet turbulence characteristics by affecting the variation of droplet oscillation. In the presence of a self-excited vibrating cavity, the spray cone angle and the droplet number concentration increased significantly. The results indicated the significant role of the self-excited vibrating cavity in promoting fluid atomization.

Furthermore, Hall and Ewing [12] estimated the instantaneous turbulent velocity field in a three-dimensional wall jet from the fluctuating wall pressure through a spectral linear stochastic estimation technique and found that the passage of the large-scale structures caused large, coherent lateral sweeps of fluid across the entire span of the wall jet. Besides, Li et al. [13] analysed effects of area discontinuity at nozzle inlet of Helmholtz oscillator and experimentally investigated it with respect to the axial pressure oscillations. It

was found that area discontinuity had a capacity of enhancing their peak, which largely depended on the inlet pressure and standoff distance. The enhancement decreased with increasing inlet pressure and only happened within small standoff distances. Oh and Cho [14] carried out experimental cutting tests with water pressure, traverse speed of nozzle, and abrasive feed rate, and the energy loss was expressed by the energy term. Thakur and Singh [15] summarized the research progress and integrated function of abrasive waterjet machining in terms of mechanism and machining performances by using mathematical modelling and optimization methods. Alsoufi et al. [16] studied the effect of abrasive waterjet machining parameters on the surface texture quality of Carrara marble, and determined that the abrasive waterjet cutting process offers better cut surface texture quality of Carrara marble when the parameter conditions are constant.

With the wider application of pulsed water jet in engineering, scholars found that the self-excited pulsed air-water jet performed better in some fields. Wang and Zhou [17] used out the air-water and pulsed jets to break rock by combination. They optimized the parameters of pulsed jet device structure and the results show that erosion effect had increased significantly.

Hu et al. [18] described a new way of generating pulsed air-water jet by entraining and mixing air into the cavity of a pulsed water jet nozzle based on the theory of hydro-acoustics and fluid dynamics. A theoretical model was built, which described the frequency characteristic of the pulsed air-water jet and aiming at gaining a better understanding of the nozzle for generating pulses. In addition, the experimental results on specimens impinged by the pulsed water jet and pulsed air-water jet showed that the erosion rate increased slightly with air addition within a certain range of cavity length.

It can be seen from the above that the self-excited pulsed air-water jet is a new type of efficient cleaning jet, which combines the advantages of different kinds of jets. The periodic high-intensity impact of self-excited pulsed air-water jet can quickly remove stains and its impact distribution is much wider, which significantly improves the cleaning effect.

In addition, the RSM is a statistical method to determine the optimum parameters, to solve the multivariate problems by using reasonable experimental design method, to obtain data through experiments and by using multivariate quadratic regression equation to obtain the functional relationship between factors. RSM was first proposed by Box and Wilson [19]. It is widely used in the fitting

field of physical experiments in medicine, chemical industry, food and mechanical engineering. Vyavahare et al. [20] studied the effects of dye concentration, time, pH, and temperature on sorption of malachite green (MG) dye using response surface methodology (RSM). Tang et al. [21] used the central composite design (CCD) and response surface methodology to optimize the working parameters of the sprinkler, and established multiple regression models, so that the vertical rocker sprinkler can achieve the best hydraulic performance in operation. Siddhant and Jignasa [22] investigated the optimum deposition conditions for preparation of copper zinc tin sulphur compounds (CZTS) thin films using the spray pyrolysis method based on the response surface methodology. Qi et al. [23] adopted Box Behnken's design combined with response surface methodology to investigate the effect of pH value, contact time, initial concentration, and other adsorption parameters on Th(IV) adsorption capacity. Khoshnamvand et al. [24] used response surface methodology to study the effects of Ciprofloxacin (CIP) concentration, CuO dosage and pH value on Chemical Oxygen Demand (COD) removal rate, and established a second-order model based on CIP concentration, CuO dosage and pH value. Öztürk and Kahraman [25] analysed and determined the best grinding parameters of glass by response surface method, and studied the relationship between grinding characteristics and surface roughness by Box Behnken design (BBD) to design the experiment. Gnanavelbabu and Saravanan [26] studied the abrasive water jet machining (AWJM) process for the machining of Grade 5 Titanium alloy through response surface methodology (RSM) and adopted BBD to optimize the abrasive water jet machining process.

Especially, in the aspect of the AWJ cutting, many scholars also use response surface method to study. Dani and Shah [27] used response surface methodology to study the effects of transverse velocity, water pressure, and tool spacing on the removal rate and surface roughness. Karakurt et al. [28] studied the effects of the abrasive waterjet operating variables on the kerf angle and the material properties were correlated with the kerf angle through response surface methodology. Gupta et al. [29] adopted the abrasive water jet cutting (AWJ) process to study experimental investigation parameters on kerf taper angles of makrana white marble through changing the water pressure, nozzle transverse speed and abrasive flow rate; analysis of variance (ANOVA) was used to determine the main statistically significant process factors affecting the kerf taper angle. Mohammad

and Jabari [30] studied the cooling of photovoltaic modules through multi-nozzle jet impingement cooling (JIC) system. The effects of the number of nozzles, their sizes (diameter), and the dimensionless nozzle-to-photovoltaic (PV) spacing on the overall performance of the JIC system were studied using a response surface methodology.

Many experiments are needed to study the influence of various factors on the performance of self-excited pulsed air-water jet nozzle and their relationship. The response surface methodology can shorten the optimization process with less experimental time compared with traditional optimization methods. In the present paper, SEPAWJ was applied to toilet nozzle, and the second-order mathematical model of RSM was established for the SEPAWJ characteristics of impact force characteristics (average impact force F , impact force amplitude ΔF) under different chamber and downstream nozzle parameters measured by experiments. The significance of the coefficients of the model and regression equation was tested. The influence of interaction items and single factors on the SEPAWJ impact characteristics was obtained. Structural parameters for optimum performance were calculated with RSM equations and the performance of the nozzle before and after optimization was compared experimentally. Comparison supplements the previous related research and provides useful information for better applications of SEPAWJ.

1 OPERATING PRINCIPLES OF A SEPAWJ NOZZLE

The SEPAWJ has a more pronounced cleaning effect than the continuous jet because of its periodic water mass delivery. The peak value of jet-forced pressure of the pulsed air-water jet is several times that of the continuous water jet under the same working conditions. Fig. 1 shows the operating principles of a nozzle producing SEPAWJ.

As shown in Fig. 1, the shear layer flow flows to the air holes on both sides of the chamber, which reduces the holes pressure to lower than atmospheric pressure. Air is sucked from the air holes and forms a series of discrete bubbles. The inclusion of bubbles to the fluids shear layer enables formation of air-water vorticity rings due to the confinement by the chamber wall. Some bubbles in air-water vorticity rings break up and produce pressure pulses. This results in small bubbles mixing into the main stream flow and causing pressure and velocity fluctuations. The air-mixed main stream flow passes through the downstream nozzle and eventually forms an air-water pulsed jet. As discussed, the series phenomena: "shear layer

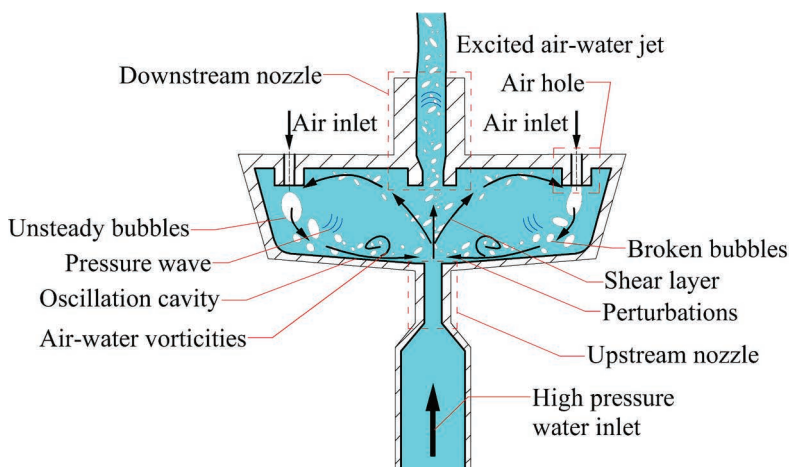


Fig. 1. Schematic diagram of a SEPAWJ nozzle and its operating principles

flow formation”, “air suction from holes”, “air-water vorticity rings formation”, “air bubble breakage”, and “air mixing with main stream” develop quasi-periodic operations of the pulsating air-water jet under certain working conditions.

around 10 cm distance from the downstream. All of this results in different speeds of individual segments. The faster segments catch up with the slower segments and eventually form a large water segment at around 15 cm from the downstream nozzle. Continuous occurrence of pulsed large water segments forms the SEPAWJ.

2 EXPERIMENTAL SETUP AND PROCEDURES

The design of the experimental SEPAWJ nozzle is shown in Fig. 3. The experimental SEPAWJ nozzle parameters before optimization are shown in Table 1. The nozzle is 3D-printed with photosensitive resin as material, which is waterproof and not easy to deform. The performance parameters of material are shown in Table 2.

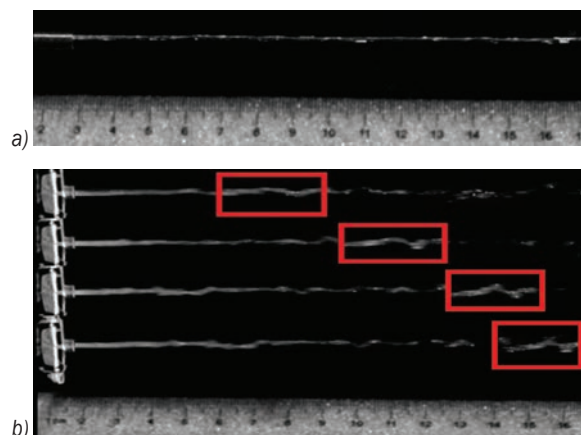


Fig. 2. Visualization of continuous jet and EPAWJ; a) continuous jet; b) EPAWJ

Fig. 2 shows visualization of the continuous jet and SEPAWJ. As shown in Fig. 2a, the continuous water jet is thin, straight, and stable for the entire observation length. Because of its stability, its cleaning area and the impact force amplitude are small. As shown in Fig. 2b, the air bubbles in the air-water jet collapse and the jet becomes unstable at 6 cm. Because non-stationary and random phenomena, like the uneven distribution of air bubbles in the entire jet, unstable and turbulent flow within the jet, pressure instabilities within the water jet, surface tension and the random air bubble collapse, the continuous air-water jet breaks into small discrete water segments at

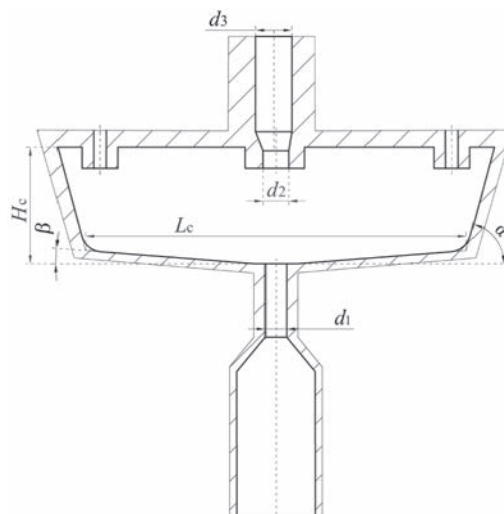


Fig. 3. Schematic diagram of the SEPAWJ nozzle

Table 1. The main structural parameters of the SEPAWJ nozzle before optimization

Parameter	Name	Size
d_1	Outlet diameter of upstream nozzle	1 mm
d_2	Inlet diameter of downstream nozzle	1.4 mm
d_3	Outlet diameter of downstream nozzle	1.7 mm
H_c	Oscillation chamber height	5.5 mm
L_c	Oscillation chamber length	16 mm
α	Inclination angle of oscillation chamber side wall	60°
β	Inclination angle of oscillation chamber bottom wall	4°

Table 2. The main performance parameters of the resin material

Heat distortion temperature	47 °C
Hardness	87
Tensile strength (fracture)	56 MPa
Tensile modulus	2800 MPa
Ductility (tensile)	4 %
Impact strength	25 J/m
Bending strength	84 MPa
Bending modulus	2490 MPa
Poisson's ratio	0.41

The experimental setup is arranged from several subsystems, indicated by different colours in Fig. 4; water supply and conditioning, nozzle, SEPAWJ cleaning evaluation, force measurement, flow visualization, and control systems.

As impact force is the most important evaluating indicator of a jet, its average impact force and impact force amplitude, as well as impact force frequency of fluctuations are essential to be measured and analysed for SEPAWJ performance evaluation under different working conditions and parameters. A miniature impact force sensor (model: LH-S09A) was used to measure the SEPAWJ impact force. It was mounted at a distance 150 mm away from the downstream nozzle outlet.

The size and shape of the discrete water segments formed within the discrete jet from the downstream nozzle outlet have a great influence on the cleaning performance. Therefore, flow field visualization was used to provide better understanding of the SEPAWJ characteristics LH-S09A performance under different nozzle structure parameters. A high-speed image acquisition system (camera model: MotionPro Y4) for capturing flow field was used for the SEPAWJ jet evaluation.

Experimental testing of the cleaning performance of the SEPAWJ is necessary and the steps to do so are as follows:

1. Evenly apply 10 g soybean paste as a dirt on a 100 mm × 20 mm water-resistant sandpaper (model: P1500).
2. The direction of nozzle outlet is at 25 degrees angle relative to the paper surface placed horizontally. The distance between nozzle outlet and sandpaper is 15 cm.

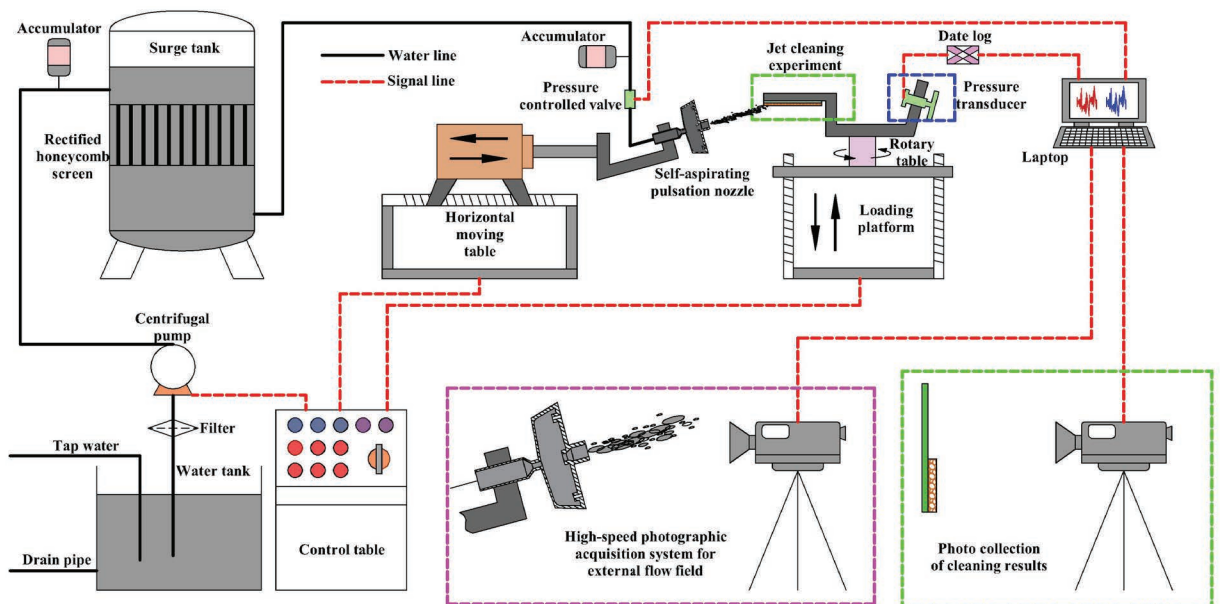


Fig. 4. Schematic diagram of the experimental setup

3. The image of residual dirt is acquired every 10 seconds for measurement of cleaned area ratio.
4. The cleaned area ratio was calculated from acquired images by using image analysis software through image pre-processing, greying, image segmentation, calibration, and area calculation.

Fig. 5 shows residual dirt image before and after the grey level thresholding by image analysis software.

Furthermore, in order to reduce the influence of testing system pressure amplitude, a centrifugal pump is used as pumping device and a surge tank and two accumulators are installed. The pressure controlled valve in upstream of the nozzle ensures that the dynamic pressure of the nozzle inlet is stable at 0.12 MPa.



Fig. 5. Before and after the gray processing of residual dirt area by image analysis software; a) before the grey processing of residual dirt area; b) after the grey processing of residual dirt area

3 RESULTS AND ANALYSIS

3.1 Design of Experiment and Measurement Results

Tang et al. [8] compared self-excited oscillation pulsed jet and continuous jet for time domain impact characteristics under the same inlet pressure and mass flow rate. They found that the impact force amplitude of continuous jet is small and that of the self-excited oscillation pulsed jet is such significant, although the average impact force of self-excited oscillation pulsed jet is slightly smaller because of energy lost from gas bubbles breakings and associated turbulent losses. The average impact force and impact force amplitude are important parameters in evaluating a jet nozzle.

Based on our previous research, it was found that the oscillation chamber length, oscillation chamber height and diameter of the downstream nozzle each have a sensitive effect on the average impact force and impact force amplitude of the jet nozzle separately. However, single factor analysis has some disadvantages in the optimization; for example, it needs a lot of experiments and the coupling effect of three parameters are unknown.

The RSM enables seeing how changes to each input parameter affect a selected output parameter, showing the coupling relationship between variables and responses. The RSM, especially the BBD used in this research, is a technique in which orthogonal arrays are used to investigate design parameters.

Table 3. Initial design parameters and constraint values

Quantity	Lower value [mm]	Base value [mm]	Largest value [mm]
Inlet diameter of upstream nozzle	1.2	1.4	1.6
Chamber length	12	16	18
Chamber height	5.1	5.5	5.9

As a result, in this paper, the average impact force F and impact force amplitude ΔF were selected as target dependent variables to establish RSM model respectively and oscillation chamber length, oscillation chamber height and diameter of the downstream nozzle are taken as experimental variables. The initial design parameters and constraint values are shown in Table 3.

According to the initial design parameters and selected constraint values presented in Table 3, 17 test cases were obtained by Box-Behnken method in Software Design-Expert 10.0, and the average impact force F and impact force amplitude ΔF for each test scheme were obtained experimentally, as shown in Table 4.

3.2 Average Impact Force RSM Model

An ANOVA, which a data mining technique, is carried out to differentiate the contributions to the variance of the response surface from the model. To evaluate the effect of each design variable, the total variance of the model is decomposed into that of each design variable and their interactions. This method is used to identify unnecessary terms in model function.

Table 5 shows the RSM summary of the RSM model and ANOVA for average impact force. For the established average impact force of the RSM model, the significance levels of inlet diameter of downstream nozzle (A) and chamber length (B) are less than 0.01, which means that these two single factors have a very significant effect on average impact force F . Similarly, the significant level of the interaction term (AB) is less than 0.05, which indicates that it has a significant coupling effect on the average impact force F .

The significance level of a certain item is inversely proportional to the influence level of the item on the average strike force. Therefore, the order

Table 4. Experimental variables and obtained results

No.	Downstream nozzle inlet diameter A [mm]	Chamber length B [mm]	Chamber height C [mm]	Average impact force F [N]	Impact force amplitude ΔF [N]
1	1.6	20	5.5	0.0942	0.0121
2	1.4	16	5.5	0.1361	0.0163
3	1.4	12	5.9	0.1145	0.0103
4	1.2	16	5.1	0.1013	0.0148
5	1.2	16	5.9	0.0948	0.0131
6	1.6	12	5.5	0.0545	0.0088
7	1.6	16	5.9	0.0923	0.0115
8	1.4	12	5.1	0.1184	0.0113
9	1.4	16	5.5	0.1361	0.0163
10	1.4	16	5.5	0.1361	0.0163
11	1.6	16	5.1	0.0939	0.0124
12	1.4	20	5.1	0.1348	0.0159
13	1.4	16	5.5	0.1361	0.0163
14	1.2	20	5.5	0.1074	0.0143
15	1.4	20	5.9	0.1194	0.0151
16	1.4	16	5.5	0.1361	0.0163
17	1.2	12	5.5	0.0895	0.0095

of the influence of single factors the average impact force F is: chamber length (B) > inlet diameter of downstream nozzle (A) > chamber height (C). The order of the influence of interaction items on the average impact force F is: downstream nozzle and chamber height (AC) > chamber length and chamber height (BC) > downstream nozzle and chamber length (AB).

Table 5. Summary of RSM model and ANOVA for average impact force

Source	Sum of squares	Degrees of freedom	Mean square	Significance level (P -value)
Model	8.225E-003	9	9.139E-004	0.0002
A	6.680E-004	1	6.680E-004	0.0039
B	6.827E-004	1	6.827E-004	0.0037
B	1.748E-004	1	1.748E-004	0.0472
AB	1.796E-004	1	1.796E-004	0.0444
AC	5.550E-005	1	5.550E-005	0.2622
BC	3.306E-005	1	3.306E-005	0.3779
Residual	2.613E-004	7	3.732E-005	
Lack of fit	2.613E-004	3	8.708E-005	
Pure error	0.000	4	0.000	
Cor Total	8.486E-003	16		

Fig. 6 shows the average impact force as a function of interaction items consisting of the downstream nozzle inlet diameter, chamber length, and chamber height. The interaction term (AB) consisting of the length of downstream nozzle and

chamber length has a very significant effect on the average impact force, while the other two interaction terms are less significant. Therefore, the parameters of downstream nozzle inlet diameter and chamber length are more critical for obtaining larger average impact force.

According to the response surface regression equation, when the downstream nozzle inlet diameter is 1.37 mm, the chamber length is 18.12 mm, and the chamber height is 4.80 mm, the average impact force is expected to reach the maximum value of 0.1434 N.

The RSM equation of average impact force F is as follows:

$$\begin{aligned}
 F = & +0.14 - 0.009138A + 0.009238B \\
 & - 0.004675C + 0.0067AB + 0.003725AC \\
 & - 0.002875BC - 0.036A^2 - 0.012B^2 \\
 & - 0.00195C^2.
 \end{aligned} \quad (1)$$

It can be seen from Table 5 that the regression model $P = 0.0002 < 0.01$ shows that the model has a very significant impact on the impact force F , and can well describe the relationship between the structural parameters and the impact force F .

3.3 Average Impact Force Amplitude of the RSM Model

The response surface regression equation of impact force amplitude ΔF is as follows:

significant impact on the impact force amplitude, and can well describe the relationship between the structural parameters and the impact amplitude .

Table 6. Summary of RSM model and ANOVA for impact force amplitude

Source	Sum of squares	Degrees of freedom	Mean square	Significance level
Model	1.098E-004	9	1.220E-005	< 0.0001
<i>A</i>	5.951E-006	1	5.951E-006	< 0.0001
<i>B</i>	3.828E-005	1	3.828E-005	< 0.0001
<i>AB</i>	5.625E-007	1	5.625E-007	0.0204
<i>AC</i>	1.600E-007	1	1.600E-007	0.1557
<i>BC</i>	1.000E-008	1	1.000E-008	0.7027
Residual	4.425E-007	7	6.321E-008	
Lack of fit	4.425E-007	3	1.475E-007	
Pure error	0.000	4	0.000	
Cor Total	1.103E-004	16		

Table 6 shows the summary of RSM model and ANOVA for impact force amplitude. For the established impact force amplitude RSM model, the significant level of inlet diameter of downstream nozzle (*A*), chamber length (*B*) and chamber height (*C*) are less than 0.01 which means that these three single factors have a very significant effect on impact force amplitude ΔF . Similarly, the significant level of the interaction terms (*AB*) is less than 0.05, which indicates that only it has a significant effect on the impact force amplitude ΔF .

The significance level of a certain item is inversely proportional to the influence level of the item on the average impact force. Therefore, the order of the influence of single factors the impact force amplitude ΔF is: inlet diameter of downstream nozzle (*A*) = chamber length (*B*) > chamber height (*C*). The order of the influence of interaction items on the average impact force *F* is: inlet diameter of downstream nozzle and chamber length (*AB*) > inlet diameter of downstream nozzle and chamber height (*AC*) > chamber length and chamber height (*BC*).

Fig. 7 shows the impact force amplitude as a function of interaction items consisting of the downstream nozzle inlet diameter, chamber length and chamber height. The interaction term (*AB*) consisting of the length of downstream nozzle and combustor has a very significant effect on the average impact force, while the other interaction terms are less significant. Therefore, the parameters of downstream nozzle inlet diameter and chamber length are more critical for obtaining larger average impact force.

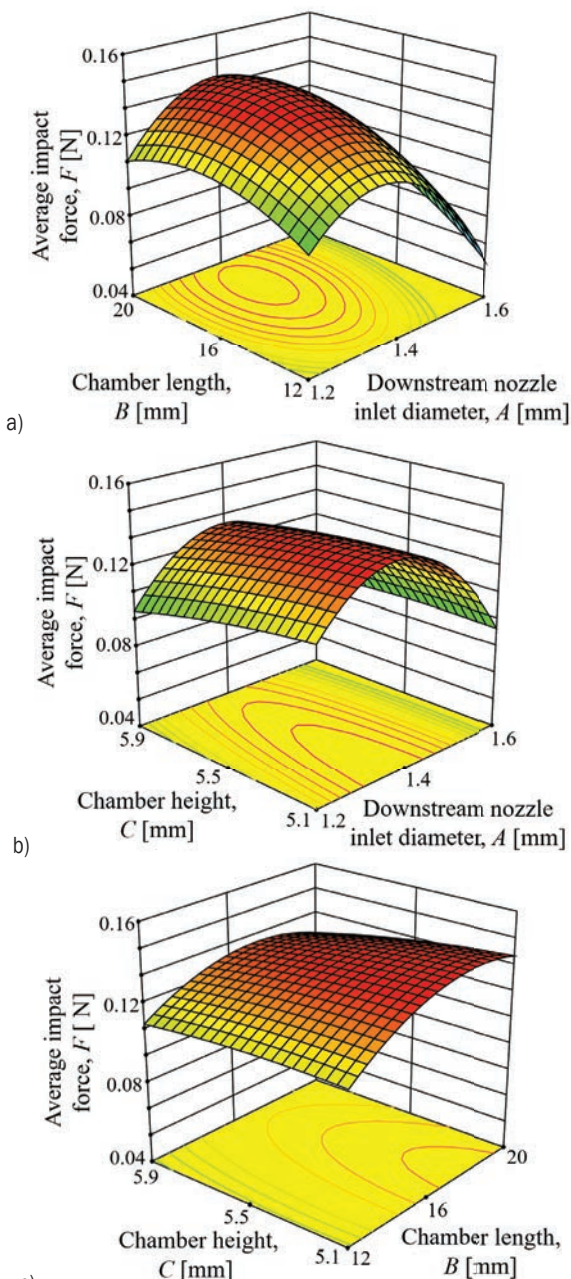


Fig. 6. Average impact force *F* as a function of interaction items; a) Interaction item of *A* and *B*; b) Interaction item of *A* and *C*; c) Interaction item of *B* and *C*

$$\begin{aligned} \Delta F = & +0.016 - 0.0008625A + 0.002188B \\ & - 0.00055C - 0.000375AB + 0.0002AC \\ & + 0.00005BC - 0.002663A^2 - 0.002463B^2 \\ & - 0.0006875C^2, \end{aligned} \tag{2}$$

It can be seen from Table 6 that the regression model $P < 0.0001$ shows that the model has a very

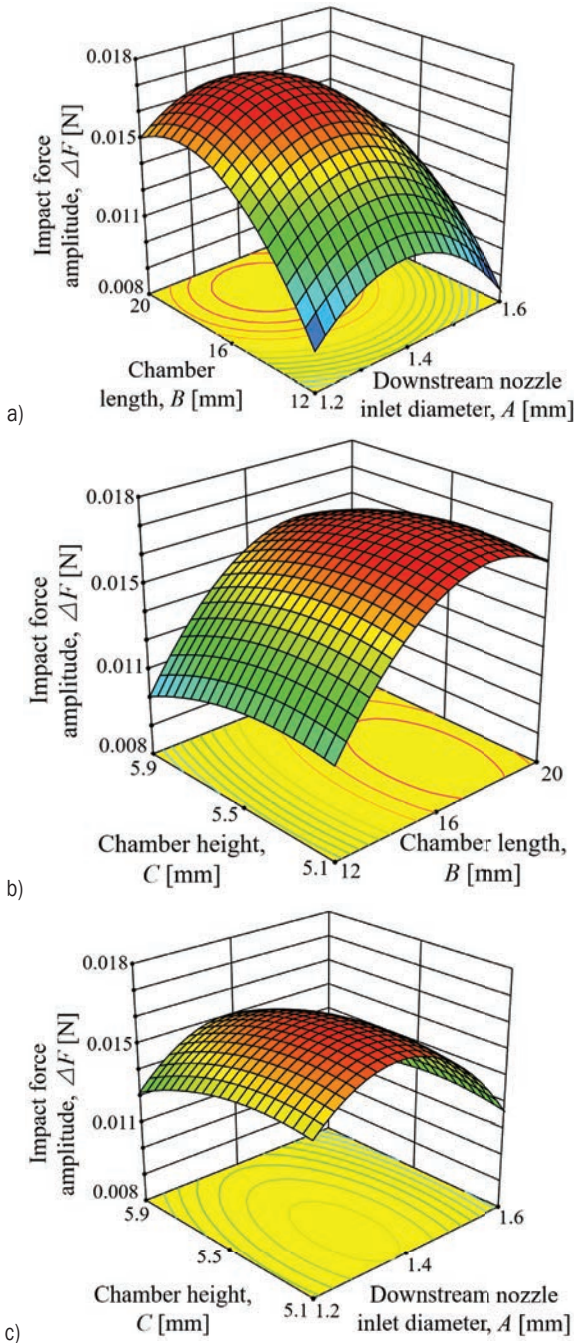


Fig. 7. Impact force amplitude ΔF as a function of interaction items; a) Interaction item of A and B; b) Interaction item of B and C; c) Interaction item of A and C

According to the response surface regression equation, when the downstream nozzle inlet diameter is 1.36 mm, the chamber length is 17.82 mm, and the chamber height is 5.33 mm, the impact force amplitude is expected to reach the maximum value of 0.0167 N.

3.4 Optimized Design Parameters

To optimize both the average impact force value and the impact force amplitude value, the average value of chamber lengths when the average impact force value and the impact force amplitude value reach their maximum is taken as the optimized dimension of chamber length. The chamber height and the diameter of downstream nozzle are obtained by the same method, as shown in Table 7.

Table 7. Optimized dimensions

Parameters	Maximum average impact force	Maximum impact force amplitude	Average
Outlet diameter of upstream nozzle [mm]	1.37	1.36	1.365
Chamber length [mm]	18.12	17.82	17.97
Chamber height [mm]	4.80	5.33	5.065

3.5 Flow Visualization

The pulsed water mass formed by SEPAWJ can cause strong strike force pulse, which greatly improves the cleaning performance. Fig. 8 shows the external flow field diagram of SEPAWJ before and after optimization.

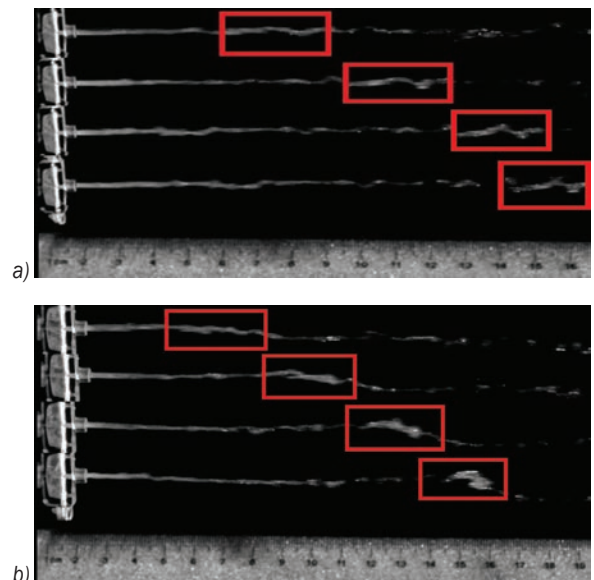


Fig. 8. External flow field diagram of SEPAWJ before and after optimization; a) flow visualization of original SEPAWJ nozzle; b) flow visualization of optimized SEPAWJ nozzle

Because air bubbles mixed in the jet collapse and water has surface tension in the air environment, the continuous air-water jet gradually forms small discrete water masses with different speeds. The faster small water masses will catch up with the slower small water masses and form to one large water mass. As can be seen from the external flow field diagram of original SEPAWJ in Fig. 8a, the final large water mass is formed near 16 cm from the nozzle exit, and it is not really concentrated and does not form a spherical shape. As shown in Fig. 8a, in the external flow field diagram of optimized SEPAWJ nozzle, the large water mass is formed close to the nozzle outlet at around 12 cm from the nozzle exit.

As it continues downstream, the water mass becomes concentrated and ultimately forms near spherical water mass in location around 14.5 cm from the nozzle exit with possessing improved cleaning capabilities.

3.6 Analysis of Impact Force

Fig. 9 shows the time and frequency domain diagram of SEPAWJ impact force before and after

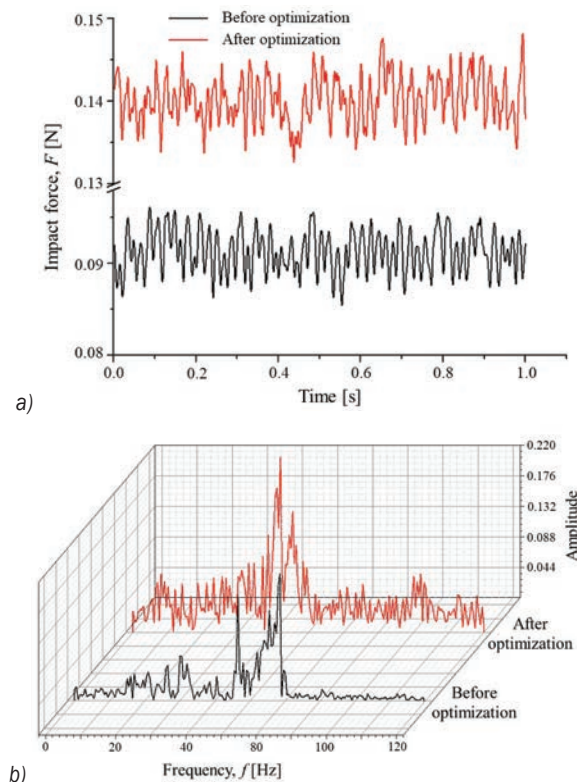


Fig. 9. Time and frequency domain diagram of SEPAWJ impact force before and after optimization; a) time domain diagram; b) frequency domain diagram

optimization; it can be seen that the value of average impact force and impact force amplitude are obviously improved for the optimized nozzle, which indicates that the cleaning performance of the optimized nozzle should be greater.

Furthermore, for the optimized nozzle, the impact force intensity of fluctuations exhibits a peak in a lower frequency region around 40 Hz. At the same mass flow rate and duration, bigger water masses definitely means less number of water masses which improves impact force amplitude and lower impact force frequency.

Table 8 shows the comparison of average impact force and impact force amplitude before and after optimization. For the SEPAWJ optimized nozzle, the average impact force is 0.1403 N and the impact force amplitude is 0.0159, which are 52.00 % and 38.26 % higher than that of the original nozzle, respectively. This means that the impact performance of the SEPAWJ nozzle has been remarkably improved.

Table 8. Comparison of average impact force and impact force amplitude before and after optimization

Value	Average impact force F	Impact force amplitude ΔF
Original [N]	0.0923	0.0115
Optimized [N]	0.1403	0.0159
Increase [%]	52.00	38.26

Table 9. Comparison of impact force between the experiment and RSM

Result	Average impact force F	Impact force amplitude ΔF
RSM model value [N]	0.1426	0.0167
Experimental value [N]	0.1403	0.0159
Error [%]	1.64	4.79

Comparison between experimental and predicted values of the average impact force value and the impact force amplitude value are shown in Table 9. The impact force and impact force amplitude errors of prediction and experiment are both less than 5 %, which means that the response surface functions are basically accurate.

3.6 Analysis of Impact Force

The cleaning performance of SEPAWJ before and after optimization of SEPAWJ nozzle were tested. Fig. 10 is a comparison of cleaning process before and after optimization.

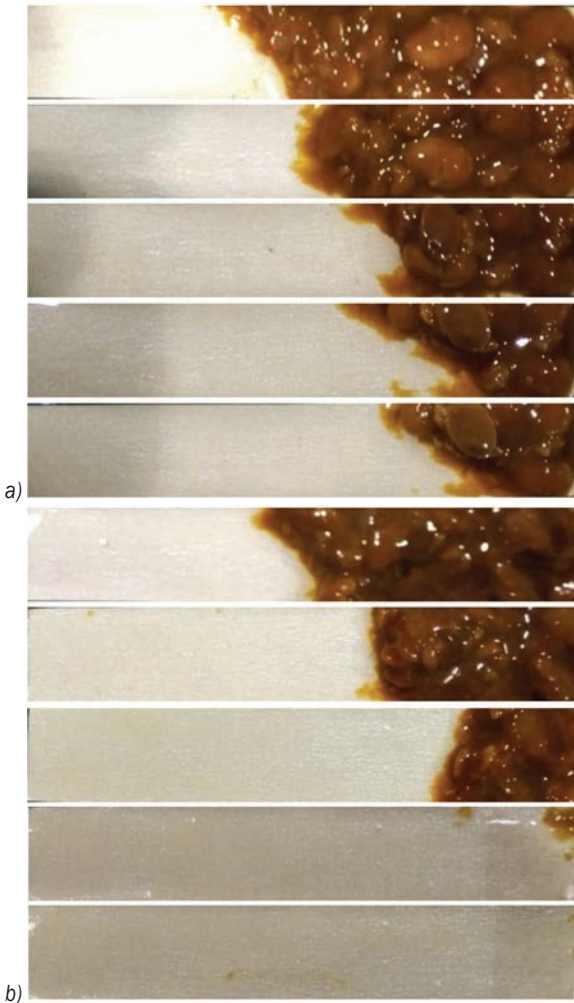


Fig. 10. Comparison of cleaning process before and after optimization; a) original nozzle; b) optimized nozzle

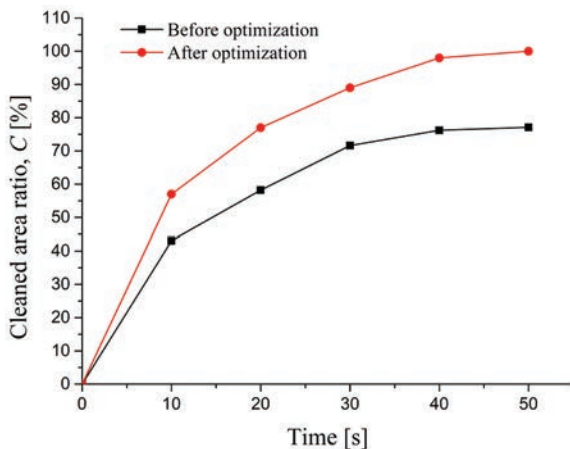


Fig. 11. Comparison of the cleaned area ratio of SEPAWJ before and after optimization

Fig. 11 shows a comparison of the cleaned area ratio of SEPAWJ before and after optimization. From the figure, it can be seen that the cleaning performance of optimized SEPAWJ on soybean paste is better than that of original SEPAWJ. At 40 seconds, the cleaned area ratio of optimized SEPAWJ reaches 96 %, and finally 100 % at 50 seconds. However, the cleaned area ratio of original SEPAWJ reaches only 76 % at 50 seconds, and the difference between them is 22.4 %.

In the first 20 seconds, the cleaned area ratio of the optimized and original SEPAWJ increases rapidly, and that of the original SEPAWJ increases much faster. After 20 seconds, the difference of the growth rate of the cleaned area ratio between the two SEPAWJ decreases gradually and is zero at 50 seconds. During the entire cleaning process, the cleaned area ratio of the optimized SEPAWJ is always higher than that of the original SEPAWJ. At 50 seconds, the cleaned area ratios of the two SEPAWJ do not change much more, and the difference of the cleaned area ratios between the two SEPAWJ reached the maximum of 22.4 %.

4 CONCLUSION

The second-order mathematical RSM were established for the jet characteristics of average impact force F and impact force amplitude ΔF for different chamber and downstream nozzle parameters. The significance of the coefficients of the model and regression equation were tested. Single and coupling factor effects of three parameters (oscillation chamber length, oscillation chamber height and diameter of the downstream nozzle) on performance of nozzle were analysed and parameters of optimum performance were calculated using RSM. The performance of the nozzle before and after optimization was compared experimentally. The result are follows:

1. The RSM model significance levels of average impact force and impact force amplitude are both lower than 0.05, which means that they have high significance. The most significant single factor affecting the average impact force and impact force amplitude of the SEPAWJ is the chamber length. The interactive item of the downstream nozzle inlet diameter and the chamber length has the most significant coupling effect on the SEPAWJ average impact force and impact force amplitude.
2. To maximize both modelled variables, the maximum value of parameters (average impact force and the impact force amplitude) are taken as the optimal nozzle parameters, as follows: the diameter of the upper nozzle inlet is 1.365, the

chamber length is 17.97 mm, and the chamber height is 5.065 mm.

3. The predicted values of RSM under optimized parameters are as follows: impact force is 0.1426 N and impact force amplitude is 0.0167 N. The experimental values under optimized parameters are as follows: the impact force is 0.1484 N and the impact force amplitude is 0.0187 N. The impact force and impact force amplitude errors of prediction and experiment are both less than 5 %, which means the response surface functions are basically accurate.
4. Flow visualization by high speed image acquisition shows the final large water mass of optimized SEPAWJ was formed much earlier, providing for more intensive and intermittent cleaning in comparison with original SEPAWJ.
5. Compared with original SEPAWJ, the average impact force and impact force amplitude of optimized SEPAWJ are increased by 52.00 % and 38.26 %, respectively, and the impact force intensity of fluctuations exhibits peak in the low frequency region around 40 Hz.
6. In the cleaning experiment at 40 seconds, the cleaned area ratio of optimized SEPAWJ reaches 96 %, and finally 100 % at 50 seconds. However, the cleaned area ratio of original SEPAWJ reaches only 76 % at 50 seconds, and the difference between them is 22.4 %, further showing that the optimized SEPAWJ cleaning performance is much higher in comparison with original design.
7. Although the multi-parameter optimization of self-excited pulsed air-water jet nozzle was carried out, only a few key parameters of the nozzle were selected as the optimization variables. In the future, the multi-parameter combination optimization of the self-excited pulsed air-water jet nozzle can be studied by taking into account the tilt angle of the two ends of the mixing chamber, the location and layout of the pores and the aperture of the nozzle as the optimization variables.

5 ACKNOWLEDGEMENTS

The authors would like to thank the support by the National Natural Science Foundation of China (51779106 and 51979126), a project funded by the Priority Academic Programme Development of Jiangsu Higher Education Institutions, Ministry of Education Xihua University (szjj2016-068). The authors would like to thank Slovenian Research

Agency (ARRS) for providing support under research programme Energy engineering P2-0401.

6 NOMENCLATURES

- d_1 Outlet diameter of upstream nozzle, [mm]
 d_2 Inlet diameter of downstream nozzle, [mm]
 d_3 Outlet diameter of downstream nozzle, [mm]
 H_c Oscillation chamber height, [mm]
 L_c Oscillation chamber length, [mm]
 α Inclination angle of oscillation chamber side wall, [°]
 β Inclination angle of oscillation chamber bottom wall, [°]
 F Average impact force, [N]
 ΔF Impact force amplitude, [N]

7 REFERENCES

- [1] Guha, A., Barron, R.M., Balachandar, R. (2011). An experimental and numerical study of water jet cleaning process. *Journal of Materials Processing Technology*, vol. 211, no. 4, p. 610-618, DOI:10.1016/j.jmatprotec.2010.11.017.
- [2] Li, D., Kang, Y., Wang, X., Ding, X., Fang, Z. (2016). Effects of nozzle inner surface roughness on the cavitation erosion characteristics of high speed submerged jets. *Experimental Thermal and Fluid Science*, vol. 74, p. 444-452, DOI:10.1016/j.exptthermfluidsci.2016.01.009.
- [3] Chahine, G.L., Kapahi, A., Choi, J.-K., Hsiao, C.-T. (2016). Modeling of surface cleaning by cavitation bubble dynamics and collapse. *Ultrasonics Sonochemistry*, vol. 29, p. 528-549, DOI:10.1016/j.ultsonch.2015.04.026.
- [4] Labus, T.J., Savanick, G.A. (2001). *An Overview of Waterjet Fundamental and Application*. Waterjet Technology Association, Saint Louis.
- [5] Glenn, L.A. (1975). The mechanics of the impulsive water cannon. *Computers and Fluids*, vol. 3, no. 2-3, p. 197-215, DOI:10.1016/0045-7930(75)90018-3.
- [6] Grinspan, A.S., Gnanamoorthy, R. (2010). Impact force of low velocity liquid droplets measured using piezoelectric PVDF film. *Colloids and Surfaces A: Physicochemical and Engineering Aspects*, vol. 356, no. 1-3, p. 162-168, DOI:10.1016/j.colsurfa.2010.01.005.
- [7] Dehkhoda, S., Hood, M. (2013). An experimental study of surface and sub-surface damage in pulsed water-jet breakage of rocks. *International Journal of Rock Mechanics and Mining Sciences*, vol. 63, p. 138-147, DOI:10.1016/j.ijrmms.2013.08.013.
- [8] Tang, C.L., Hu, D., Zhang, F.H. (2011). Study on the frequency characteristic of self-excited oscillation pulsed water jet. *Advanced Materials Research*, p. 317-319, 1456-1461, DOI:10.4028/www.scientific.net/AMR.317-319.1456.
- [9] Hu, Y.Z. (2016). *Time-Frequency Feature Analysis of the Pulsed Liquid Gas Jet of the Self-Excited Inspiration Nozzle in Deep Water Conditions*. MSc. Thesis, North China University of Water Resources and Hydropower, Zhengzhou.

- [10] Li, D., Kang, Y., Ding, X., Wang, X., Fang, Z. (2017). Effects of nozzle inner surface roughness on the performance of self-resonating cavitating waterjets under different ambient pressures. *Strojniški vestnik - Journal of Mechanical Engineering*, vol. 63, no. 2, p. 92-102, DOI:10.5545/sv-jme.2016.3563.
- [11] Chen, B., Gao, D.R., Liang, Y.N., Zhao, J.H., Sun, Y.N. (2018). Experimental investigation of atomization and droplet turbulence characteristics of a twin-fluid nozzle with different self-excited vibrating cavity structures. *Experimental Thermal and Fluid Science*, vol. 99, p. 525-536, DOI:10.1016/j.exptthermflusci.2018.08.017.
- [12] Hall, J., Ewing, D. (2010). Spectral linear stochastic estimation of the turbulent velocity in a square three-dimensional wall jet. *Journal of Fluids Engineering*, vol. 132, no. 5, p. 1-9, DOI:10.1115/1.4001490.
- [13] Li, D., Kang, Y., Ding, X., Wang, X., Fang, Z. (2016). Effects of area discontinuity at nozzle inlet on the characteristics of high speed self-excited oscillation pulsed waterjets. *Experimental Thermal and Fluid Science*, vol. 79, p. 254-265, DOI:10.1016/j.exptthermflusci.2016.07.013.
- [14] Oh, T.M., Cho, G.C. (2011). Energy loss from an abrasive waterjet for rock cutting. *WJTA-IMCA Conference and Expo*, Houston.
- [15] Thakur, R.K., Singh, K.K. (2020). Abrasive waterjet machining of fiber-reinforced composites: A state-of-the-art review. *Journal of the Brazilian Society of Mechanical Sciences and Engineering*, vol. 42, no. 7, p. 1-25, DOI:10.1007/s40430-020-02463-7.
- [16] Alsoufi, M.S., Suker, D.K., Alhazmi, M.W., Azam S. (2017). Influence of abrasive waterjet machining parameters on the surface texture quality of Carrara marble. *Journal of Surface Engineered Materials and Advanced Technology*, vol. 7, no. 2, p. 25-37, DOI:10.4236/jsemat.2017.72003.
- [17] Wang, W., Zhou, Z. (1988). Rock breaking device with pulse gas-liquid jet. *Mining Technology*, vol.36, p. 23-24, DOI:10.13828/j.cnki.ckjs.1988.36.015. (in Chinese)
- [18] Hu, D., Li, X.-H., Tang, C.L., Kang, Y. (2015). Analytical and experimental investigations of the pulsed air-water jet. *Journal of Fluids And Structures*, vol. 54, p. 88-102, DOI:10.1016/j.jfluidstructs.2014.10.010.
- [19] Box, G.E.P., Wilson, K. (1992). On the experimental attainment of optimum conditions. *Journal of the Royal Statistical Society*, vol. 8, no. 1, p. 1-38, DOI:10.1007/978-1-4612-4380-9_23.
- [20] Vyavahare, G.D., Gurav, R.G., Jadhav, P.P., Patil, R.R., Aware, C.B., Jadhav, J.P. (2018). Response surface methodology optimization for sorption of malachite green dye on sugarcane bagasse biochar and evaluating the residual dye for phyto and cytogenotoxicity. *Chemosphere*, vol. 194, p. 306-315, DOI:10.1016/j.chemosphere.2017.11.180.
- [21] Tang, P., Li, H., Chen, C., Sun, C. Z. (2016). Optimization and experiment of adjustable structural parameters for vertical impact sprinkler with working pressure. *Transactions of the Chinese Society of Agricultural Engineering*, vol. 32, no. 20, p. 99-107, DOI:10.11975/j.issn.1002-6819.2016.20.013. (in Chinese)
- [22] Siddhant, B.P., Jignasa, V.G. (2018). Enhanced solar cell performance by optimization of spray coated CZTs thin film using taguchi and response surface method. *Journal of Materials Science Materials in Electronics*, vol. 29, p. 5613-5623, DOI:10.1007/s10854-018-8530-5.
- [23] Qi, C.X., Liu, H.J., Deng, S.X., Yang, A.H., Li, Z.D. (2018). A modeling study by response surface methodology (RSM) on Th(IV) adsorption optimization using a sulfated β -cyclodextrin inclusion complex. *Research on Chemical Intermediates*, vol. 44, p. 2889-911, DOI:10.1007/s11164-018-3286-3.
- [24] Khoshnamvand, N., Kord, F.M., Mohammadi, A., Faraji, M. (2018). Response surface methodology (RSM) modeling to improve removal of ciprofloxacin from aqueous solutions in photocatalytic process using copper oxide nanoparticles (CuO/UV). *AMB Express*, vol. 8, p. 48, DOI:10.1186/s13568-018-0579-2.
- [25] Öztürk, S., Kahraman, M.F. (2019). Modeling and optimization of machining parameters during grinding of flat glass using response surface methodology and probabilistic uncertainty analysis based on Monte Carlo simulation. *Measurement*, vol. 145, p. 274-291, DOI:10.1016/j.measurement.2019.05.098.
- [26] Gnanavelbabu, A., Saravanan, P. (2020). Experimental investigations of abrasive waterjet machining parameters on titanium alloy Ti-6Al-4V using RSM and evolutionary computational techniques. *Advances in Unconventional Machining and Composites*, p. 413-425, DOI:10.1007/978-981-32-9471-4_33.
- [27] Dani, D.N., Shah H.N. (2016). An experimental investigation of abrasive water jet machining on granite. *International Journal for Innovative Research in Science & Technology*, vol. 3, no. 5, p. 26-31.
- [28] Karakurt, I., Aydin G., Aydiner K. (2012). A study on the prediction of kerf angle in abrasive waterjet machining of rocks. *Proceedings of the Institution of Mechanical Engineers, Part B: Journal of Engineering Manufacture*, vol. 226, no. 9, p. 1489-1499, DOI:10.1177/0954405412454395.
- [29] Gupta, V., Garg, M. P., Batra, N.K., Khanna R. (2013). Analysis of kerf taper angle in abrasive water jet cutting of Makrana white marble. *Asian Journal of Engineering and Applied Technology*, vol. 2, no. 2, p. 35-39.
- [30] Javidan, M., Moghadam, A.J. (2021). Experimental investigation on thermal management of a photovoltaic module using water-jet impingement cooling. *Energy Conversion and Management*, vol. 228, no. 15, art. ID 113686, DOI:10.1016/j.enconman.2020.113686.

Optimization of Running Blade Prosthetics Utilizing Crow Search Algorithm Assisted by Artificial Neural Networks

Manuel Javier Rosel Solis¹ – José Omar Dávalos Ramírez^{2,*} – Javier Molina Salazar² –
Juan Antonio Ruiz Ochoa¹ – Antonio Gómez Roa¹

¹Autonomous University of Baja California, México

²Autonomous University of Ciudad Juárez, México

A crow search algorithm (CSA) was applied to perform the optimization of a running blade prosthetics (RBP) made of composite materials like carbon fibre layers and cores of acrylonitrile butadiene styrene (ABS). Optimization aims to increase the RBP displacement limited by the Tsai-Wu failure criterion. Both displacement and the Tsai-Wu criterion are predicted using artificial neural networks (ANN) trained with a database constructed from finite element method (FEM) simulations. Three different cases are optimized varying the carbon fibre layers orientations: $-45^\circ/45^\circ$, $0^\circ/90^\circ$, and a case with the two-fibre layer orientations intercalated. Five geometric parameters and a number of carbon fibre layers are selected as design parameters. A sensitivity analysis is performed using the Garzon equation. The best balance between displacement and failure criterion was found with fibre layers oriented at $0^\circ/90^\circ$. The optimal candidate with $-45^\circ/45^\circ$ orientation presents higher displacement; however, the Tsai-Wu criterion was less than 0.5 and not suitable for RBP design. The case with intercalated fibres presented a minimal displacement being the stiffer RBP design. The damage concentrates mostly in the zone that contacts the ground. The sensitivity study found that the number of layers and width were the most important design parameters.

Keywords: optimization, crow search algorithm, artificial neural networks, running blade prosthetics, Tsai-Wu criterion, finite element method

Highlights

- An optimization methodology was proposed for the RBP design.
- A new technique for RBP manufacturing was evaluated.
- Carbon fibre layers with layers oriented $0^\circ/90^\circ$ were the best option for the design of the RBP.
- The proposed methodologies reduce the manufacturing costs of the RBP.

0 INTRODUCTION

A prosthesis is an artificial element integrated into the human body to replace an internal or external organ. The most common prostheses are those that replace upper and lower limbs. With the use of new materials and better manufacturing techniques, it has been possible to optimize prosthetic models to replace amputated arms and legs [1] to [3]. Regarding leg prostheses, the applications are diverse; everyday cosmetic prostheses have been created that allow an amputated person to lead a normal life, thereby improving their living conditions. Furthermore, advanced prostheses have been developed that have allowed an athlete with amputations in one or both lower limbs to take part in sports activities almost at the level of a non-amputee athlete. An example is the blade type prostheses used by the South African athlete Oscar Pistorius made with carbon fibre, a composite material with applications in the automotive and aerospace industry, which has properties similar to steel but with little weight, which makes it ideal for prosthetic applications. Manufacturers of these sports implement, for low and high impact activities, such

as Ösur and Ottobock, offer various blade-type sports prostheses, but the high cost of these makes them inaccessible to the general public [4]

An alternative in the manufacture of sports prostheses, like running blade prosthetics (RBP), is the inclusion of additive manufacturing in the process of developing a human prosthesis, in particular, fused deposition modelling, which is one of the most widely used processes due to its simplicity and ease of operation. Therefore, the mechanical properties that composite materials offer can be combined with the advantages of fused deposition modelling, mainly in small-scale production, with the option of manufacturing highly personalized products and, at the same time, with shorter prototypes development times [5].

Türk et al. [6] evaluate the mechanical performance of lower limb prostheses manufactured combining additive manufacturing with carbon fibre-reinforced polymers. They found that by using this technique, the mechanical strength increases by around 40 %, and the weight decreases by 28 %.

Tavangarian et al. [7] studied the mechanical strength of the pylon section of a lower limb prosthetic

manufactured with 3D printing using polylactic acid polymers. They found that this material meets the standards set by ISO 1038:2016 [8] regarding the structural requirements of lower-limb prostheses.

Ouarhim et al. [9] perform the characterization and numerical simulation of laminated glass fibre-polyester composites applied to running blade prosthetics. They used software to simulate the composite materials. Its results show that the number of layers impacts in bending and buckling. Its results show a good agreement between experimental and numerical.

A good balance between displacement and mechanical resistance guarantees the good performance of an RBP. During the change of length or displacement of an RBP, energy is stored and returned, increasing the forward propulsion [10]. However, increasing the displacement can lead to the mechanical failure of RBP, mainly in the sections with a curved shape.

To achieve an optimal design of an RBP, advanced tools as optimization algorithms are required. These types of algorithms are widely used to solve diverse problems in engineering fields [11] to [14]. A common characteristic of optimization algorithms is the large number of objective function evaluations required to find an optimal solution. When experimental or finite element method (FEM) calculations are employed to perform objective function evaluations, the computational cost increases, making the optimization process infeasible. In these cases, surrogated methods are an option to reduce the optimization time [15] to [17]. An example of an optimization strategy assisted by surrogated methods applied to lower limb prosthesis manufactured with composite materials can be found in [18], focusing on the optimization of the pylon tube made of isogrid structures. Due to optimization, they achieved a reduction of 13.3 % and 70.59 % in the mass and the Tsai-Wu index under compression effects.

Unlike previous optimization work, the present investigation is applied to a lower-limb sport prosthetics which can be used to reintegrate people with lower-limb amputations into sport activities. Also, optimization methodology employs artificial neural networks (ANN) with two intentions: to evaluate the objective function and to use the ANN coefficients in the calculation of relative importance of design parameters.

This work employs an optimization strategy to improve the design of an RBP. This strategy integrates crow search algorithm (CSA), and ANN and FEM calculations. The objective of the optimization was

to find a design that has better resistance to failure without decreasing its capability to displace in order to maintain its functionality. The failure criterion used for determining the resistance of the RBP was the Tsai-Wu criterion. To reduce the computational cost, displacements and the Tsai-Wu failure criterion were calculated by means of ANN. The ANN was trained with a database constructed from FEM calculations of displacement and Tsai-Wu failure. The manufacturing process, modelled using commercial FEM software, is a lay-up process with carbon fibre layers stacked around acrylonitrile butadiene styrene (ABS) cores. Three carbon fibre orientations were tested to find the better design option: $-45^\circ/45^\circ$, $0^\circ/90^\circ$, and a combined case with $-45^\circ/45^\circ$ and $0^\circ/90^\circ$ orientations. Using the ANN coefficients, a sensitivity analysis was performed to know the relative importance of the design parameters in each orientation.

1 METHODS

1.1 RBP Design and Manufacturing

An RBP is a hook-shaped artefact made primarily of composite materials from epoxy matrix carbon fibres. The manufacturing processes used for its manufacture are the lay-up process and the pre-impregnated fibre process. The first consists of applying or mixing epoxy resin with a brush or roller into the carbon fibre layers that are stacked until reaching the thickness based on the desired resistance. Another manufacturing process consists of the use of pre-impregnated carbon fibre layers that, after being stacked, must undergo a thermal treatment in an autoclave for the activation of the resin [19]. The RBPs have a spring-like mechanical behaviour; during the first gait cycle, the prosthesis is compressed by the effect of the dynamic load of the body storing energy. In the second stage of the gait cycle, that stored energy is released, generating a thrust forward, just as the heel joint of the human foot does. The maximum efficiency in this energy return of a high-performance RBP ranges between 63 % and 95 % of the accumulated energy [20].

1.2 Optimization Methodology

A bio-inspired method used in optimization is the CSA. This novel algorithm, developed by Askarzadeh [21], is based in the behaviour of crows, considered the most intelligent birds. A characteristic of the crow's behaviour is the way they store food in hideouts to prevent that other crows from stealing it; at the same time, they look for opportunities to steal

the food of other members of the flock. Crows use the gained experience stealing food to deceive potential plunderers, employing diverse strategies [22]. Crows, always try to find optimal food places. This intelligent behaviour is replied in the CSA in which the optimal place is analogous to the global optima into the search space. In CSA, it is assumed that the crows live in flocks, can memorize the places where they hide their food, a crow follows another to try to steal its food and protect its hideouts from other crows via a probability reason [22].

In the CSA optimization process, during a iteration *iter*, a crow *i*, from a flock of size *N*, occupy a position defined by the vector $x^{i,it} = [x_1^{i,it}, x_2^{i,it}, \dots, x_d^{i,it}]$, where $i=1,2,\dots,N$, $it=1,2,\dots,it_{max}$, it_{max} is the maximum number of iterations, and *d* is the dimension of the problem or the number of variables in the design. The position, $m^{i,it}$, of the hideout *it* is stored in the crow memory and represents the best position at *it*, the far. For the next iterations, the crow will try to find better positions.

Two situations may occur when, at iteration *it*, a crow *j* visits the hideout where it stores its food and a crow *i* is on the lookout attempting to steal it: (1) the crow *j* does not realize that crow *i* followed it and reveals its hideout to the thief crow; (2) the crow *j* detects the presence of the crow *i* and changes its trajectory to avoid revealing the location of its hideout. In the first situation, the new position of crow *i* is defined by:

$$x^{i,it+1} = x^{i,it} + r_i \times fl^{i,it} \times (m^{i,it} - x^{i,it}), \quad (1)$$

where $0 \leq r_i \leq 1$ is a random number with uniform distribution and $fl^{i,it}$ is the flight length of crow *i* at iteration *it*. If the second situation arises, the crow *j* will change its trajectory through fake hideouts to deceive to crow *i*. Both situations are expressed as follows:

$$x^{i,it} = \begin{cases} x^{i,it} + r_i \times fl^{i,it} \times (m^{i,it} - x^{i,it}) & r_j \geq AP^{j,it} \\ \text{a random position} & \text{otherwise} \end{cases}, \quad (2)$$

where $0 \leq r_j \leq 1$ is a random number with uniform distribution and $AP^{j,it}$ is the awareness probability of the crow *j* at iteration *it*. Intensification and diversification are two important characteristics of metaheuristic algorithms; these characteristics in CSA are provided by *fl* and *AP*. Lower values of both parameters will guide the optimization to local search, increasing the intensification, whereas larger values expand the search randomly in the decision space

but reduce the probability of found optimal solutions, resulting in increasing diversification.

In Fig. 1, the flowchart of the CSA is presented. In the first step, the objective function, the range of decision variables and constraints are defined, also, the CSA parameters, *N*, it_{max} , *d*, *fl*, and *AP* are initialized. In Step 2 the positions of flock crows are defined randomly; because the crows do not have prior experience at Iteration 1, it is assumed that the initial position is the location of the hideout. In Step 3, the algorithm evaluates the objective function. In the next step, all the crows of the flock update its position using the next procedure: a crow *i* randomly selects a crow *j* of the flock and tries to discover the position of the hideout, m^j . The position is updated using Eq. (2). In Step 5, if the new position of crow *i* is feasible, then its position is updated; if not, crow *i* will remain at the initial position. In the next step, the objective function is evaluated for the new crow flock positions. In Step 7, the memory of the crow flocks is updated. A comparison is made between the value of the objective function evaluated with both the new position $x^{i,it+1}$ and the position $m^{i,it}$. If the new position performs better. the memory *it* is updated; if not, the memory remains without changes. This is mathematically stated as follow:

$$m^{i,it+1} = \begin{cases} x^{i,it+1} & F_{obj}(x^{i,it+1}) \text{ better than } F_{obj}(m^{i,it+1}) \\ m^{i,it+1} & \text{otherwise} \end{cases}. \quad (3)$$

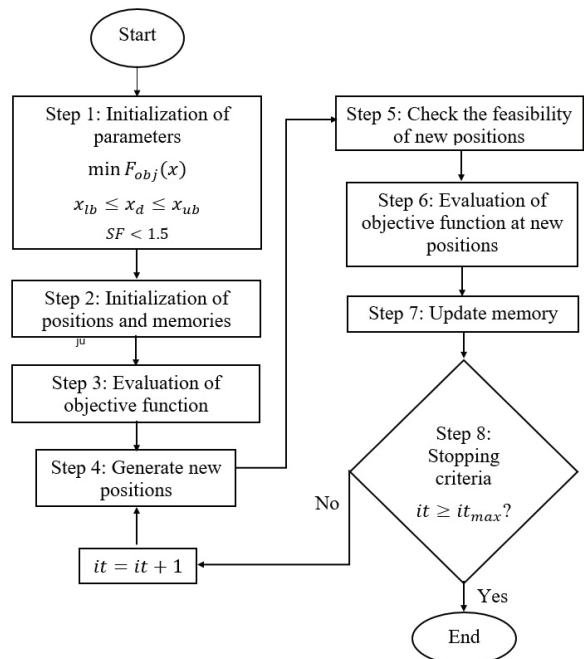


Fig. 1. CSA flowchart

1.3 Artificial Neural Network

An ANN is a machine-learning technique used in the prediction of output variables as a function of input variables. A typical ANN consists of processing elements or neurons grouped in layers sequentially connected by synaptic weights. The most popular type of ANN is the multi-layer perceptron (MLP) with at least three neurons layers divided into input, hidden, and output layers. The number of neurons clustered at input and output layers is equal to the number of input and output variables, respectively, whereas, in the case of the hidden layer, the number of neurons is defined in terms of the predictive accuracy level of the ANN model [23] to [25]. The output of layers is computed by means of transfer functions whose argument is the summation of the multiplication of the corresponding weight by input signals plus a bias [26] a comprehensive review of the artificial neural network (ANN). The ANN prediction is computed by the next expression:

$$ANN_{output} = TF^O \left[\sum_{j=1}^n (w_j^2 TF_j^H) + b^2 \right]. \quad (4)$$

Here ANN_{output} is the ANN prediction, TF^O is the transfer function of the output layer, w is the connection weight, TF^H is the transfer function of the hidden layer, b is the bias, n is the number of neurons in the hidden layer, and the superscript 2 indicates the output layer.

The ANN is trained using a set of sample data. During the training, the ANN coefficients, w and b , are proposed and the error between ANN_{output} and real outputs, stored in a database, is calculated. This error is minimized by adjusting the coefficients by means of a training algorithm.

1.4 Tsai-Wu Failure Theory

The Tsai-Wu failure [27] theory is widely used in the prediction of failure in laminates. In the case of laminate analysis, the governing equation in matrix form is:

$$\begin{Bmatrix} N \\ M \end{Bmatrix} = \begin{bmatrix} A & B \\ B & D \end{bmatrix} \begin{Bmatrix} \varepsilon^0 \\ k \end{Bmatrix}. \quad (5)$$

Here, N and M are the resultant force and moment

respectively, $\varepsilon^0 = \begin{bmatrix} \varepsilon_x^0 \\ \varepsilon_y^0 \\ \gamma_{xy}^0 \end{bmatrix}$ and $k = \begin{bmatrix} k_x \\ k_y \\ k_{xy} \end{bmatrix}$ are the displacement in the midplane and curvature effects

respectively, A , B and D are the extensional, coupling and bending matrices, which are calculated as follow:

$$A = \sum_{k=1}^n (\bar{Q}_k) (t_k - t_{k-1}), \quad (6)$$

$$B = \sum_{k=1}^n (\bar{Q}_k) (t_k^2 - t_{k-1}^2), \quad (7)$$

$$D = \sum_{k=1}^n (\bar{Q}_k) (t_k^3 - t_{k-1}^3). \quad (8)$$

Here, n is the total number of layers, \bar{Q} is the transformed stiffness matrix, and t is the thickness of the composite layer. Using the stress-strain relationship for laminates, it is possible to calculate the state of stress of each composite layer, as is stated in Eq. (9):

$$\begin{bmatrix} \sigma_x \\ \sigma_y \\ \tau_{xy} \end{bmatrix} = \begin{bmatrix} \bar{Q}_{11} & \bar{Q}_{12} & \bar{Q}_{16} \\ \bar{Q}_{12} & \bar{Q}_{22} & \bar{Q}_{26} \\ \bar{Q}_{16} & \bar{Q}_{26} & \bar{Q}_{66} \end{bmatrix} \begin{bmatrix} \varepsilon_x^0 \\ \varepsilon_y^0 \\ \gamma_{xy}^0 \end{bmatrix}, \quad (9)$$

where σ_x and σ_y are the normal stresses in x and y directions respectively, τ_{xy} is the shear stresses and γ_{xy}^0 is the shear strain. The calculation of the stress state allows using the Tsai-Wu failure criterion:

$$H_1 \sigma_1 + H_2 \sigma_2 + H_6 \tau_{12} + H_{11} \sigma_1^2 + H_{22} \sigma_2^2 + H_{66} \tau_{12}^2 < 1. \quad (10)$$

The Tsai-Wu criterion states that the failure occurs when this condition is not satisfied. In the FEM software used, this condition is associated with the F in composite materials so that in FEM simulations, if $F < 1$ the failure is expected.

2 PROBLEM FORMULATION

This work focuses on obtaining the optimal design variables that allow the maximum displacements of an RBP constrained by the safety factor (F) based on the Tsai-Wu failure theory. The process used in the manufacturing of the RBP is the lay-up process, in which layers of 3k woven carbon fibre and epoxy resin are used. The fibre layers are placed in $-45^\circ/45^\circ$ and $0^\circ/90^\circ$ orientations.

The strategy employed consists of obtaining the design parameters through an optimization algorithm that evaluates the objective function that defines the optimization problem; nevertheless, during the optimization, it is not feasible to evaluate it by means of numerical methods due to excessive consumption of time and computational resources. To improve the optimization process, a mathematical model is

constructed using a surrogated method. This model will predict both the displacement and SF, which are required in objective function evaluations. To obtain this model, it is necessary to construct a database that contains a set of combinations of design parameters with their respective responses, in this case, displacement and \mathcal{F} . The responses to be obtained from FEM calculations due to the number of required simulations is significantly lower than in the optimization process. Employing this strategy led to a reduction of the required time to design an RBP. For this research, the chosen optimization method was the CSA, whereas ANN was used as surrogated method.

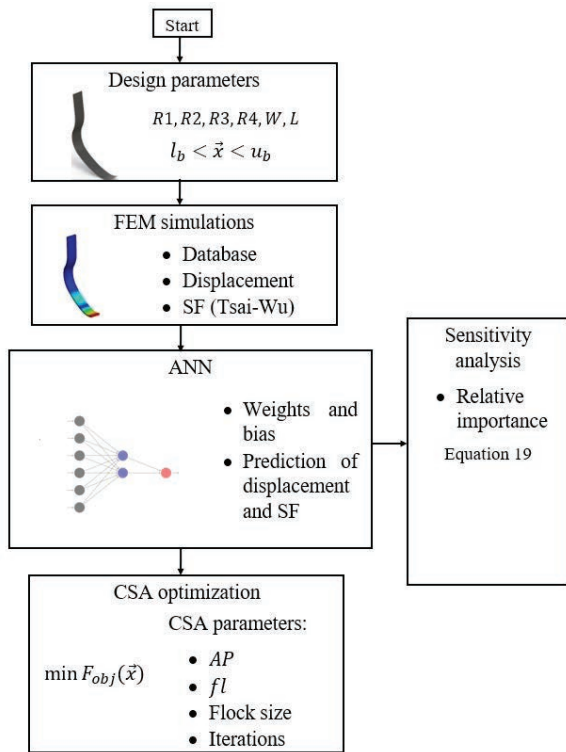


Fig. 2. Optimization procedure

The sequence of activities to optimize the RBP is described in Fig. 2. First are defined the design variables with its bounds and the prosthesis load conditions. Afterward, the FEM calculations are performed to generate the database whose combinations are based on a design of experiments in order to promote the learning of the ANN. In the next step, the database was used to train and test the ANN models that will predict the prosthesis displacements and the \mathcal{F} , respectively. In this step, the ANN coefficients, weights, and biases are obtained. Before the optimization, the relative importance of each of the design variables in the variables predicted is

calculated by means of a sensitivity analysis. Finally, in the optimization process, the CSA parameters are defined, and the objective function is evaluated, obtained as a result the optimization of the RBP. This process is performed three times for each of the fibre layer orientations. A detailed description of this strategy is presented in the next sections.

2.1 CSA Parameters

Three optimizations were performed for different layer orientations: a first case, C1, with layers of carbon fibre with orientation $-45^\circ/45^\circ$, a case C2 with layers of carbon fibre with orientation $0^\circ/90^\circ$ and a third case, C3, with a combination of carbon fibre layers oriented $-45^\circ/45^\circ$ and $0/90^\circ$. The objective function that defines the problem is expressed by:

$$\min F_{obj} = 15 - d_{ANN}, \quad (11)$$

where F_{obj} is the objective function, d_{ANN} is the displacement calculated by means of ANN and 15 is a maximum displacement, expressed in mm, expected during the optimization. This value was set based on the results obtained from the central composite design of experiments. The objective function must be minimized because it is expected that as the obtained displacement increases during CSA iterations, the value of the function approaches zero. The objective function is subjected to:

$$1.2 - SF_{ANN} \leq 0, \quad (12)$$

$$x_i^{lb} \leq x_i \leq x_i^{ub}, \quad (13)$$

here \mathcal{F}_{ANN} is the safety factor predicted using ANN, x_i is the i^{th} design variable, and the superscripts lb and ub are the lower and upper bound, respectively.

The same optimization parameters were used for the three optimization cases. Each optimization was carried on during 1000 iterations; the flock size was 50 crows, fl was 2, and AP was 0.1.

2.2 Parameterization

In Fig. 3, the geometric segments of the RBP profile are illustrated. For the optimization, the dimensions of two of them stay constant. These two segments belong to the joint with the human body (top of the RBP), with a length of 97.12 mm, and the contact area with the ground (bottom of the RBP), with an arc length of 10 mm. The remaining four segments, associated with the letter R, are defined geometrically by radii whose dimensions were selected as design parameters for the optimization. To guarantee a smooth transition, the

points of segments $R1$, $R2$, $R3$ and $R4$ are tangential to each other. The last geometric parameter corresponds to the width, W , of the RBP. An additional parameter is the number of layers of carbon fibre that cover the ABS core. This parameter must be an even number to maintain the same number of layers on both the front and the back of the RBP. The bounds of the design parameters were the same for the three optimization cases and are listed in Table 1. The geometry used was a surface modelled in CAD software, based on the dimensions of a commercial prosthesis [28]. The geometry profile was obtained from the centreline of the original one, as it was required to generate the surface necessary for the simulation of a FEM module for composite materials.

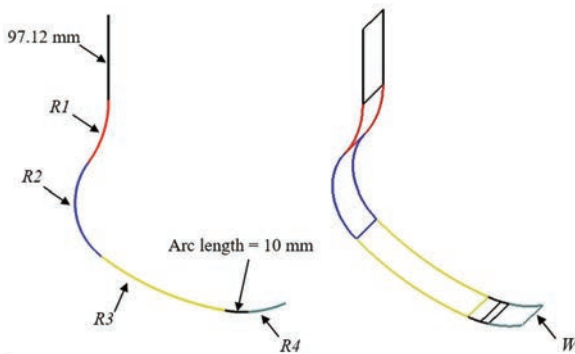


Fig. 3. Geometrical parameters of the RBP

Table 1. Design parameter bounds

Design parameter	Lower bound (lb)	Upper bound (ub)
$R1$ [mm]	106.2	129.8
$R2$ [mm]	74.7	91.3
$R3$ [mm]	283.5	343.5
$R4$ [mm]	110.7	135.3
W [mm]	40.5	49.5
No. of layers [-]	18	26

2.3 Generation of Database and FEM Simulations

For each optimization case, a database based on a central composite design of experiments was generated to be used in the ANN predictions. The size of each database was 6×125 , where 6 is the number of input variables or design variables and 125 is the number of design combinations in the database. The dimensions of each combination varied according to the design of experiments, except for those remaining constant, as was referred in Fig. 3. For each combination, the displacement and the SF using

static linear FEM calculations were calculated. To characterize the materials in the simulations, a special module for composite materials was used. Here, were set the inputs shown in Table 2; the number of layers, in even number, to maintain the symmetry of the prosthesis, the materials that make up the ABS composite material, fibre, core, and combinations of fibre orientations. Properties of carbon fibre and ABS are presented in Tables 3 and 4, respectively.

Table 2. Input parameters for composite materials

Fabrics	ABS, Core
Number of layers	18, 20, 22, 24, 26
Sub laminates	$-45^\circ/45^\circ$, $0^\circ/90^\circ$

Table 3. Properties of 3k woven carbon fibres

Properties	Unit	Value
E_x	[MPa]	59160
E_y	[MPa]	59160
E_z	[MPa]	7500
ν_{xy}	[-]	0.04
ν_{yz}	[-]	0.3
ν_{xz}	[-]	0.3
ρ	[kg/m ³]	1451

Table 4. Properties of ABS

Property	Unit	Value
E	[MPa]	2588
ν	[-]	0.36
ρ	[kg/m ³]	1040

This configuration was exported to a static structural analysis, where each layer was discretized using shell elements, which have 4 nodes per element and 6 degrees of freedom per node. The finite elements have a size of 2 mm resulting in a mesh size of 6400 elements per layer (Fig. 4a). The number of elements was selected based on the comparison between FEM and experimental measurements.

The load was applied in the top segment of the RBP, whereas the displacement was constrained in all directions in the segment of contact with the ground (Fig. 4b). The magnitude of the load was set considering a human weight of 77.6 kg, which results in a static load of 761.25 N. For dynamic conditions, the load was increased 2.7 times, which corresponds to a maximum load peak during running [29]. Then, the applied load was 2055 N.

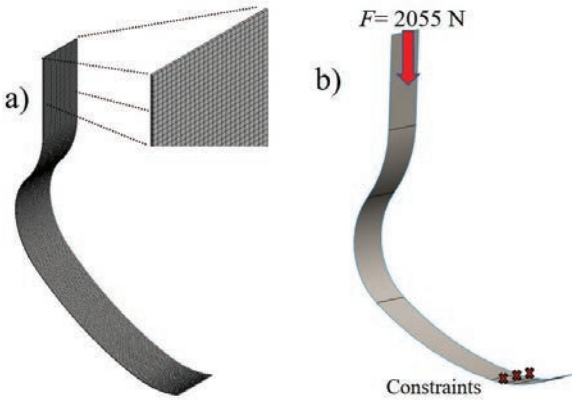


Fig. 4. a) Discretized model, and b) force and constraints

From the FEM simulations, the displacement of RBP and the SF based on Tsai-Wu failure theory were obtained.

2.4 ANN Modelling

To reduce the computational time during the design optimization, a total of six ANN models were trained to predict the displacement and SF factor for each of the optimization cases. The ANN was trained using the Levenberg-Marquardt algorithm [30] and [31] with a learning rate of 1×10^{-4} . The transfer function for the hidden layer, TF^H , was the hyperbolic transfer function Eq. (14), whose argument is defined by Eq. (15), whereas output layer TF^O was linear [32] and [33].

$$TF_j^H = \frac{2}{1 + e^{-2x_j}} - 1, \quad (14)$$

$$x_j = \sum_{i=1}^m (w_i^1 in_i) + b_n^1, \quad (15)$$

Here x_j is the argument for the transfer function of the j^{th} hidden neuron, m is the number of neurons in the input layer or number of inputs and the superscript 1 indicates the hidden layer.

The architecture of the net consists of an input layer with six neurons and one neuron at the output layer. In the hidden layer, all the nets that were used to predict the displacement and Tsai-Wu criterion in the optimization cases contain two neurons.

Eighty per cent of data samples were used for training, and the rest for testing. Input data were normalized between 0.1 and 0.9 by means of [34]:

$$in_i = 0.8 \left(\frac{In_i - In_{low}}{In_{upp} - In_{low}} \right) + 0.1, \quad (16)$$

where in_i is the normalized input, In_i is the unnormalized input, In_{low} is the input lower bound and In_{upp} is the input upper bound.

During training and testing, the ANN was evaluated using the mean squared error, and the correlation coefficient defined by Eqs. (17) and (18), respectively:

$$RMSE = \frac{\sum_{i=1}^T (y_{ANN} - y_{FEM})^2}{T}, \quad (17)$$

$$R^2 = 1 - \frac{\sum_{i=1}^T (y_{ANN} - y_{FEM})^2}{\sum_{i=1}^T (y_{FEM} - y_{ave})^2}, \quad (18)$$

where y_{ANN} is the output predicted by ANN, y_{FEM} is the output predicted by FEM, y_{ave} is the average of actual values and T is the number of samples.

2.5 Sensitivity Analysis

A sensitivity analysis enables determining the relative importance of each of the design variables in the displacement and in the Tsai-Wu criterion. For this purpose, the equation proposed by Garson [35] was used. Eq. (19) is suitable due its use of the ANN synaptic weights to calculate the percentage of importance of each variable. In addition to relative importance, the obtained results of the sensitivity analysis can provide information about of the relation between the design variables.

$$I_m = \frac{\sum_{j=1}^n \left(\frac{|w_{jm}^1|}{\sum_{i=1}^m |w_{in}^1|} \times w_{jm}^2 \right)}{\sum_{i=1}^m \left(\sum_{j=1}^n \frac{|w_{in}^1|}{\sum_{i=1}^m |w_{in}^1|} \times w_{jm}^2 \right)}, \quad (19)$$

3 RESULTS

3.1 Numerical Validation

A comparison was made between FEM simulations and experimental test results reported by Rosel-Solis et al. [36]. The specimen was manufactured by the lay-up process with carbon fibres with $0^\circ/90^\circ$ orientation. The machine was a Shimadzu AG-IC stress floor machine with a load cell of 100 kN. The material conditions were the same as described above, whereas the force and support conditions were set as in the experiment. The comparison is shown in Fig.

5. The maximum difference between experimental and numerical displacements was around 8 % caused by a force near 600 N. From there, the difference decreases considerably. Based on these results, it can be stated that the proposed methodology to calculate displacements and SF is highly suitable for this purpose.

3.2 ANN Results

Six models were trained to vary the number of hidden neurons to obtain the best ANN performance. The architecture obtained was 6:2:1 for all ANN models. This means that two neurons are in the hidden layer. The comparison of FEM and ANN results for displacement and SF are presented in Fig. 6. A good approach is observed in the prediction of both variables. The values of R^2 were >0.99 for all models, whereas the values obtained of MSE were $<1.3 \times 10^{-2}$.

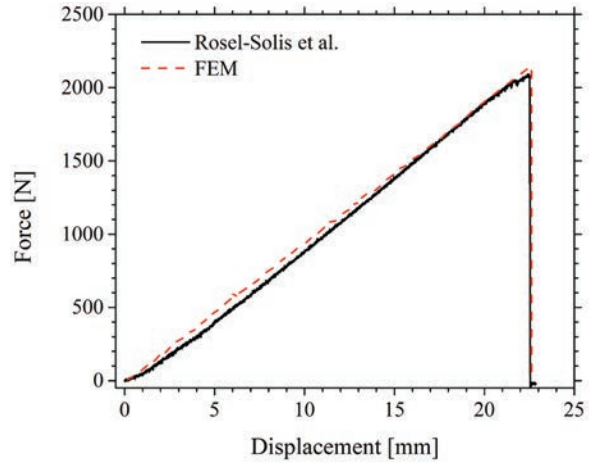


Fig. 5. Comparison between experimental and numerical results

Five new FEM simulations, with different design parameters than the stored in database, were performed

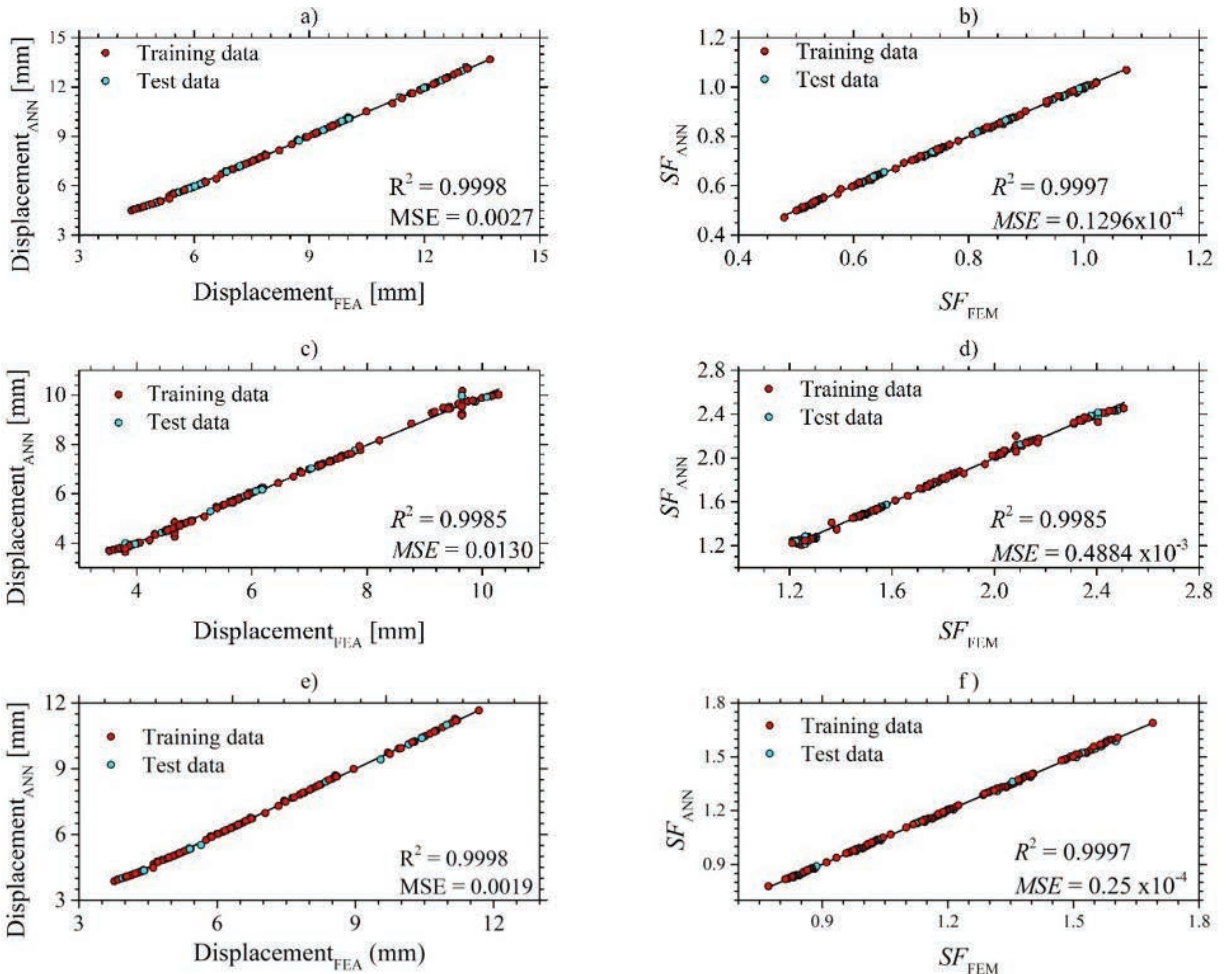


Fig. 6. Comparison of ANN and FEM predictions; a) C1 displacement, b) C1 SF, c) C2 displacement, d) C2 SF, e) C3 displacement, f) C3 SF

to test each ANN models. The results are presented in Fig. 7. The prediction of displacement and SF in C1 had an average error of 5 % and 2 %, respectively. For C2, the average error for displacement was 3.5 and for SF was 3.2 %, whereas in C3 the ANN model predicted the displacement and SF with an average error of 4.1 % and 4.2 %, respectively. These findings guarantee the capability of ANN accurate predictions with the proposed architecture.

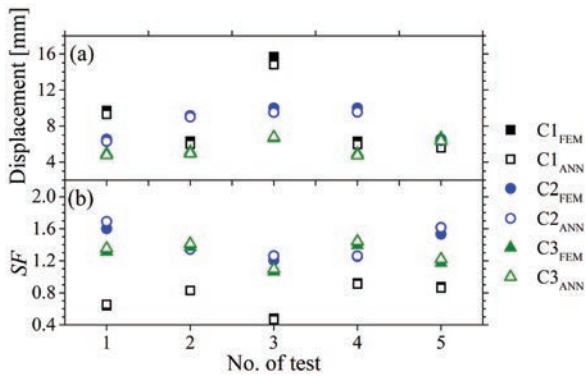


Fig. 7. Testing of ANN models

3.3 Optimization Results

The optimization convergence for three cases is presented in Fig. 8. Around the first 300 iterations, the CSA has identified the region of the search space where the optimal solutions are located. Minimal changes are observed in the objective function value from the subsequent iterations.

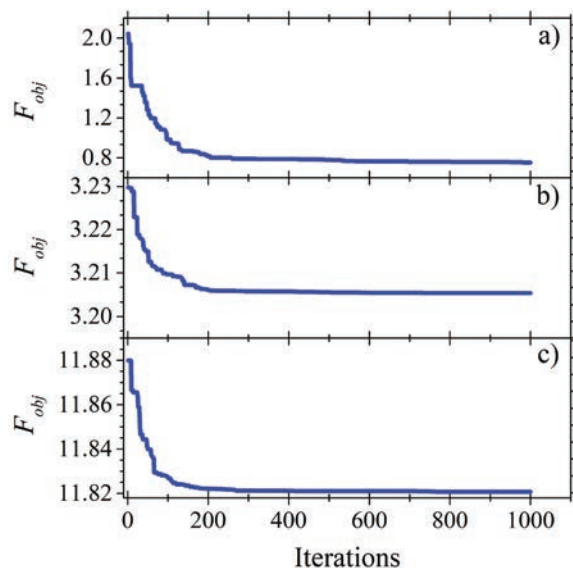


Fig. 8. CSA optimization convergence for: a) C1, b) C2, and c) C3

The optimized results of displacement and SF are presented in Table 5. In C1, with fibres oriented $-45^{\circ}/45^{\circ}$, no solutions that meet the requirements of an $\mathcal{F} > 1.2$ were found; however, the displacement was higher than in the rest of the cases. This result shows that the fibre orientation is not suitable to resist the working conditions of the RBP. The C3 presents the higher \mathcal{F} , but at the same time, the displacement was shorter with only 5 mm. The best balance between displacement and \mathcal{F} was found in C2. In this case, the displacement was 9.19, and the SF was 1.34. Carbon fibres with $0^{\circ}/90^{\circ}$ orientation results in the best option for the design of RBP. The addition of layers with $0^{\circ}/90^{\circ}$ in a combined case, C3, reduces the capability of displacement of only layers oriented $-45^{\circ}/45^{\circ}$. The fibres oriented at $-45^{\circ}/45^{\circ}$ have a more elastic behaviour because they are not perpendicular to the direction of the applied load; therefore, there is energy dissipation.

Table 5. Displacement and SF obtained from optimization

	Displacement [mm]	\mathcal{F}
C1	16.24	0.43
C2	9.19	1.34
C3	5	1.45

In Fig. 9, the displacement and SF obtained from the optimization were compared with those obtained in the database. The search space is reduced to the zone where one of the two requirements, either displacement or \mathcal{F} , stands a greater chance of improvement. In C1, the increase of displacement is remarkable due to the low capability of RBP design to increase its strength to the applied load. C2 presents the same trend to improve its displacement; however, its \mathcal{F} is over the defined limit, which favours the RBP design. In the case of C3, the trend is reversed and now the optimization leads toward and improvement of the \mathcal{F} , decreasing considerably its displacement. These results confirm C2 as the best option for the design of the RBP.

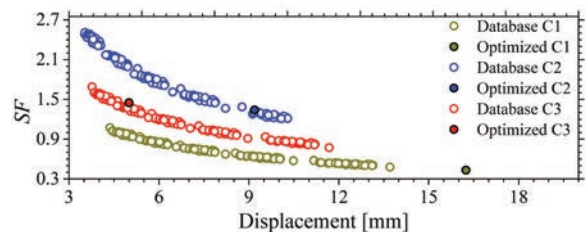


Fig. 9. Comparison between database and optimized cases; C1, C2, and C3

The design variables for each case are presented in Table 6. It is observed that R2 presents the same value for the three cases and corresponds to its lower bound. It should be noted that W in C1 is on the low bound, and this had a negative impact in its resistance. Cases with a short number of layers were those who presented higher displacements, whereas in C3 with 24 layers, the displacement was reduced. Then, it is observed that a lower number of layers helps to decrease the stiffness. The R2 segment, being in the middle part of the RBP in relation to its height and a greater horizontal distance from the direction of application of the load, is subjected to a greater bending moment than the rest of the segments of the RBP. For this reason, the smaller the dimension of R2, the better the behaviour of the prosthesis. The values of segments R1, R3, and R4 vary depending on maintaining an optimal horizontal extension between R2 and R4 to minimize the effect of total flexion of the RBP. Also, the fact that manufacturing costs are reduced with fewer layers must be considered.

Table 6. Optimized design parameters

Design parameter	C1	C2	C3
R1 [mm]	106.207	129.7	108.85
R2 [mm]	74.7	74.7	74.7
R3 [mm]	346.49	305.61	333.68
R4 [mm]	133.75	129.14	110.7
W [mm]	40.5	49.48	49.5
No. of layers	18	18	24

A comparison of the RBP profiles is presented in Fig. 10. At the segment R1, the profile of both C1 and C3 is similar and changes from R2, whereas the C2 profile presents lower outward curvature. All the profiles match in the junction of the end of R3, and the start of the ground contact area due to the length of this area is constant. Beyond the contact area, the profiles separate again, and the C3 curves inward to RBP more than C2 and C3.

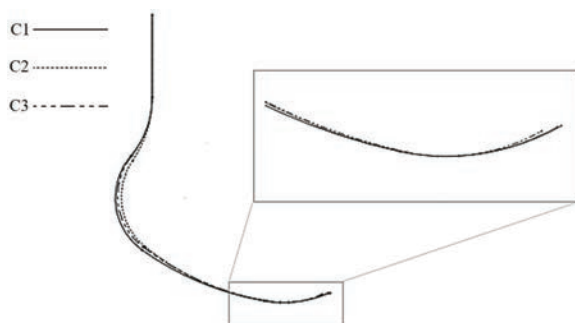


Fig. 10. Comparison of optimized RBP profiles

The displacement contours of the optimized RBP are presented in Fig. 11. The RBP displacement is higher at the top and diminishes until the area of contact with the ground. Beyond this point until the bottom tip, the displacements are negligible. The difference of displacements between top and point of contact of the RBP optimized models indicates that the stiffness of C1 design is lower than C2 and C3, whereas C3 presents higher stiffness. Higher displacement is a characteristic that favours the return of energy that the RBP must offer when operating. The C1 design presents the highest displacement value due to the behaviour of the fibres oriented at $-45^\circ/45^\circ$ that tend to dissipate energy. This level of displacement would be desirable if it is complemented by an acceptable SF. The C2 design with fibre orientations at $0^\circ/90^\circ$ offers a higher level of stiffness, which produces a lower displacement value than the C1 design; this is because part of the fibres of this configuration oppose resistance in a direction parallel to the applied force. The combination of $-45^\circ/45^\circ$ and $0^\circ/90^\circ$ orientations further increases stiffness, affecting displacement, obtaining the lowest displacement values of the three designs.

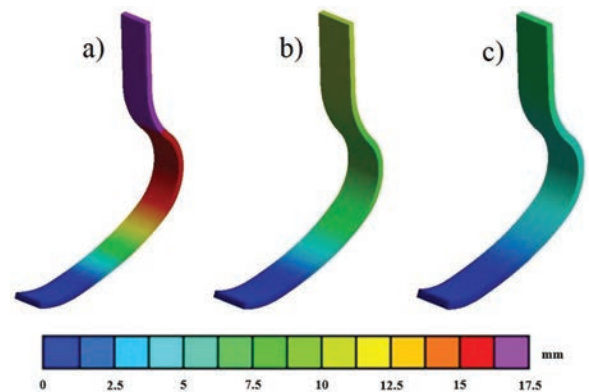


Fig. 11. Displacement contours of optimized cases; a) C1, b) C2, and c) C3

Fig. 12 shows the zones where the SF occurs in the RBP optimized designs and its magnitudes. The critical zone is the contact area in which the SF is lower. This occurs due to the fact that in this segment the displacements are restricted, and reaction forces increase. Zones with high curvature also present lower SF, which can be attributed to a stress concentration in these locations. In C1, due to the orientation of layers, low SF magnitude covers a large section of the RBP. Areas below the minimum ($\mathcal{F} < 1$) appear in the C1 design; therefore, under the analysis conditions, it is not satisfactory since

the RBP fails. The fibre orientation $-45^{\circ}/45^{\circ}$ favours the flexural capacity of the RBP but acts negatively on its resistance. Designs C2 and C3 obtained satisfactory SF values, with C3 obtaining the best. However, considering the displacement results, the C2 design is the one that offers a better balance between displacement and F , in addition to requiring a lower number of layers than C3. The combination of fibre orientation in the C3 design increased its stiffness and decreased its flexibility, obtaining a higher F but reducing displacement.

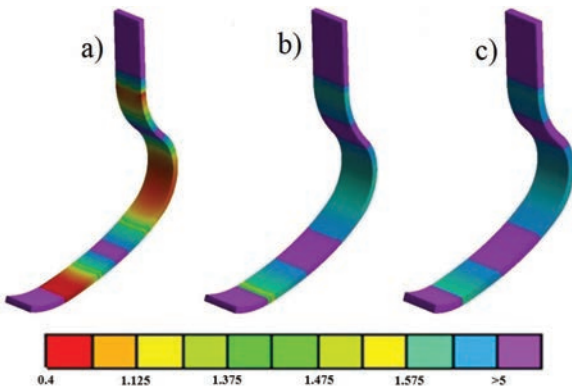


Fig. 12. SF contours of optimized cases; a) C1, b) C2, and c) C3

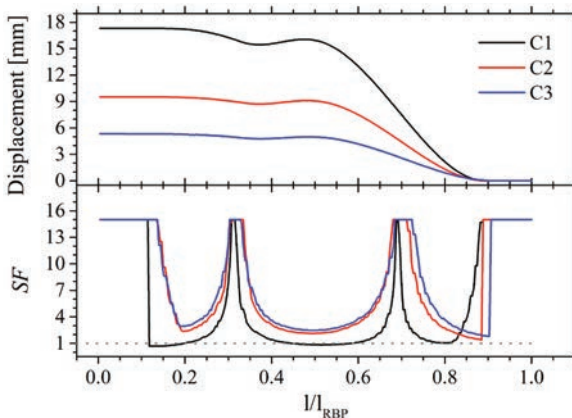


Fig. 13. Displacement and SF along RBP

Displacement and F were obtained along a path at the centre of the RBP in Fig. 13. The length of the RBP was normalized from top to bottom. The maximum displacement is observed at the top of the RBP and remains constant. Near the middle displacement diminishes and drops to zero at the point of contact. Due to the amplitude of displacements, large forward propulsion will be expected in C1 but, due to fluctuations observed, the return of energy will be smoother in C2 and C3. In the case of F , three critical zones were identified. In the design, C1 failure

occurs in almost 25 % of the RBP length whereas in C2 and C3 the percentage of length with lower F values is smaller. Another difference was the region where minimum F appears in C1 is at 10 % away from the RBP top; cases C2 and C3, this region was near the point of contact.

3.4 Sensitivity Analysis Results

The results of the sensitivity analysis are presented in Fig. 14. The displacement is mostly influenced by the number of layers in all cases and to a lesser extent by R1 for the cases C1 and C3, whereas in the C2 case, the lowest percentage of relative importance was the R4. In the F , the number of layers is the most important variable for C1 and C3; however, in C2, it is the width of the prosthesis. These differences can be attributed to the orientation of the fibres. The fibres at $-45^{\circ}/45^{\circ}$ make the RBP more flexible but decreases its resistance; therefore, to improve this negative condition, the carbon fibre layers must be increased. In the case of the $0^{\circ}/90^{\circ}$ fibre orientation design, by increasing the width of the RBP, the number of fibres acting to support the applied load is increased, which improves their resistance and displacement.

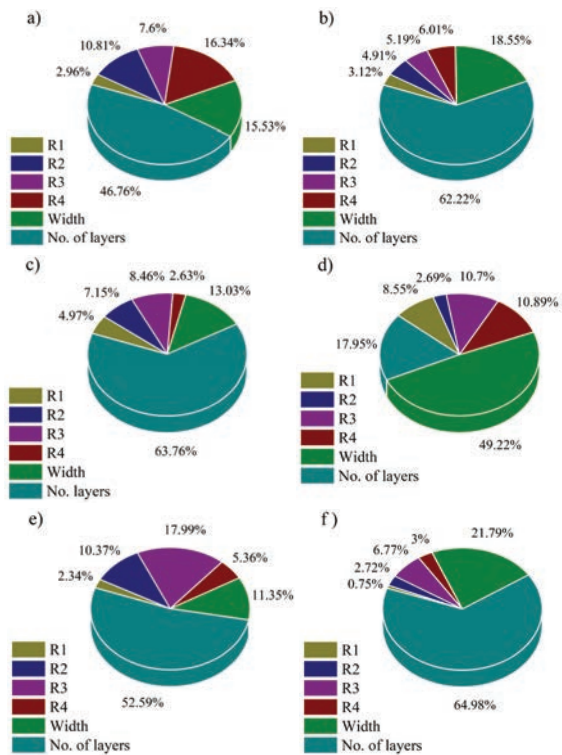


Fig. 14. Relative importance of the design parameters; a) C1 displacement, b) C1 SF, c) C2 displacement, d) C2 SF, e) C3 displacement, f) C3 SF

4 CONCLUSIONS

An optimization procedure that includes CSA and ANN was employed to optimize the design of an RBP with the objective of increasing its displacement to prevent failure through the Tsai-Wu failure criterion. The RBP was made of carbon fibre layers stacked around a core made of ABS. Three carbon fibre layer orientations were tested. For the design of the RBP, the results show that the layers oriented at $0^\circ/90^\circ$ represent the best trade-off between displacement and Tsai-Wu criterion with a reduced number of layers, whereas $-45^\circ/45^\circ$ are not suitable due to imminent failure. The case with combined orientations presented minimal displacement, which would increase its stiffness. The damage was concentrated in the point of contact with the ground and, due to the selection of adequate design parameters, was minimized in the zones of the RBP with a curved shape. The two most important design parameters were the number of layers and the width of the RBP. The developed optimization procedure that combines CSA and ANN reveals a fast technique to improve the design of RBP; in addition, it is feasible to use the proposed manufacture technique for future orthopaedic personalized applications.

4 REFERENCES

- [1] De Luigi, A.J., Cooper, A. (2018). Adaptive sports technology and biomechanics: Prosthetics. *PM&R*, vol. 6, no. 8, p. S40-S57, DOI:10.1016/j.pmrj.2014.06.011.
- [2] Monette, D., Dumond, P., Chikhaoui, I., Nichols P., Lemaire, E.D. (2020) Preliminary material evaluation of flax fibers for prosthetic socket fabrication. *ASME Journal of Biomechanical Engineering*, vol. 143, no. 2, p. 021006, DOI:10.1115/1.4048079.
- [3] Morais, D., Ferreira, Gomes, G., Silveira, M.E., Ancelotti A.C. (2019). Design optimization and development of tubular isogrid composites tubes for lower limb prosthesis. *Applied Composite Materials*, vol. 26, p. 273-297, DOI:10.1007/s10443-018-9692-2.
- [4] Marcellini, A., Ferez, S., Issanchou, D., De Léséleuc, E., Mc Namee, M. (2012). Challenging human and sporting boundaries: The case of Oscar Pistorius. *Performance Enhancement & Health*, vol. 1, no. 1. p. 3-9, DOI:10.1016/j.peh.2011.11.002.
- [5] Jin, Y., He, Y., Shih, A. (2016). Process planning for the fuse deposition modeling of ankle-foot-orthoses. *Procedia CIRP*, vol. 42, p. 760-765, DOI:10.1016/j.procir.2016.02.315.
- [6] Türk, D.-A., Einarsson, H., Lecomte, C., Meboldt, M. (2018) Design and manufacturing of high-performance prostheses with additive manufacturing and fiber-reinforced polymers. *Production Engineering*, vol. 12, p. 203-213, DOI:10.1007/s11740-018-0799-y.
- [7] Tavangarian, F., Proano, C., Zolko, C. (2019). Performance of low-cost 3D printed pylon in lower limb prosthetic device. *TMS 2019 148th Annual Meeting & Exhibition Supplemental Proceedings, The Minerals, Metals & Materials Series*, p. 1207-1215, DOI:10.1007/978-3-030-05861-6_115.
- [8] ISO 10328:2016. *Prosthetics – Structural Testing of Lower-Limb Prostheses – Requirements and Test Methods*. International standard organization, Geneva
- [9] Ouahim, W., Ait-Dahi, M., Bensalah, M.-Q., El Achaby, M., Rodrigue, D., Bouhfid, R., Qaiss, A. (2020). Characterization and numerical simulation of laminated glass fiber-polyester composites for a prosthetic running blade. *Journal of Reinforced Plastics & Composites*, vol. 40, no. 3-4, p. 118-133, DOI:10.1177/0731684420949662.
- [10] Fey, N.P., Klute, G.K., Neptune, R.R. (2011). The influence of energy storage and return foot stiffness on walking mechanics and muscle activity in below-knee amputees. *Clinical Biomechanics*, vol. 26, no. 10, p. 1025-1032, DOI:10.1016/j.clinbiomech.2011.06.007.
- [11] Pérez-Carabaza, S., Scherer, J., Rinner, B., López-Orozco, J.A., Besada-Portas, E. (2019). UAV trajectory optimization for minimum time search with communication constraints and collision avoidance. *Engineering Applications of Artificial Intelligence*, vol. 85, p. 357-371, DOI:10.1016/j.engappai.2019.06.002.
- [12] Yu, Q., Cai, M., Shi, Y., Fan, Z. (2014). Optimization of the energy efficiency of a piston compressed air engine. *Strojniški vestnik - Journal of Mechanical Engineering*, vol. 60, no. 6, p. 395-406, DOI:10.5545/sv-jme.2013.1383.
- [13] Cheng, J., Wang, L., Xiong, Y. (2018). An improved cuckoo search algorithm and its application in vibration fault diagnosis for a hydroelectric generating unit. *Engineering Optimization*, vol. 50, no. 9, p. 1593-1608, DOI:10.1080/0305215X.2017.1401067.
- [14] Joly, M.M., Verstraete, T., Paniagua, G. (2013). Differential evolution based soft optimization to attenuate vane-rotor shock interaction in high-pressure turbines. *Applied Soft Computing*, vol. 13, no. 4, p. 1882-1891, DOI:10.1016/j.asoc.2012.12.005.
- [15] Jouhaud, J.-C., Sagaut, P., Montagnac, M., Laurenceau, J. (2007). A surrogate-model based multidisciplinary shape optimization method with application to a 2D subsonic airfoil. *Computers and Fluids*, vol. 36, no. 3, p. 520-529, DOI:10.1016/j.compfluid.2006.04.001.
- [16] White, D.A., Arrighi, W.J., Kudo, J., Watts, S.E. (2019). Multiscale topology optimization using neural network surrogate models. *Computer Methods in Applied Mechanics and Engineering*, vol. 346, p. 1118-1135, DOI:10.1016/j.cma.2018.09.007.
- [17] Fan, X., Wang, P., Hao, F.F. (2019). Reliability-based design optimization of crane bridges using Kriging-based surrogate models. *Structural and Multidisciplinary Optimization*, vol. 59, p. 993-1005, DOI:10.1007/s00158-018-2183-0.
- [18] Francisco, M.B., Junqueira, D.M., Oliver, G.A., Junho Pereira, J.L., da Cunha, S.S.Jr.Jr., Gomes, G.F. (2020). Design optimizations of carbon fibre reinforced polymer isogrid lower limb prosthesis using particle swarm optimization and

- Lichtenberg algorithm. *Engineering Optimization*, p. 1-24, DOI:10.1080/0305215X.2020.1839442.
- [19] Zhai, Y., Liang, S. (2017). Optimal lay-ups to maximize loss factor of cross-ply composite plate. *Composite Structures*, vol. 168, p. 597-607, DOI:10.1016/j.compstruct.2017.01.019.
- [20] Hobara, H., Baum, B.S., Kwon, H.-J., Linberg, A., Wolf, E.J., Miller, R.H., Shim, J.K. (2014). Amputee locomotion: Lower extremity loading using running-specific prostheses. *Gait & Posture*, vol. 39, no. 1, p. 386-390, DOI:10.1016/j.gaitpost.2013.08.010.
- [21] Askarzadeh, A. (2016). A novel metaheuristic method for solving constrained engineering optimization problems: Crow search algorithm. *Computers & Structures*, vol. 169, p. 1-12, DOI:10.1016/j.compstruc.2016.03.001.
- [22] Clayton, N., Emery, N. (2005). Corvid cognition. *Current Biology*, vol. 15, no. 3, p. R80-R81, DOI:10.1016/j.cub.2005.01.020.
- [23] Giustolisi, O., Laucelli, D. (2005). Improving generalization of artificial neural networks in rainfall-runoff modelling. *Hydrological Sciences Journal*, vol. 50, no. 3, p. 457, DOI:10.1623/hysj.50.3.439.65025.
- [24] Koopialipoor, M., Ghaleini, E.N., Haghighi, M., Kanagarajan, S., Maarefvand, P., Mohamad, E.T. (2019). Overbreak prediction and optimization in tunnel using neural network and bee colony techniques. *Engineering with Computers*, vol. 35, no. 4, p. 1191-1202, DOI:10.1007/s00366-018-0658-7.
- [25] Tanzifi, M., Hosseini, S.H., Kiadehi, A.D., Olazar, M., Karimipour, K., Rezaiemehr, R., Ali, I. (2017). Artificial neural network optimization for methyl orange adsorption onto polyaniline nano-adsorbent: Kinetic, isotherm and thermodynamic studies. *Journal of Molecular Liquids*, vol. 244, p. 189-200, DOI:10.1016/j.molliq.2017.08.122.
- [26] Afram, A., Janabi-Sharifi, F., Fung, A.S., Raahemifar, K. (2017). Artificial neural network (ANN) based model predictive control (MPC) and optimization of HVAC systems: A state of the art review and case study of a residential HVAC system. *Energy and Buildings*, vol. 141, p. 96-113, DOI:10.1016/j.enbuild.2017.02.012.
- [27] Tsai, S.W., Wu, E.M. (1971). A general theory of strength for anisotropic materials. *Journal of Composite Materials*, vol. 5, no. 1, p. 58-80, DOI:10.1177/002199837100500106.
- [28] Rahman, M., Bennett, T., Glisson, D., Beckley, D., Khan, J. (2014). Finite element analysis of prosthetic running blades using different composite materials to optimize performance. *ASME International Mechanical Engineering Congress and Exposition*, vol. 10, DOI:10.1115/IMECE2014-37293.
- [29] Beck, O.N., Taboga, P., Grabowski, A.M. (2016). Characterizing the mechanical properties of running-specific prostheses. *PLOS ONE*, vol. 11, no. 12, p. 1-16, DOI:10.1371/journal.pone.017376.
- [30] Kayri, M. (2016). Predictive abilities of Bayesian regularization and Levenberg-Marquardt algorithms in artificial neural networks: A comparative empirical study on social data. *Mathematical and Computational Applications*, vol. 21, no. 2, p. 1-11, DOI:10.3390/mca21020020.
- [31] Blaifi, S., Moulahoum, S., Taghezout, B., Saim A., (2019). An enhanced dynamic modeling of PV module using Levenberg-Marquardt algorithm. *Renewable Energy*, vol. 135, p. 745-760, DOI:10.1016/j.renene.2018.12.054.
- [32] Bonakdari, H., Sheikh Khozani, Z., Zaji, A.H., Asadpour, N. (2018). Evaluating the apparent shear stress in prismatic compound channels using the genetic algorithm based on multi-layer perceptron: A comparative study. *Applied Mathematics and Computation*, vol. 338, p. 400-411, DOI:10.1016/j.amc.2018.06.016.
- [33] Kong, Y. S., Abdullah, S., Schramm, D., Omar, M. Z., Haris, S.M. (2019). Optimization of spring fatigue life prediction model for vehicle ride using hybrid multi-layer perceptron artificial neural networks. *Mechanical Systems and Signal Processing*, vol. 122, p. 597-621, DOI:10.1016/j.ymsp.2018.12.046.
- [34] Despagne, F., Luc Massart, D. (1998). Neural networks in multivariate calibration. *Analyst*, vol. 123, no. 11, p. 157R-178R, DOI:10.1039/A805562I.
- [35] Garson, G.D. (1991). Interpreting neural-network connection weights. *AI Expert*, vol. 6, 47-51.
- [36] Rosel-Solis, M., Molina-Salazar, J., Dávalos-Ramírez, J.O., Pimentel-Mendoza, A.B., Vega, Y. (2019). Analysis of characteristics of composite materials built on abs cores prepared by additive manufacturing. *DYNA Ingeniería e Industria*, vol. 94, no. 3, p. 286-291, DOI:10.6036/8980.

Reduction of Stresses and Mass of an Engine Rubber Mount Subject to Mechanical Vibrations

Omar Dávalos¹ – Uzziel Caldiño-Herrera¹ – Delfino Cornejo-Monroy¹ –
Oscar Tenango-Pirin¹ – Juan Carlos García^{2,*} – M.A. Basurto-Pensado²

¹Universidad Autónoma de Ciudad Juárez, México

²Centro de Investigación en Ingeniería y Ciencias Aplicadas, Universidad Autónoma del Estado de Morelos, México

A rubber engine mount (EM) is a mechanical coupling between the engine and the chassis, and its main function is to diminish, in the chassis, the amplitude of vibrations caused for the engine operation. Such vibrations cause discomfort for vehicle passengers and reduce the EM lifetime. To increase the comfort of vehicle passengers and the lifetime of the EM, this paper presents an EM optimization by means of reducing three main criteria: the EM mass, the displacements transmitted to the chassis, and the mechanical stress in the EM rubber core. For carrying out the EM optimization, the optimum global determination by linking and interchanging kindred evaluators (GODLIKE), assisted by artificial neural networks (ANN) and finite element method (FEM), was used. Because of the optimization process, a reduction greater than 10 % was achieved in the three criteria in comparison with a baseline design. The frequency responses were compared and showed that although the optimization was carried out for the range of 5 Hz to 30 Hz the trend of reduced responses continues beyond this range. These results increased the comfort of vehicle passengers and the lifetime of the EM; in addition, the reduction of mass diminishes its production costs.

Keywords: multi-objective optimization, vehicle engine mount, ANN, FEM, global optimum determination

Highlights

- An engine mount (EM) was optimized using the integration of optimization algorithms, ANN, and FEM.
- For the EM optimization, the global optimum determination by linking and interchanging kindred algorithm was used.
- The optimization is focused on the reduction of EM mass, displacements, and stress responses under mechanical vibration.
- The engine operation frequencies were obtained via experimental measurements.
- The errors of ANN model predictions were less than 5 %.
- The FEM model was validated by the experimental measurements of natural frequencies.

0 INTRODUCTION

A current trend in the automotive industry is the tendency to downsize the components to increase vehicle power capacity, to simplify the manufacturing process and reduce production costs, among other features. This downsizing is only possible if the modifications do not compromise passenger comfort or affect the performance of the automotive systems. Thus, there is a simultaneous need to find automotive components susceptible to improvements and strategies capable of optimizing new designs. One of these automotive parts is the EM, whose main function includes the attenuation of engine vibrations, by means of the reduction of stiffness, and to support the weight of the engine [1] and [2].

The EM consists of a cylindrical steel structure fixed to a rubber core, and it is exposed to forced vibrations caused by the engine operation [3] to [5]. The forced vibrations could cause failure due to fatigue of the EM rubber core, limiting the EM lifetime to five or six years at most. It should be noted that the damage caused by the cyclic load on the steel section of the EM parts is minimal [6] and [7]. Under these

conditions, a good design of an EM mainly involves the reduction of the displacements transmitted from engine to chassis, the increasing of the lifetime through the reduction of mechanical stresses and the reduction of weight. This is a complicated task due to the interaction of the design variables. Heuristic optimization techniques are a good option when solving this type of engineering problems.

Researchers in different engineering fields have analysed these types of problems using optimization techniques. Pérez-Carabaza et al. [8] optimized the trajectory of an unmanned aerial vehicle using search algorithms of minimum time. Daróczy et al [9] optimized the aerofoil geometry of an H-rotor employing computational fluid dynamics and genetic algorithms; they increased the H-rotor power coefficient from 0.40 to 0.48. Cheng et al. [10] improved a cuckoo search algorithm applied to vibration fault diagnosis. In another study [11], a soft optimization based on differential evolution was applied to attenuate the vane-rotor shock interaction in high-pressure turbines. They achieved attenuation above 60 % without stage-efficiency abatement. Rai and Barman [12] applied simulated annealing and real

*Corr. Author's Address: Universidad Autónoma del Estado de Morelos, Av. Universidad 1001, Cuernavaca, Mor., México, jcgarcia@uaem.mx

coded genetic algorithms to optimize the design of a spur gear. They obtained reductions of 14.1 % and 16.6 % of material by using the simulated annealing algorithm and the real coded genetic algorithm, respectively. In [13], the non-dominated sorting genetic algorithm was used to improve the efficiency, and the output power of a piston compressed air engine. They obtained, as an optimized result, an efficiency of 31.17 % when the output power was 2 kW. However, for the case of multi-objective optimization problems, GODLIKE has been used to find one common optimal solution [14].

Regarding EM optimization, several works have employed heuristic techniques. In Ahn et al. [15] an optimization of an EM, by means of an enhanced genetic algorithm with a simplex method and sequential quadratic programming, was employed. The aim of the study was to reduce both the notch depth and the resonance peaks. Both algorithms converged in the presence of selected constraints for the design parameters which improved the forces of transmission to the vehicle by about 30 % due to reduction of notch depth and resonance peaks. Lee and Kim [16] used a micro-genetic algorithm, ANN, and FEM to reduce the mechanical stresses and to increase the life cycles of an elastomeric EM. They obtained a 24 % reduction of stresses and an increment greater than 100 % in the fatigue life cycles. Furthermore, they compared their results against a simple genetic algorithm (GA), showing that a micro-GA performs better than a simple GA. In Zhao et al. [17], a topological optimization was performed to reduce the weight of an EM, maximizing the natural frequencies and increasing the life cycles. They obtained 1.5×10^6 cycles, more than three times the initial target. Alvarado-Iniesta et al. [18] used memetic genetic programming to optimize an engine mount under static load conditions, using a surrogate method and FEM. They reported a reduction of EM weight and stresses.

In this work, a multi-objective design optimization of an EM is proposed using GODLIKE assisted by ANN and FEM. The optimization aim was to reduce the mass of the EM and to reduce the displacements and stresses under mechanical vibrations. Three objective functions were defined, including a target and a penalty factor for each objective function. Experimental measurements were accomplished to identify the mechanical vibration frequency range of the engine; later, this range was used as a boundary condition in commercial FEM software to perform frequency response simulations. ANN was used as a surrogate method within GODLIKE to predict the rubber core mass,

displacement, and stress responses. The ANN was trained with a database generated from a central composite design of the experiments. Measurement of the EM natural frequency was used to validate the numerical model, and this was used to compute the EM frequency response using FEM. This multi-objective optimization is a novel way to link three different algorithms (GODLIKE, ANN, and FEM) to improve its performance and reach a fast optimization methodology of EM, considering stress and displacement responses under mechanical vibrations. Using another way for the optimization process, the calculation of these responses requires a large amount of time for the numerical computations. However, in this multi-objective optimization algorithm, to reduce the computation time, a surrogate method, like ANN, is employed. Thus, the cases of FEM computations are reduced according to the size of the database used in ANN training. Furthermore, the ANN database was constructed using a design of experiments which is helpful in attaining convergence, further reducing the time of optimization. The proposed optimization methodology is applied to a specific EM model, however; the methodology can be applied to other EM types considering its characteristics.

1 METHODS

1.1 Optimization Methodology

This work is focused on the numerical optimization of an EM, but the manufacturing of the optimized EM is out of the scope. The EM used in this investigation is located on the front right side of a 4-cylinder, 2.4 L Toyota internal combustion engine. One of its sides is attached to the chassis, and the other side supports the engine. The materials of which it is made are steel and rubber. The steel portion of the EM includes a cylindrical cover, a ring between the cylindrical cover and the rubber core, and a metal bushing between the rubber core and the bolt that fixes the engine. The rubber core has two lobe-shaped holes, one lateral tip at each side and a conical-shape around the metal bushing. The typical failure of the EM occurs in the rubber core. The crack propagation path extends along the neck of the lobe and around the conical shape, as shown in Fig. 1. Generally, the damage in the EM steel parts is negligible.

The sequence of the optimization methodology is shown in Fig. 2. First, the frequencies of the forced vibration caused by the engine operation are gotten through experimental measurements. These measured frequencies will show the range of the EM



Fig. 1. Failed of the rubber core in an EM

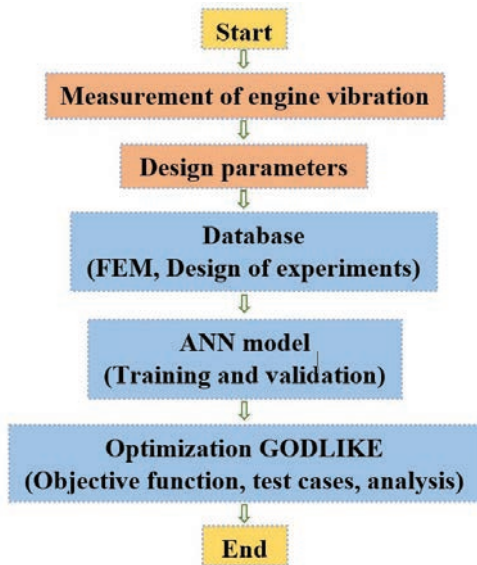


Fig. 2. Optimization methodology

excitation frequencies in which responses will be computed. Then, the design parameters are defined based on the EM geometry and the optimization requirements, which are the reduction of three criteria: EM mass, displacement response, and stress response. Afterwards, a database is generated using a central composite design of experiments and the values of stress and displacement to complete the database are computed using frequency response analysis through FEM simulations. Once the database was generated, it was used for the training and the validation of an ANN model, which could accurately predict the rubber core mass and both displacement and stress responses. The final part is the application of the GODLIKE algorithm in the optimization of the design

of the EM. The detailed description of each part of the optimization methodology is presented in the next sections.

1.2 Measurement of Engine Mechanical Vibrations

A triaxial G-Link-200 Microstrain® wireless accelerometer was placed over the engine block (Fig. 3) to measure the acceleration amplitude of engine mechanical vibrations. The acquired signal from the accelerometer was transmitted to a WSDA®-200-USB Microstrain® receiver connected to a personal computer. The acceleration measurements were carried out at 1500 rpm, 2000 rpm, 2500 rpm, 3000 rpm, and ralenti conditions (around 800 rpm to 900 rpm).



Fig. 3. Mounting of the accelerometer over the engine block

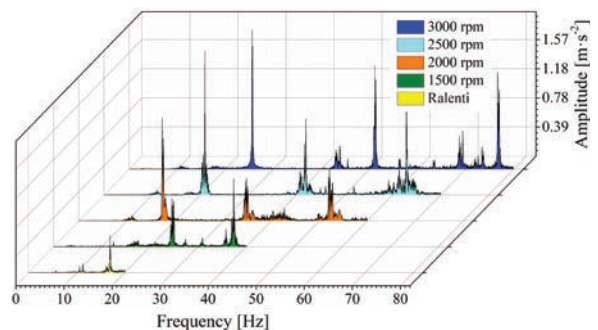


Fig. 4. Engine mechanical vibration spectrum at ralenti, 1500 rpm, 2000 rpm, 2500 rpm, and 3000 rpm

The acceleration signal of engine mechanical vibration in the time domain was converted to the frequency domain using the fast Fourier transform. The results of measured frequencies are presented in Fig. 4. At ralenti, the measured engine frequency was 5.7 Hz and increased with increasing engine revolutions. The maximum frequency was 25.6 Hz

at 3000 rpm. Based on these findings, the frequency range for the FEM computations and optimization was set from 5 Hz to 30 Hz.

1.3 Parameterization

For the EM optimization, only the part that holds the engine was considered since it is where failure occurs within the rubber core element. The metal parts were considered in the optimization process to reduce the total mass of the EM.

A total of eight geometrical variables were selected as design parameters: the outer diameter of the metal ring (V_1), the external diameter of the rubber core (V_2), the internal diameter of the rubber core (V_3), the external diameter of the cylindrical cover (V_4), the separation between the internal diameter of the rubber core and the lateral tip (V_5), the internal diameter of the thickness of rubber wall (V_6), the separation between tips of rubber lobes (V_7) and the base diameter of a rubber cone (V_8) around the metal bushing. Fig. 5 illustrates the location of the design parameters.

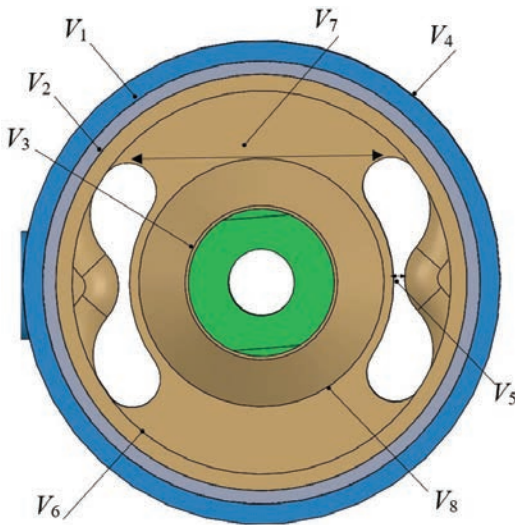


Fig. 5. EM design parameters: $V_1, V_2, V_3, V_4, V_5, V_6, V_7,$ and V_8

The lower and upper limits of the design variables are presented in Table 1. These limits were defined to avoid EM geometry interferences and available space to install EM into the engine bay.

1.4 Database and Frequency Response Analyses

To complete the database for ANN training and validation, the EM geometrical values of Table 1 were

used to compute the frequency harmonic response using FEM by means of Ansys software. In this way, the stress, based on the von Mises stress theory, and displacements responses caused by engine mechanical vibrations were computed. Firstly, a load, considered as sinusoidal, with a frequency range between 5 Hz and 30 Hz with a step of 1 Hz was used. To compute the EM response to higher harmonics excitation, the frequency range was extended until 100 Hz.

Table 1. Design variables bounds

Variable	Lower limit [mm]	Upper limit [mm]
V_1	64	68
V_2	60	64
V_3	20	24
V_4	72	76
V_5	1	3
V_6	57	61
V_7	36	40
V_8	34	40

The frequency response analysis is based on the equation of motion for a mechanical vibration which is written as [19]:

$$[\mathbf{M}]\{\ddot{\mathbf{u}}\} + [\mathbf{C}]\{\dot{\mathbf{u}}\} + [\mathbf{K}]\{\mathbf{u}\} = \{\mathbf{f}(t)\}, \quad (1)$$

where \mathbf{M} is the mass matrix, \mathbf{u} is the nodal displacement vector, \mathbf{C} is the damping matrix, \mathbf{K} is the stiffness matrix, and $\mathbf{f}(t)$ is the forcing vector or the dynamic load applied to EM. This dynamic load is a harmonic function:

$$\mathbf{f}(t) = \mathbf{F} \sin(\omega t), \quad (2)$$

where ω is the frequency and \mathbf{F} is the force vector.

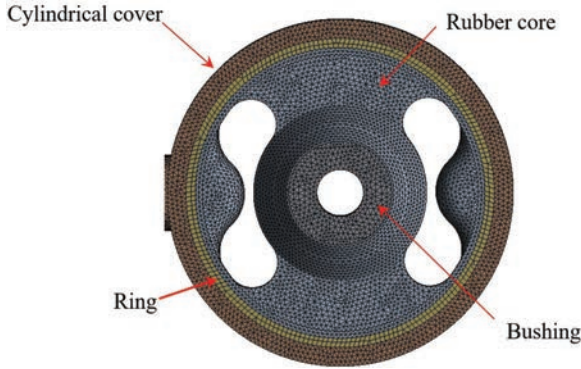
The FEM computations assumed the rubber material as linear elastic to simplify the frequency response study. However, this assumption is limited to small deformations. For this research, to guarantee the validity of the FEM computations, experimental validation with the EM natural frequencies was implemented.

The property of materials, rubber, and metal, are described in Table 2.

The baseline EM model was discretized using tetrahedral elements with sizes between 1.2 mm and 1.8 mm, resulting in 401,613 finite elements (Fig. 6). For each node, six degrees of freedom were considered. For the rest of the EM models of the database, a slight variation in the number of elements is expected due to changes in the design parameters.

Table 2. Properties of materials

Property	Steel	Rubber
Elastic modulus [Pa]	200×10^9	1.5×10^6
Poisson's ratio	0.29	0.45
Density [kg/m ³]	7850	1100

**Fig. 6.** Meshed domain for the EM geometrical model

The total engine weight is distributed and applied as a force among the three EM that support the engine in the engine bay. So, a force of 457.83 N was calculated using the engine mass of 140 kg, and then it was applied at the internal face of the EM bushing. Furthermore, the harmonic response requires applying a dynamic force, which was considered as three times the force applied to EM bushing resulting in a final force of 1373.5 N. Two displacement restrictions were applied, one at the inner face of the bushing of the part bolted to chassis, the second one at the external surface of the cylindrical cover. No sliding or separation was considered for the contact between the EM parts.

The harmonic response analysis was performed in a range of 5 Hz to 30 Hz with frequency steps of 1 Hz. At each frequency step, resultant deformation and stress responses were calculated.

1.5 Artificial Neural Networks

An ANN works as an interpolator in the classification process and static or time-series predictions. A type of feed-forward ANN, widely used in prediction is the multilayer perceptron (MLP), which has an architecture of layers arranged in input, hidden, and output layers. Each layer is composed of a defined number of neurons which, in the case of input and output layers, corresponds to the number of inputs and predicted outputs, respectively. In the case of the hidden layer, the number of neurons is defined by trial and error, until it reaches an acceptable reliability prediction. Each layer is linked to the

next one through weighted connections. To establish nonlinear relationships between inputs and outputs, transfer functions must be added to ANN. A good performance in prediction could be found using the hyperbolic tangent (HT) function between input and hidden layer, whereas between the hidden and output layers, a linear function could be used [20] to [23]. The predicted output is calculated through:

$$y = l \left(\sum_{j=1}^n (w_j^2 \cdot HT_n + b^2) \right), \quad (3)$$

where l is the linear function, w is the weight connection, HT is the hyperbolic tangent transfer function, b is the bias, n is the total number of hidden neurons. The HT is:

$$HT_n = \frac{2}{1 + e^{-2x_n}} - 1, \quad (4)$$

where x is defined as:

$$x_n = \sum_{i=1}^m w_i^1 \cdot in_i + b_j^1, \quad (5)$$

where m is the number of neurons in the input layer. The superscripts 1 and 2 indicate inputs to the hidden layers and outputs from the hidden layers, respectively. Weights and biases coefficients are obtained from the ANN training process and inserted in the above equations to calculate the desired output. The adequate selection of these coefficients is made by a training algorithm. To train, validate, and test the ANN, the database of section 1.4 was used.

In this work, three ANN models were implemented to calculate stress and displacements response at a specified frequency range and, due to the complex shape, the mass of the rubber core of the EM. The architecture of all three models consists of three layers with eight and one neurons at input and output layers, respectively. The model to predict the stress response area has six neurons in the hidden layer, whereas the model for displacements has three neurons, and just two neurons in the hidden layer for the mass prediction. The database to train the ANN consists of 80 design combinations based on a central composite design of experiments and an additional baseline design. This design of experiments was implemented to avoid duplicated information which difficult the ANN learning. The database was constructed by FEM simulations of the harmonic response of EM subjected to excitation frequencies. All design combinations of the database show the same trend increasing displacement and stress responses as frequency increases. The net was trained using the Levenberg-Marquardt algorithm, which has shown

a good prediction performance compared with other training algorithms [24]. The transfer functions used in these models were HT, between input and hidden layer, and linear, between hidden and output layer. Due to the use of HT, the input data were normalized between 0.1 and 0.9 using the next expression [25]:

$$n_i = 0.8 \left(\frac{In_i - In_{\min}}{In_{\max} - In_{\min}} \right) + 0.1. \quad (6)$$

Here n_i is the normalized variable, In_i is the not-normalized variable, and In_{\min} and In_{\max} are the lower and upper range of the design variable.

The performance of the ANN models was evaluated using the estimation of both root mean square error, RMSE, and the correlation coefficient, R^2 , calculated as follows:

$$RMSE = \sqrt{\frac{\sum_{i=1}^T (y_{ANN} - y_{FEM})^2}{T}}, \quad (7)$$

$$R^2 = 1 - \frac{\sum_{i=1}^T (y_{ANN} - y_{FEM})^2}{\sum_{i=1}^T (y_{FEM} - y_{ave})^2}, \quad (8)$$

where y_{ANN} is the output predicted by ANN, y_{FEM} is the output predicted by FEM, y_{ave} is the average of actual values. From the database, 80 % of data were randomly selected to train the net, whereas the rest of the data were used in the validation process. To test the ANN models, eight additional simulations (10 % of the database) were computed to evaluate ANN predictions against FEM calculations.

1.6 Optimization

The proposed optimization is based on the GODLIKE algorithm developed by Oldenhuis and Vandekerckhove [26]. GODLIKE uses four single meta-heuristic algorithms: differential evolution (DE), genetic algorithm (GA), particle swarm optimization (PSO) and adaptive simulated annealing (ASA). In GODLIKE, each algorithm performs the first approach from an initial population. Before starting a second approach, a defined number of members of the firstly optimized population is randomly selected from one algorithm (e.g., DE) and inserted in the population of the remaining algorithms (e.g., GA, PSO, and ASA). The second approach starts until all the algorithms have shared members among them. This process is repeated until a stop condition is met. In this way, the possible poor performance of each algorithm is improved due to the integration of population members from other algorithm approaches.

This link between algorithms is intended to find the global optimum due to the use of populations with the fittest individuals. The use of this methodology requires many objective function evaluations, which increase the computational cost; however, it is offset by the robustness of the algorithm [27].

1.7 Objective Function

A multi-objective optimization works by minimizing or maximizing several objective functions that satisfy a defined set of constraints [28]. The problem can be mathematically written as:

$$\text{minimize} \{f_1(\bar{X}), f_2(\bar{X}), \dots, f_N(\bar{X})\}, \quad (9)$$

subject to; $g_j(\bar{X}) \leq 0$, $h_k(\bar{X}) = 0$, and $x_{lb} \leq x_M \leq x_{ub}$. Here f is the objective function, \bar{X} is a vector that contains the design variables x , g and h are the inequality and equality constraint functions, respectively. The subscript N is the total of objective functions; j , k and M are the amounts of inequalities constraints, equalities constraints, and design variables respectively, whereas l_b and u_b are the lower and upper bounds of the corresponding design variable. When a multi-objective optimization is performed, more than one solution is obtained; these feasible solutions lie on the Pareto-optimal front [29].

In this work, the total mass reduction of the EM was calculated by adding the mass of all its parts: rubber core, ring, metal cover, and the bushing. Due to the complex shape of the rubber core, its mass was computed using an ANN model, whereas the mass of the rest of the components was evaluated as follows:

$$m_{ru} = m_{ru,ANN}, \quad (10)$$

$$m_{ri} = \pi 62.8 (V_1^2 - V_2^2), \quad (11)$$

$$m_{mc} = \pi 62.8 (V_4^2 - V_1^2), \quad (12)$$

$$m_{bu} = \pi 90.275 (V_3^2 - 0.010^2). \quad (13)$$

Here m_{ru} is the mass of the rubber part, and the subscript ANN indicates the rubber mass predicted by means of the neural net. Deformations and stresses vary as functions of the mechanical vibrations and their excitation frequencies. Since the engine works at different frequencies, a method was implemented to evaluate both displacement and stress as response areas considering a frequency step of $S=1$ Hz. The method aims to calculate every response area as an area of a trapezoidal shape formed between two

consecutive frequency steps. For this purpose, the coordinates of four points must be in a plane where frequencies versus response (displacement or stresses) are plotted at the x -axis and y -axis, respectively. The coordinates of the four points are defined by their position at x -axis and y -axis, respectively. For example, in Fig. 7, the displacement response area A is formed by points 1, 2, 3, and 4. The coordinates of point 1 and 2 at the x -axis are the frequency ω at step 1 and frequency $\omega+1$ respectively, whereas at the y -axis its coordinate is 0. The coordinates of points 3 and 4 at the x -axis are the same as in points 1 and 2; at the y -axis, the coordinates correspond to response magnitude at ω and $\omega+1$, respectively. Then, the four points are connected, closing the profile forming a trapezoidal area, which evaluates the response through two consecutive frequencies.

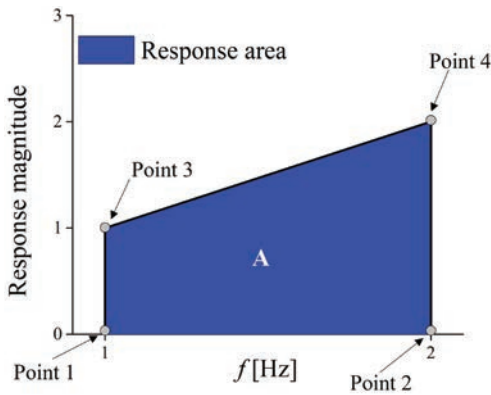


Fig. 7. Definition of coordinates at the response area

The response areas for displacement and stress are calculated using Eqs. (14) and (15) respectively:

$$A_{d\omega} = \frac{d_{\omega+1} + d_{\omega}}{2} s, \quad (14)$$

$$A_{\sigma\omega} = \frac{\sigma_{\omega+1} + \sigma_{\omega}}{2} s, \quad (15)$$

where $A_{d\omega}$ and $A_{\sigma\omega}$ are the areas for displacement and stress responses, respectively, and d and σ are the displacement and stress responses obtained at a specific excitation frequency, ω .

For the optimized design of the EM, a multi-objective optimization was raised. Three objective functions were selected with a set target for each one of them. Penalty factors were added to objective functions to define the relevance of each variable in the optimization process.

Objective functions are expressed in Eqs. (16) to (18). Eq. (16) minimizes the expression to evaluate the mass of the EM, which involves the mass of

rubber part, ring, metal cover, and bushing. Eqs. (17) and (18) are the average of the response areas of displacement and stress, respectively, during the excitation frequencies range.

$$\min f_1 = \left(\frac{m_{ru} + m_{ri} + m_{mc} + m_{bu}}{m_{tar}} \right) (P_{f1}), \quad (16)$$

$$\min f_2 = \frac{A_{d\omega}^{avg}}{A_{d\omega,tar}^{avg}} (P_{f2}), \quad (17)$$

$$\min f_3 = \frac{A_{\sigma\omega}^{ave}}{A_{\sigma\omega,tar}^{ave}} (P_{f3}). \quad (18)$$

Here, $A_{d\omega}^{avg} = \sum_{i=1}^{S-1} A_{d,i} / (S-1)$ is the average area response of displacement, $A_{\sigma\omega}^{avg} = \sum_{i=1}^{S-1} A_{\sigma,i} / (S-1)$ is the area average response of stresses, whereas S is the total number of excitation frequencies. The subscript tar indicates the targets which were set to reach the convergence to the optimized values. The targets were, $m_{tar} = 0.45$ kg, $A_{d,tar} = 0.0035$ m·Hz and $A_{\sigma,tar} = 0.5$ MPa·Hz. The penalty factors are: P_{f1} , P_{f2} and P_{f3} for mass, displacement response and stress response, respectively. In this work, it was assumed that passenger comfort (which is related to the displacement) is the main criterion to consider followed by the resistance of components and finally the mass of the component. Based on these assumptions, the penalty factors were set as follows: 0.15 for mass, 0.60 for displacement and 0.25 for stresses.

1.8 Validation of FEM Model

The FEM model was validated through the measurement of the first natural frequency of the EM. The accelerometer utilized was the same used in the measurements of engine mechanical vibrations. The device was mounted over the EM inside the engine bay. The excitation signal was provided by an impact hammer.

The experimental measurement of EM first natural frequency is shown in Fig. 8. The value of the first natural frequency was 75.015 Hz. The first three natural frequencies from FEM computations are shown in Table 3. The comparison of both the experimental and numerical first natural frequencies shows a good agreement between measured and predicted frequencies with a difference of around 7.5 %. These results guarantee the accuracy of the FEM model and its validity for the optimization of the EM.

Table 3. Natural frequencies calculated by FEM

Natural frequency	Frequency [Hz]
1 st	80.68
2 nd	89.68
3 rd	104.98

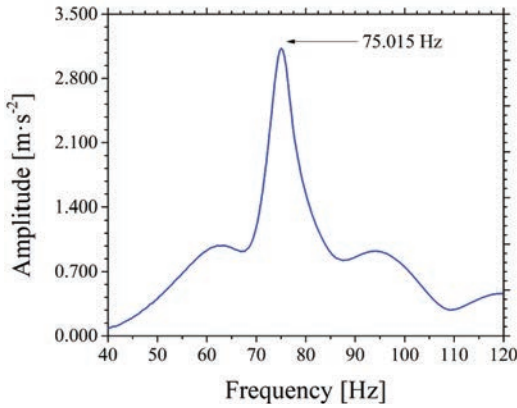


Fig. 8. Experimental measurement of the first natural frequency

2 RESULTS AND DISCUSSION

The results of the ANN computations are presented in Fig. 9. For $A_{\sigma\omega}^{avg}$ training and validation, the correlation coefficient was greater than 0.98, whereas the cases of $A_{d\omega}^{avg}$ and m_{ru} is greater than 0.99. To test the ANN models, eight additional simulations (10 % of the database) were carried out to compare ANN predictions against FEM calculations. In the cases of displacement response and rubber mass computation, the ANN testing predictions have an error below 5%, whereas for stress response prediction the error is slightly greater than 5 %. These results show the capability of the ANN models to predict reliably and ensure its use in the optimization of the EM.

The weights and biases to predict stress response, displacement response and rubber mass are presented in Tables 4 to 6. These coefficients were obtained during ANN training and correspond to the best fit for the three predictions.

In contrast with other works, such as [16] and [18], that have used similar optimization techniques assisted by surrogated methods, this research includes experimental measurements, which guarantee that optimization was performed over operating conditions. Furthermore, considering displacement as an objective function instead of a constraint (as in [16]) allows reducing displacement along with the whole range of engine frequencies.

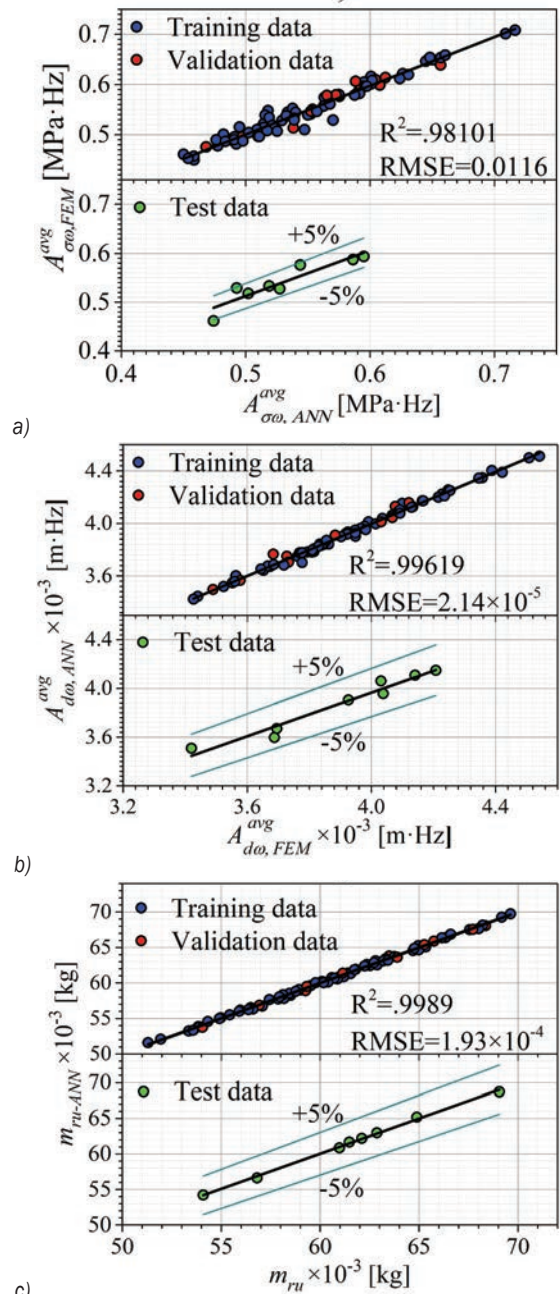


Fig. 9. Results of ANN predictions for

a) $A_{\sigma\omega}^{avg}$, b) $A_{d\omega}^{avg}$ and c) m_{ru}

In Fig. 10, the results of the optimization process are presented. Around 25 % of the Pareto points improve the baseline design. Possible candidates were found with a reduced displacement; nevertheless, their mass was around 0.5 kg which makes them non-feasible candidates. As the $A_{\sigma\omega}^{avg}$ and $A_{d\omega}^{avg}$ reduce their magnitude, more options can be found with a lower mass.

Table 4. ANN coefficients for prediction of area average of stress response

$w_{1,1}^1$	$w_{1,2}^1$	$w_{1,3}^1$	$w_{1,4}^1$	$w_{1,5}^1$	$w_{1,6}^1$	$w_{1,7}^1$	$w_{1,8}^1$
-1.45854	0.96315	-1.82456	-0.49916	-0.45800	5.08531	2.05659	-3.16593
$w_{2,1}^1$	$w_{2,2}^1$	$w_{2,3}^1$	$w_{2,4}^1$	$w_{2,5}^1$	$w_{2,6}^1$	$w_{2,7}^1$	$w_{2,8}^1$
0.98225	2.23806	-1.75895	-1.17739	-2.32274	-1.14974	1.65331	-2.22049
$w_{3,1}^1$	$w_{3,2}^1$	$w_{3,3}^1$	$w_{3,4}^1$	$w_{3,5}^1$	$w_{3,6}^1$	$w_{3,7}^1$	$w_{3,8}^1$
1.39160	-5.58502	-2.39672	-0.12927	-0.05249	1.15514	-0.59857	-1.20014
$w_{4,1}^1$	$w_{4,2}^1$	$w_{4,3}^1$	$w_{4,4}^1$	$w_{4,5}^1$	$w_{4,6}^1$	$w_{4,7}^1$	$w_{4,8}^1$
0.63538	3.30013	-1.19526	-0.09034	-1.41403	-1.35004	-3.69895	-2.78710
$w_{5,1}^1$	$w_{5,2}^1$	$w_{5,3}^1$	$w_{5,4}^1$	$w_{5,5}^1$	$w_{5,6}^1$	$w_{5,7}^1$	$w_{5,8}^1$
-2.83462	-1.74426	1.65473	1.03900	3.66780	-0.30788	-0.69853	2.18040
$w_{6,1}^1$	$w_{6,2}^1$	$w_{6,3}^1$	$w_{6,4}^1$	$w_{6,5}^1$	$w_{6,6}^1$	$w_{6,7}^1$	$w_{6,8}^1$
0.17086	-1.81009	0.84667	0.12948	-2.15127	4.82269	0.90327	-0.18045
$w_{1,1}^2$	$w_{1,2}^2$	$w_{1,3}^2$	$w_{1,4}^2$	$w_{1,5}^2$	$w_{1,6}^2$		
0.03196	-0.07535	0.16155	0.06778	-0.53198	0.12223		
$b_{1,1}^1$	$b_{2,1}^1$	$b_{3,1}^1$	$b_{4,1}^1$	$b_{5,1}^1$	$b_{6,1}^1$		
1.15072	2.51253	0.89235	2.00106	-5.08572	-3.36807		
$b_{1,1}^2$							
0.33196							

Table 5. ANN coefficients for prediction of area average of displacement response

$w_{1,1}^1$	$w_{1,2}^1$	$w_{1,3}^1$	$w_{1,4}^1$	$w_{1,5}^1$	$w_{1,6}^1$	$w_{1,7}^1$	$w_{1,8}^1$
-0.11114	-0.06945	6.66939	-0.11978	0.05504	0.22898	0.31355	-0.27377
$w_{2,1}^1$	$w_{2,2}^1$	$w_{2,3}^1$	$w_{2,4}^1$	$w_{2,5}^1$	$w_{2,6}^1$	$w_{2,7}^1$	$w_{2,8}^1$
0.01930	-0.08350	-0.02500	0.04518	0.03851	-0.53731	0.52415	0.18607
$w_{3,1}^1$	$w_{3,2}^1$	$w_{3,3}^1$	$w_{3,4}^1$	$w_{3,5}^1$	$w_{3,6}^1$	$w_{3,7}^1$	$w_{3,8}^1$
0.01093	3.65897	-1.03528	0.72872	0.91272	-0.74952	0.14733	-0.06379
$w_{1,1}^2$	$w_{1,2}^2$	$w_{1,3}^2$					
-0.00018	-0.00162	0.00010					
$b_{1,1}^1$	$b_{2,1}^1$	$b_{3,1}^1$					
-2.58080	0.32367	-2.47434					
$b_{1,1}^2$							
0.00464							

Table 6. ANN coefficients for rubber mass prediction

$w_{1,1}^1$	$w_{1,2}^1$	$w_{1,3}^1$	$w_{1,4}^1$	$w_{1,5}^1$	$w_{1,6}^1$	$w_{1,7}^1$	$w_{1,8}^1$
0.00051	-0.47488	0.21294	0.00173	0.03700	0.31568	-0.11993	-0.12761
$w_{2,1}^1$	$w_{2,2}^1$	$w_{2,3}^1$	$w_{2,4}^1$	$w_{2,5}^1$	$w_{2,6}^1$	$w_{2,7}^1$	$w_{2,8}^1$
1.11450	2.60450	-0.06103	1.59204	0.57664	-0.56463	-0.80459	-1.36578
$w_{1,1}^2$	$w_{1,2}^2$						
-0.03618	0.000068						
$b_{1,1}^1$	$b_{2,1}^1$						
0.05320	-0.93912						
$b_{1,1}^2$							
0.05983							

Individual results are presented in Table 7. For the optimized case, total reductions of 21.5 %, 12.46 %, and 15.3% were obtained for $A_{\sigma\omega}^{avg}$, $A_{d\omega}^{avg}$ and mass, respectively, regarding the baseline design. These reductions are attributable to the application of targets and penalty factors. $A_{d\omega}^{avg}$ is considered the most important parameter, and it was set with a penalty factor of 60 %; however, the magnitude of its reduction was lower than others resulting in the hardest parameter to optimize.

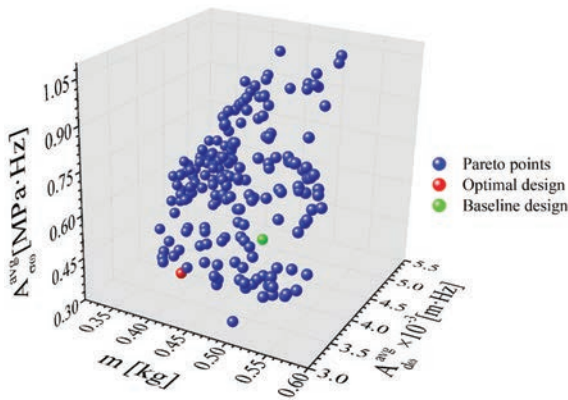


Fig. 10. Pareto points, optimal design found and baseline design

Table 7. Comparison of optimization results of $A_{\sigma\omega}^{avg}$, $A_{d\omega}^{avg}$ and mass

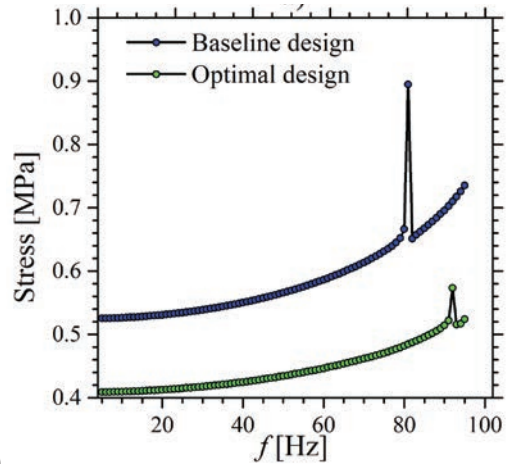
	Baseline design	Optimal design
$A_{\sigma\omega}^{avg}$ [MPa·Hz]	0.53042	0.41632
$A_{d\omega}^{avg}$ [m·Hz]	0.00385	0.00337
mass [kg]	0.49148	0.41628

Table 8. Magnitudes of the baseline and optimized design variables

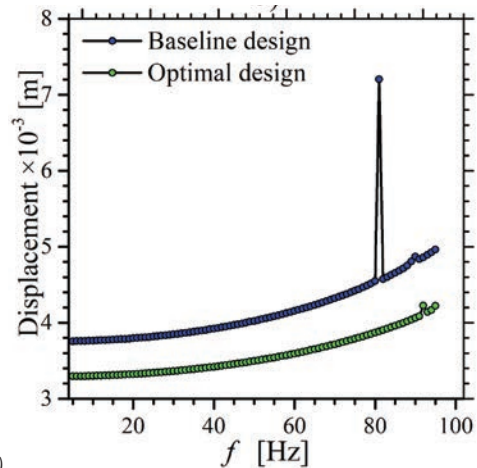
Variable	Baseline design [mm]	Optimal design [mm]
V_1	66	67.404
V_2	62	61.683
V_3	22	22.003
V_4	74	72.189
V_5	2	1.683
V_6	59	57.151
V_7	38	39.63
V_8	37	38.736

In Table 8, the optimized dimensions of EM are presented. The loss of mass is due to the reduction of the thickness of the wall of the cylindrical cover and the internal diameter of ring. The increment of V_1 combined with the reduction of V_2 causes the increment of internal ring wall thickness. Due to the

increment of the ring wall thickness, the movement of the rubber core is restricted, thereby reducing the displacements. The length of V_7 increases the strengthening of the rubber core thus achieving a reduction of the stress response.



a)



b)

Fig. 11. Comparison of responses through the frequency range, a) stress, b) displacement

With the optimized design variables, a new geometrical model, which corresponds to optimized EM, was generated. For such optimized geometry, new computations of the frequency response were performed and compared against the baseline design. In Fig. 11, stress and displacements are plotted against the typical (5 Hz to 30 Hz) and extended (30 Hz to 100 Hz) excitation frequency of the internal combustion engine. The improvement of the optimized EM is outstanding due to the difference in stress and displacement responses between baseline and the optimal design. For the case of the baseline design, the difference between the computed amplitude of displacement response for the initial (5

Hz) and the last (30 Hz) frequencies was 0.0896×10^{-3} m. While for the case of the optimized design, such a difference was reduced to 0.06839×10^{-3} m. Also, the stress response amplitude had a reduction of 35.9 % between the baseline design case and the optimized case. These results are significant when a vehicle is accelerating between this frequency range because, in the case of displacements, a smaller movement will be transmitted to vehicle chassis affecting passenger comfort, whereas, in the case of stresses, its amplitude is minor, reducing the effects of fatigue in the EM. Extending the frequency excitation range, the difference between displacement and stress responses (Fig. 11) for the case of baseline and optimized EM is increased. Also, Fig. 11 shows that the peak which corresponds to the first natural frequency is decreased for the case of the optimized model. This contributes to reducing the amplitude of vibrations of the vehicle chassis in case of resonance at that frequency.

The distribution of stresses at 21 Hz, 2500 rpm, is presented in Fig. 12. Stresses are concentrated in the region near the rubber neck. Fig. 12a shows how the magnitude of stresses is greater than the optimized EM for which a reduction is observed at this zone. Around the external surface of the rubber core, the stresses are lower than in the centre region. A stress line extends out from the front of the neck to the back. Thereby, if a failure occurs, it is expected to be in this zone. These findings are consistent with those presented in Fig. 1, which shows the cracks of a failed EM.

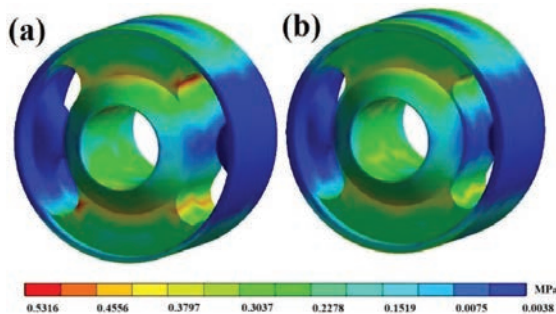


Fig. 12. Comparison of stress distributions at 21 Hz (2500 rpm), a) baseline design, b) optimized design

A comparison of displacements is presented in Fig. 13 at 21 Hz equivalent to 2500 rpm. Maximum displacements are observed in the surface around the bushing and in the cone. In the optimized EM, the displacements are reduced mainly at the sides of the cone and, in a smaller proportion, at the top and bottom.

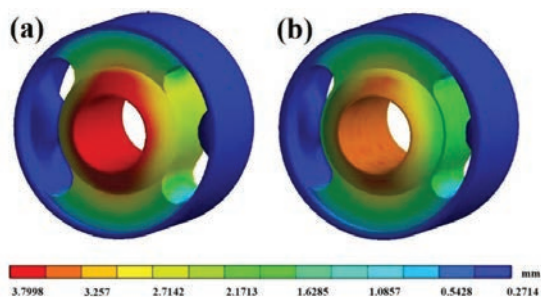


Fig. 13. Comparison of displacement at 21 Hz at 2500 rpm, a) baseline design, b) optimal design

3 CONCLUSIONS

An EM with a rubber core was optimized using a methodology that includes optimization algorithms, ANN and FEM. The optimization is focused on the reduction of EM mass, and both displacements and stresses responses under the excitation of mechanical vibration due to the engine operation. The EM mass has a reduction of 15.3 %, the and were reduced by 21.5 % and 12.46 %, respectively. The target values added in the objective functions were reached, leading the optimization process toward better solutions than a baseline design. A lower magnitude of displacement and stress responses was reached, increasing the ring wall thickness and the distance between lobes in the rubber core, respectively. The reduction of the and means lowering the amplitude of stress and displacements levels in the whole frequencies range, which, in turn, reduces the displacement transmitted from engine to chassis and increases the lifetime of EM. In contrast, the mass reduction decreases production costs. The results from training, testing, and validation of the ANN assure a high confidence level in the predictions. The good definition of ANN models contributes to simplifying the optimization process in this research. The integration of the optimization methodology here presented could be applied for many optimization problems in engineering. The frequency response computation with the extended frequency range shows that the proposed optimization method of averaging both displacement and stress responses is effective because the trend of displacement and stresses response improvement remains continual throughout the extended range.

4 REFERENCES

- [1] Shangguan, W.-B., Liu, X.-A., Lv, Z.-P., Rakheja, S. (2016). Design method of automotive powertrain mounting system

- based on vibration and noise limitations of vehicle level. *Mechanical Systems and Signal Processing*, vol. 76-77, p. 677-695, DOI:10.1016/j.ymsp.2016.01.009.
- [2] Azammi, A.M.N., Sapuan, S.M., Ishak, M.R., Sultan, M.T.H. (2018). Conceptual design of automobile engine rubber mounting composite using triz-morphological chart-analytic network process technique. *Defence Technology*, vol. 14, no. 4, p. 268-277, DOI:10.1016/j.dt.2018.05.009.
- [3] Liu, X.-A., Shangguan, W.-B., Lv, Z.-P., Ahmed, W., Zhu, W. (2017). A study on optimization method of a powertrain mounting system with a three-cylinder engine. *Proceedings of the Institution of Mechanical Engineers, Part C: Journal of Mechanical Engineering Science*, vol. 231, no. 12, p. 2235-2252, DOI:10.1177/0954406216631004.
- [4] Idrees, M., Rajendra Prasad, V.B.S. (2018). Response of rubber based engine mounts with sbr as the core rubber. *IOP Conference Series: Materials Science and Engineering*, vol. 455, p. 012108, DOI:10.1088/1757-899x/455/1/012108.
- [5] Ramachandran, T., Padmanaban, K.P. (2013). Minimization of IC engine rubber mount displacement using genetic algorithm. *The International Journal of Advanced Manufacturing Technology*, vol. 67, p. 887-898, DOI:10.1007/s00170-012-4533-1.
- [6] Tang, N., Soltani, P., Pinna, C., Wagg, D., Whear, R. (2018). Ageing of a polymeric engine mount investigated using digital image correlation. *Polymer Testing*, vol. 71, p. 137-144, DOI:10.1016/j.polymertesting.2018.08.036.
- [7] Kim, W.D., Lee, H.J., Kim, J.Y., Koh, S.-K. (2004). Fatigue life estimation of an engine rubber mount. *International Journal of Fatigue*, vol. 26, no. 5, p. 553-560, DOI:10.1016/j.ijfatigue.2003.08.025.
- [8] Pérez-Carabaza, S., Scherer, J., Rinner, B., López-Orozco, J.A., Besada-Portas, E. (2019). UAV trajectory optimization for minimum time search with communication constraints and collision avoidance. *Engineering Applications of Artificial Intelligence*, vol. 85, p. 357-371, DOI:10.1016/j.engappai.2019.06.002.
- [9] Daróczy, L., Janiga, G., Thévenin, D. (2018). Computational fluid dynamics based shape optimization of airfoil geometry for an H-rotor using a genetic algorithm. *Engineering Optimization*, vol. 50, no. 9, p. 1483-1499, DOI:10.1080/0305215X.2017.1409350.
- [10] Cheng, J., Wang, L., Xiong, Y. (2018). An improved cuckoo search algorithm and its application in vibration fault diagnosis for a hydroelectric generating unit. *Engineering Optimization*, vol. 50, no. 9, p. 1593-1608, DOI:10.1080/0305215X.2017.1401067.
- [11] Joly, M.M., Verstraete, T., Paniagua, G. (2013). Differential evolution based soft optimization to attenuate vane-rotor shock interaction in high-pressure turbines. *Applied Soft Computing*, vol. 13, no. 4, p. 1882-1891, DOI:10.1016/j.asoc.2012.12.005.
- [12] Rai, P., Barman, A.G. (2018). Design optimization of spur gear using SA and RCGA. *Journal of the Brazilian Society of Mechanical Sciences and Engineering*, vol. 40, art. ID 257, DOI:10.1007/s40430-018-1180-y.
- [13] Yu, Q., Cai, M., Shi, Y., Fan, Z. (2014). Optimization of the energy efficiency of a piston compressed air engine. *Strojniški vestnik - Journal of Mechanical Engineering*, vol. 60, no. 6, p. 395-406, DOI:10.5545/sv-jme.2013.1383.
- [14] Sbayti, M., Bahloul, R., BelHadjSalah, H., Zemzemi, F. (2018). Optimization techniques applied to single point incremental forming process for biomedical application. *The International Journal of Advanced Manufacturing Technology*, vol. 95, p. 1789-1804, DOI:10.1007/s00170-017-1305-y.
- [15] Ahn, Y.-K., Kim, Y.-C., Yang, B.-S., Ahmadian, M., Ahn, K.-K., Morishita, S. (2005). Optimal design of an engine mount using an enhanced genetic algorithm with simplex method. *Vehicle System Dynamics*, vol. 43, no. 1, p. 57-81, DOI:10.1080/00423110412331290400.
- [16] Lee, J.S., Kim, S.C. (2007). Optimal design of engine mount rubber considering stiffness and fatigue strength. *Proceedings of the Institution of Mechanical Engineers, Part D: Journal of Automobile Engineering*, vol. 221, no. 7, p. 823-835, DOI:10.1243/09544070JAUTO433.
- [17] Zhao, Q., Chen, X., Wang, L., Zhu, J., Ma, Z.-D., Lin, Y. (2015). Simulation and experimental validation of powertrain mounting bracket design obtained from multi-objective topology optimization. *Advances in Mechanical Engineering*, vol. 7, no. 6, p. 1-10, DOI:10.1177/1687814015591317.
- [18] Alvarado-Iniesta, A., Guillen-Anaya, L.G., Rodríguez-Picón, L.A., Neco-Caberta, R. (2020). Multi-objective optimization of an engine mount design by means of memetic genetic programming and a local exploration approach. *Journal of Intelligent Manufacturing*, vol. 31, p. 19-32, DOI:10.1007/s10845-018-1432-9.
- [19] Thorby, D. (2008). *Structural Dynamics and Vibration in Practice*, Thorby, D. (ed.), Butterworth-Heinemann, Oxford, p. 77-97.
- [20] Bartecski, K. (2013). A general transfer function representation for a class of hyperbolic distributed parameter systems. *International Journal of Applied Mathematics and Computer Science*, vol. 23, no. 2, p. 291-307, DOI:10.2478/amcs-2013-0022.
- [21] Bonakdari, H., Khozani, Z.S., Zaji, A.H., Asadpour, N. (2018). Evaluating the apparent shear stress in prismatic compound channels using the genetic algorithm based on multi-layer perceptron: A comparative study. *Applied Mathematics and Computation*, vol. 338, p. 400-411, DOI:10.1016/j.amc.2018.06.016.
- [22] Kong, Y.S., Abdullah, S., Schramm, D., Omar, M.Z., Haris, S.M. (2019). Optimization of spring fatigue life prediction model for vehicle ride using hybrid multi-layer perceptron artificial neural networks. *Mechanical Systems and Signal Processing*, vol. 122, p. 597-621, DOI:10.1016/j.ymsp.2018.12.046.
- [23] Durodola, J.F., Ramachandra, S., Gerguri, S., Fellows, N.A. (2018). Artificial neural network for random fatigue loading analysis including the effect of mean stress. *International Journal of Fatigue*, vol. 111, p. 321-332, DOI:10.1016/j.ijfatigue.2018.02.007.
- [24] Hamzaoui, Y.E., Hernández, J.A., Silva-Martínez, S., Bassam, A., Álvarez, A., Lizama-Bahena, C. (2011). Optimal performance of cod removal during aqueous treatment of alazine and gesaprim commercial herbicides by direct and inverse neural network. *Desalination*, vol. 277, no. 1-3, p. 325-337, DOI:10.1016/j.desal.2011.04.060.

- [25] Despagne, F., Massart, D.L. (1998). Neural networks in multivariate calibration. *Analyst*, vol. 123, no. 11, p. 157R-178R, DOI:10.1039/A805562I.
- [26] Oldenhuis, R., Vandekerckhove, J. (2009). Godlike: A Robust Single- & Multi-Objective Optimizer. from <http://www.mathworks.co.uk/matlabcentral/fileexchange/24838-godlike-a-robust-single-multi-objective-optimizer>, accessed on 2013-04-19.
- [27] Sbayti, M., Bahloul, R., BelHadjSalah, H., Zenzemi, F. (2018). Optimization techniques applied to single point incremental forming process for biomedical application. *The International Journal of Advanced Manufacturing Technology*, vol. 95, p. 1789-1804, DOI:10.1007/s00170-017-1305-y.
- [28] Coello Coello, C., Lamont, G.B., Van Veldhuizen, D.A. (2007). *Evolutionary Algorithms for Solving Multi-Objective Problems*. Springer, New York, DOI:10.1007/978-1-4757-5184-0.
- [29] Lim, J., Jang, Y.S., Chang, H.S., Park, J.C., Lee, J. (2020). Multi-objective genetic algorithm in reliability-based design optimization with sequential statistical modeling: An application to design of engine mounting. *Structural and Multidisciplinary Optimization*, vol. 61, p. 1253-1271, DOI:10.1007/s00158-019-02409-1.

Residual Stress and Deformation Analy is in Machining Split Straight Bevel Gears

Bin Wang^{1,2} – Chenxiao Yan^{1,*} – Jubo Li¹ – Peiyao Feng³ – Shuaipu Wang¹ – Shuo Chen¹ – Jianxin Su¹

¹Henan University of Science and Technology, School of Mechatronics Engineering, China

²Collaborative Innovation Center of Machinery Equipment Advanced Manufacturing, China

³Xinxiang Aviation Industry (Group) Co., China

In the machining of split straight bevel gears, the stiffness changes and internal stress are redistributed, which leads to serious deformation of the gear blank after machining. To rectify this problem, a finite element model is established by transforming the processing information of the gear blank into the finite element simulation calculation information, and the gear machining simulation of split straight bevel gear is carried out. Considering the material, design, and machining process of the gear blank, the characteristics and laws of internal stress variation during the gear machining are studied, and the internal mechanism and deformation law of split straight bevel gear are explored. Finally, the gear machining experiment, and the gear blank measurement are carried out. The results show that the deformation law of simulation is consistent with that of the experiment and the deformation characteristics of the split straight bevel gear are consistent with the change law of initial residual stress.

Keywords: split straight bevel gear, residual stress, machining deformation, finite element model, deformation measurement

Highlights

- The finite element model for deformation prediction of the split straight bevel gear is established, and the results of finite element calculation are in good agreement with the experimental results.
- In the process of gear cutting, the change of initial residual stress near the upper and lower surfaces is the greatest, and the change and redistribution of stress is independent of the cutting tooth sequence.
- In the inner of the machined tooth, the tensile and compressive stress in the X-direction decreases significantly, while the stress in the Y-direction changes little. The performance and change of Z-direction stress in the whole machining process are relatively minor.
- The Z-direction bending deformation in the middle of split straight bevel gear is the largest, the deformation at the outer is larger than that at the inner, and the difference of deformation between the outer and inner is especially obvious in the middle.
- The X-direction deformation of the split straight bevel gear basically does not change in the face-width direction, and the closer to the middle of length direction, the smaller the deformation is.
- The deformation in Y-direction is smaller in the middle position, the deformation is slightly different in the face-width direction, and the deformation at wider end of a single tooth (an outer) is slightly greater than that at (the narrower end of a single tooth (an inner)).

0 INTRODUCTION

An oversize straight bevel gear is one of the most important parts in large-scale heavy industrial equipment. It is widely used in mining, power generation and other important fields. An extra-large bevel gear (wheel, diameter greater than 3000 mm) requires a higher forming method and machining equipment, and its manufacturing cost is high, its manufacturing cycle is long, and its machining is very difficult [1] and [2]. The structural stiffness of the entire oversize straight bevel gear is small and is easily deformed during machining and assembly, and the machining is often limited by the size of the equipment. Therefore, the existing extra-large straight bevel gear mostly uses a split structure [3] and [4]. According to the engineering practice and existing research data, the bending deformation of the split straight bevel

gear is the most obvious after machining, which can reach several millimetres [5] and [6]. The deformation of the split gear blank mainly depends on two aspects: one is the deformation created by the stiffness change and internal stress caused by material removal, which accounts for 92.2 % of the total deformation [7] to [9], and the structural deformation caused by surface stress, which only accounts for 7.8 % [10] and [11]. Therefore, this paper focuses on the study of machining deformation caused by the change of internal stress, and the influence of surface processing stress, cutting heat, and workpiece clamping on the deformation is not studied. The oversize straight bevel gear is divided first, and then the teeth are cut. In existing engineering practice, there is a lack of effective theoretical guidance, which leads to great blindness and randomness.

Regarding the machining deformation of large-scale parts, the existing research mainly focuses on the numerical control machining deformation, deformation mechanism and deformation prediction of aviation structure components, frame-shaped components and ring form thin-walled components. Based on theoretical calculation and finite element simulation, Sun and Ke [12] studied the influence of the initial internal stress on the machining deformation of large whole components. Wu [13] explored the machining deformation principle of thin-walled components from the machining principle and finite element simulation. Lu [14] comprehensively considered the effects of initial internal stress, machining stress, temperature change and clamping stress on the deformation of frame-shaped integral components and established a deformation prediction model. Cheng et al. [7] aimed at the milling deformation behaviour of aviation frame-shaped integral components, based on the restart analysis principle, the milling process was simulated, and a calculation system was established. Zhou [15] established a finite element model to predict the deformation of ring thin-walled components, analysed the influence of machining stress on machining accuracy, and predicted the relationship between the amount of material removed and machining error. Huang [16] used theoretical calculation to analyse the stiffness change, internal stress distribution and deformation during machining, and established the deformation prediction model of integral components. Nervi [17] established a machining deformation prediction model of components with initial internal stress and analysed the relationship between the distribution of initial internal stress and the deformation. Wu et al. [18] put forward a quasi-symmetric machining method to reduce the deformation by using the M-symmetry distribution law of residual stress. The deformation mechanism of milling residual stress is studied and compared with the finite element method. Zhang et al. [19] analysed the welding sequence, stress distribution and deformation of vacuum vessels and carried out finite element modelling. Keith [20] studied the influence of machining stress on the machining deformation of components. Ratchev et al. [21] established a mathematical model to predict the machining deformation of thin-walled components on the basis of a neural network, and predicted the machining error. Bremec and Kosel [22] presented an experimental determination of the buckling load and the buckling coefficient of a circular, annular plate with constant thickness, which is made of an elastic-plastic hardening material.

To summarize, focusing on the machining of split straight bevel gear, this paper intends to carry out the research from the following aspects: Firstly, according to the actual distribution law of internal stress and the structural characteristics of the gear blank, the finite element modelling is carried out. Secondly, the distribution law and evolution process of the internal stress in the inner, upper and lower surface of the wheel blank were studied by simulation processing. Thereafter, the deformation forms, characteristics and evolution process of the split gear blank in machining, as well as the relationship between the deformation and machining, and the thickness of the gear blank are studied. Finally, the machining and measuring experiments of split straight bevel gear are carried out, and the finite element model and deformation analysis are verified.

1 RESIDUAL STRESS EVOLUTION IN GEAR CUTTING

1.1 Finite Element Model of Split Straight Bevel Gear

According to the existing data and stress measurement equipment in the laboratory, the aluminium alloy 7075-t7451 is to be used in the experiment of this study. The distribution of residual stress is illustrated in Fig. 1. The length direction (rolling direction) of a split gear blank is set as the X-direction, the transverse direction is the Y-direction, from outer to inner is positive, along the thickness of gear blank is the Z axis, the direction is vertical upward.

Fig. 1 indicates that the residual stress curves in X- and Y-directions along the gear blank thickness are approximate to "M" shape, and the curves are symmetrical about the neutral axis in the thickness direction of the cross-section. There is a large compressive stress near the upper and lower surfaces of the gear blank; the maximum compressive stress in the X-direction is -17.21 MPa and that in Y-direction is -13.27 MPa. The maximum tensile stress in the X- and Y-directions is 20mm away from the middle surface of the gear blank; the maximum tensile stress in the X-direction is 16.21 MPa, and that in the Y-direction is 13.84 MPa. It should be pointed out that the large gear blank is rectangular after cutting. When the balance of three normal stress components of internal stress changes in the process of gear cutting, the dimension expansion occurs in the direction of length, width and height, but the absolute value of the change in the direction of thickness is far less than that in the direction of length and width. Simultaneously, because the cross-sectional area in the thickness direction is

the largest, the bending stiffness is also the largest, and the deformation caused by the internal stress in the Z-direction is very small. Also, the deformation of extra-large split gear in the cutting process is at the millimetre level, so the deformation caused by internal stress in Z-direction can be ignored; therefore, this paper only analyses the internal stress in the X- and Y-directions.

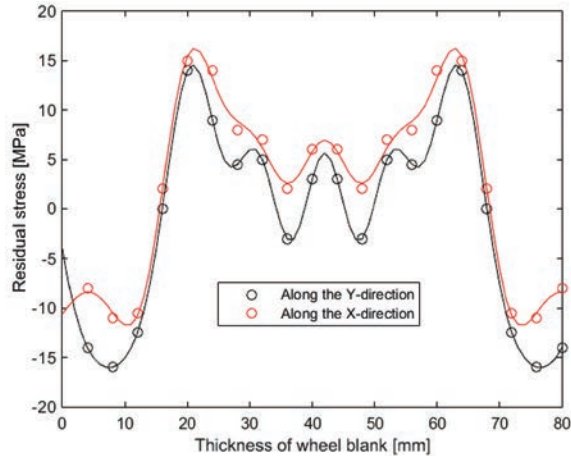


Fig. 1. Initial residual stress curve

For the wheel of extra-large straight bevel gear, the root angle is very large, the cross-section of the gear blank is approximately rectangular. Due to the large diameter and small curvature of the gear blank, and the entire gear blank is divided into several segments; each segment is similar to a cuboid. In the ABAQUS environment, the three-dimensional model of the split straight bevel gear is established according to its structural characteristics. The mesh element type is 20 node quadric hexahedral C3D20R, and the grid division is “structure”. In the “grid” module, a certain number of local seeds are arranged along the thickness direction of gear blank, so the grid along the thickness direction is divided into several layers, and the thickness of each layer is 2 mm. The rigid displacement of gear blank is limited to ensure the accuracy of simulation results. In order to obtain the machining deformation, the split gear blank must be free to deform in the simulation processing. In order to achieve the correct simulation effect, the initial stress of the gear blank material needs to be applied to the finite element model.

According to Fig. 1, the discrete data are input into MATLAB, and Fourier curve fitting is carried out. The relationship between the initial residual stress in two directions and the gear blank thickness is expressed by function respectively,

$$\begin{aligned} \sigma_x &= 0.59 + \sum_{i=1}^5 a_i \cos[i \cdot 0.08(z + 2)] \\ &\quad + \sum_{i=1}^5 b_i \cos[i \cdot 0.08(z + 2)], \\ \sigma_y &= 2.65 + \sum_{i=1}^4 c_i \cos[i \cdot 0.07(z + 2)] \\ &\quad + \sum_{i=1}^4 d_i \cos[i \cdot 0.07(z + 2)], \end{aligned} \quad (1)$$

in Eq. (1), z is the gear blank thickness, a_i, b_i, c_i, d_i are the calculated coefficients obtained by fitting.

With the function expression obtained by fitting, the SIGINI subroutine is programmed in Visual Studio with Fortran language. The SIGINI subroutine will be called by the finite element software in the calculation process to realize the automatic continuous application of the initial residual stress. The gear blank with initial internal stress [MPa] is shown in Fig. 2.

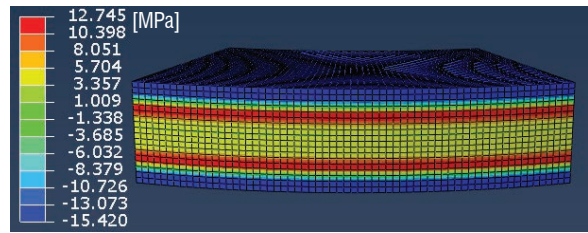


Fig. 2. Finite element model of split gear blank

After the establishment of the finite element model, the “life and death element” technology of the “interaction” module in the simulation software is used to simulate the dynamic process of cutting teeth. Firstly, the element that needs to be “killed” in the finite element model is separated from other element regions. Secondly, multiple analysis steps can be created for the processing of multiple grooves of the split wheel blank, and the removed elements can be “killed” in the corresponding analysis steps. By adjusting the unit “kill” sequence, the simulation effect of multiple cutting sequences can be achieved.

1.2 Internal Stress Evolution in Tooth Machining

In the finite element analysis, the module of gear is set as 20, the number of teeth is 60, the facewidth is 100 mm, the thickness of the gear blank is 80 mm, and 1/10 of the circumference of the whole gear is taken as the split gear blank of the simulation.

1.2.1 Stress Analysis in X-direction

Before the simulation machining, on the gear blank section in the length direction, the X-direction stress nephogram is illustrated as Fig. 3. After the simulation, observe the gear blank section in the same direction; the X-direction stress nephogram shown as Figs. 4 and 5. Fig. 4 shows that all the tooth spaces are machined from left to right in turn, and Fig. 5 shows that the machining starts from the middle of the gear blank.

The section view of the facewidth direction and the X-direction stress nephogram is indicated in Fig. 6. Fig. 6a shows the stress nephogram before gear cutting, Fig. 6b shows the stress nephogram of the section from the topline, and Fig. 6c shows the stress nephogram of the section from the tooth space bottom.

The results indicate that the X-direction internal stress of the material adjacent to the gear cutting area changes greatly during the gear cutting. The largest X-direction stress change occurs at the bottom of the machined tooth space, where there is little tensile stress before machining and a compressive stress of -15 MPa after machining. The compressive stress on the surface of the split gear blank is almost completely released during machining. The compressive stress of

material near the lower surface of gear blank increases from about -15 MPa to -8 MPa, and the tensile and compressive stress values inside the machined teeth decrease. The maximum tensile stress between the bottom of tooth space and the lower surface of the gear blank has little change before and after machining. The stress distribution of the top land cross-section and tooth space cross-section is basically the same

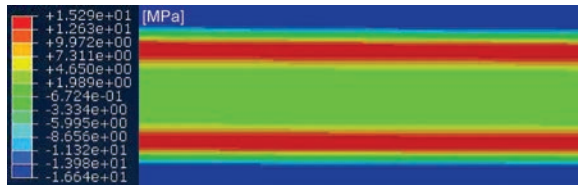


Fig. 3. X-direction stress nephogram before gear cutting

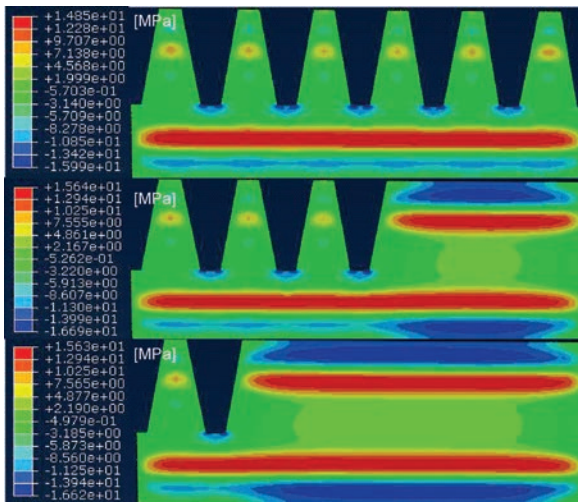


Fig. 4. X-direction stress nephogram when machining from left

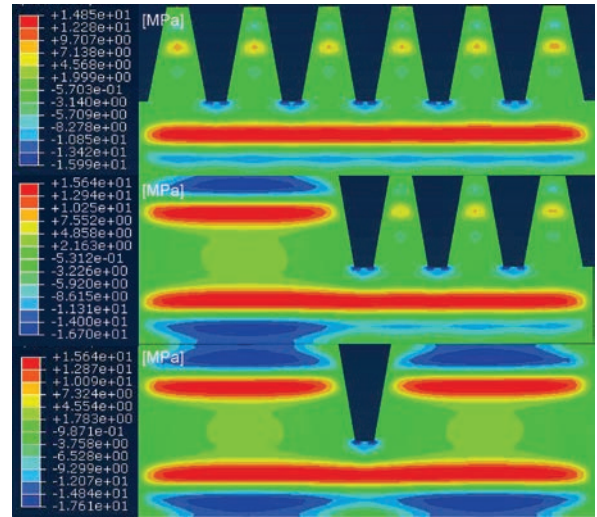


Fig. 5. X-direction stress nephogram when machining from the middle

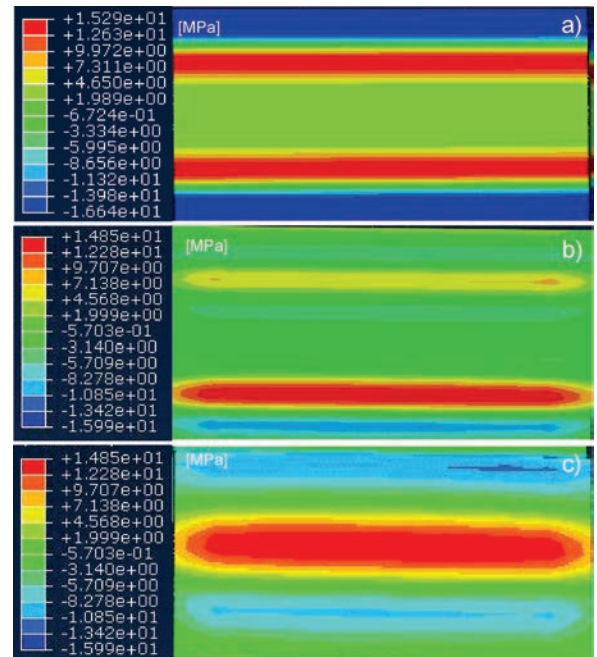


Fig. 6. X-direction stress nephogram of split gear blank along the facewidth section; a) before machining, b) of tooth topline section, and c) of tooth space section

in different cutting ways. The internal stress in the unmachined area does not change significantly during the tooth machining.

1.2.2 Stress Analysis in Y-direction

The stress analysis method in the Y-direction is similar to that in the X-direction. The finite element simulation results indicate that no matter which machining method is used, the stress change of the upper and lower surface of the gear blank is the largest, which changes from the compressive stress of -5.9 MPa before machining to the tensile stress after machining, and the maximum tensile stress can reach about 13.6 MPa, and the bottom of machined tooth space shows a large compressive stress.

In the machining process, the change of internal stress of the material near the gear cutting area is greater than that far away from the cutting area, but the change of Y-direction stress in the whole gear blank is less. It can be observed that the change of Y-direction stress is mainly reflected in the upper and lower surfaces of the gear blank.

2 DEFORMATION ANALYSIS IN GEAR CUTTING

During the gear cutting process, the material in tooth space is removed, and the stress contained in the material disappears, which is the fundamental reason for the deformation of split straight bevel gear. In this section, the deformation state of the gear blank is obtained via finite element analysis, and the deformation characteristics and law of split gear blank in gear cutting are explored. The research group’s machining practice and previous study in the split straight bevel gear indicate that the bending deformation is the main deformation and the deformation is the greatest. Therefore, this section starts with the deformation analysis in Z-direction of the split gear blank and studies the deformation law of split straight bevel gear.

2.1 Deformation Analysis in Z-direction

In two different cutting sequences, the Z-direction displacement nephogram of gear blank is shown in Fig. 7. In the case of machining from left to right, the deformation of gear blank after machining the first two tooth spaces is only 0.03mm. When the gear cutting is carried out from the middle of the gear blank, the deformation suddenly increases to 0.078 mm. When machining the middle tooth space first, the deformation is 0.048 mm. The deformation in

Z-direction reaches 0.069 mm after machining all the tooth spaces in the right half. No matter which process sequence, after machining, the gear blank is bent downward along the negative direction of Z-axis, and the maximum Z-direction displacement in the middle of the gear blank is 0.098 mm.

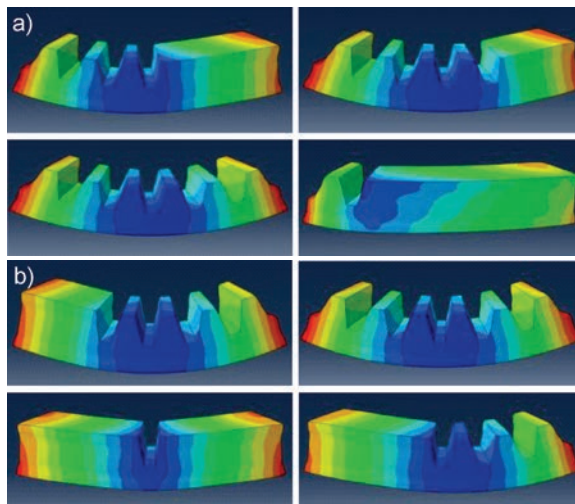


Fig. 7. Z-direction displacement nephogram in different tooth cutting sequence; a) deformation when machining from left, and b) deformation when machining from middle

Thereafter, the same machining deformation analysis was carried out for 90 mm, 85 mm, 75 mm, 70 mm thick gear blanks. The Z-direction deformation along the length direction of a gear blank is illustrated in Fig. 8.

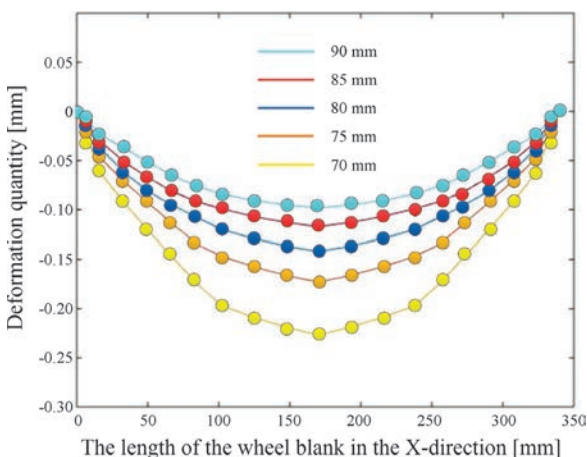


Fig. 8. Deformation in Z-direction along the length direction of gear blank with different thickness

From Fig. 8, the displacement in the Z-direction of a gear blank increases with the decrease of the thickness. The difference of the gear blank thickness

is the same, but the difference of deformation is nonlinear, and when the gear blank thickness is less than 80 mm, the speed of Z-direction deformation increases obviously.

In the subsequent machining and measurement experiment, five measuring lines are selected along the width direction on the bottom surface of the split straight bevel gear. The measuring lines are evenly distributed along the length direction. Points are taken every 3 mm on the selected measuring line, and the bottom surface coordinates are measured point by point. The comparison between the measured deformation in Z-direction and the simulation results is shown in Table 1.

Table 1. Deformation comparison in Z-direction

Deformation	Outer	33 mm from outer	33 mm from inner	Inner
Simulation [mm]	-0.142	-0.133	-0.125	-0.118
Experiment [mm]	-0.137	-0.130	-0.121	-0.115

The Z-direction deformation measured by experiment along the length direction, and the simulation results are drawn as a curve, as shown in Fig. 9.

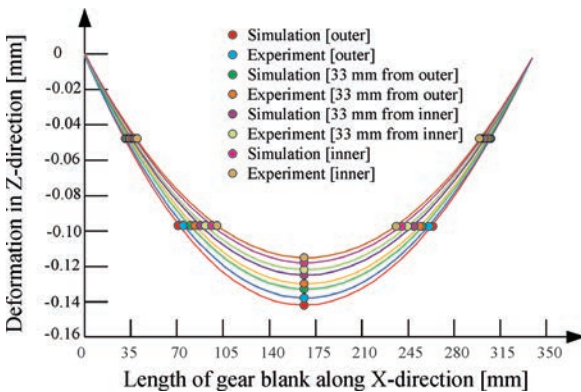


Fig. 9. Z-direction deformation at different positions along the length of gear blank

From Table 1, the deformation results obtained by finite element simulation are slightly greater than those measured in practice, and the relative errors of the two results at different positions are less than 3.6 %. From Fig. 9, it can be found that although the deformation of the gear blank decreases gradually from the wider end of a single tooth (an outer) to the narrower end of a single tooth (an inner), the deformation form remains unchanged, and the deformation in the middle of the length direction is obvious. The error between the experimental and simulation results is small, which verifies the correctness of the simulation model.

2.2 Deformation Analysis in X-direction

By analysing the displacement nephogram in the X-direction of the split straight bevel gear, it can be found that the upper surface is in a compression state, the lower surface is in a tensile state, and the deformation in X-direction is symmetrical. With the same gear blank parameters as before, the maximum absolute value of the X-direction displacement on the upper surface of finished gear blank is 0.052 mm, while that on the lower surface is 0.033 mm. The deformation process is different in different machining sequence, but the deformation mode and amount of the two methods are the same after machining. The absolute displacement in the X-direction of the upper and lower surface of the gear blank with different thickness is drawn into a broken line diagram, as illustrated in Fig. 10.

From Fig. 10, it can be observed that when the gear blank thickness decreases gradually, the displacement in the X-direction of the upper surface increases gradually, and the displacement change speed increases gradually. The X-direction displacement of the lower surface decreases with the decrease of gear blank thickness, and the displacement is obviously less than that of the upper surface. The displacement in the X-direction is less than that in the Z-direction.

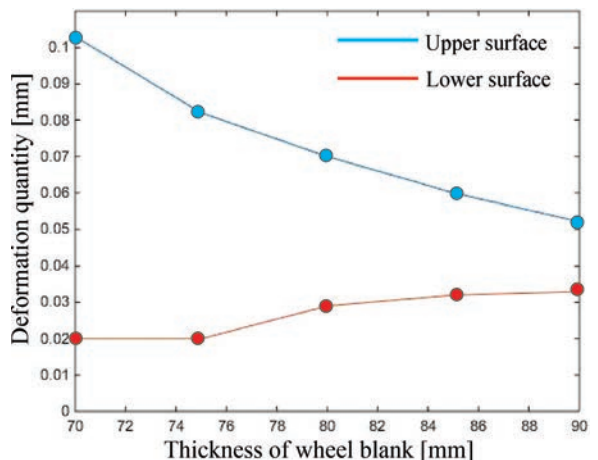


Fig. 10. X-direction deformation of upper and lower surfaces with different thickness

2.3 Deformation Analysis in Y-direction

By analysing the Y-direction displacement nephogram of split straight bevel gear, it can be found that in the two different machining processes, the displacement generally presents a negative direction along the Y-axis, and the displacement is almost zero on the

lower surface, and increases gradually from the lower surface to the upper surface. In addition, during the machining process, the machined top land indicates a large negative displacement, and the maximum negative displacement of the unprocessed area is concentrated in an outer of gear blank. With the continuous machining, the negative displacement of the gear blank along the Y-direction increases gradually. After machining, the maximum negative displacement in the Y-direction is at the tooth top of the left and right ends of gear blank, and the maximum negative displacement of upper surface is 0.029 mm.

When the only thickness of split gear blank is changed, the deformation form of the gear blank in the Y-direction will not change, but the displacement value in the Y-direction will change. The relationship between the absolute value of the maximum displacement in the Y-direction, and the gear blank thickness is drawn into a broken line diagram, as shown in Fig. 11. It can be found from Fig. 11 that with the gradual decrease of gear blank thickness, the displacement of the upper surface in the Y-direction gradually increases. In the machining process, the deformation in Y-direction is less than that in the X- and Z-directions. After machining, the deformation in the Z-direction is the largest, followed that of the X-direction.

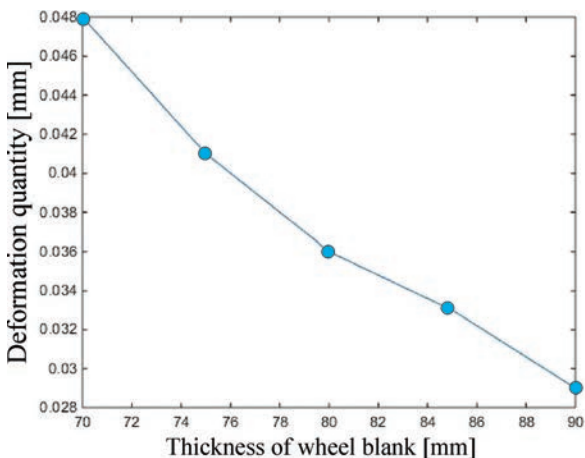


Fig. 11. Y-direction displacement of gear blank with different thickness

It is also found that the machining deformation of split straight bevel gear is not affected by the gear cutting sequence. The deformation in the Y-direction of the gear blank is slightly different in the facewidth direction, and the deformation at outer is slightly greater than that at an inner. The deformation in Y-direction is symmetrical to the middle of the length direction, the deformation of the upper surface at

the left and right ends is the most obvious, and the deformation in the middle of gear blank is little.

The subsequent experimental data indicate that the diameter of the inner and outer circle has been increasing during the machining process. The diameter of the inner and outer circle increases about 0.070 mm after the machining, that is, the deformation of gear blank along the negative direction of the Y-axis is about 0.035 mm. The experimental results are consistent with the finite element analysis.

3 EXPERIMENT

The material and size of the experimental gear blank are the same as that of the simulation model. The inner diameter of the split gear blank is 1000 mm, the outer diameter is 1200 mm, and the angle between the left and right end plane of the gear blank is 36 °.

Experimental design: firstly, the outer surface of the split gear blank is machined, and the initial measurement of the gear blank is carried out in the coordinate measuring machine. The measurement items include the flatness of the bottom surface, the verticality of the left and right end faces, the diameter of the inner and outer circle, and the angle between the left and right end faces. Thereafter, the first tooth space in the middle is machined, and the second measurement is carried out after the machining. Next, several tooth spaces on the right side are machined one at a time, and the third measurement is conducted. Finally, the left half of the split gear blank is machined, and the fourth measurement is conducted.

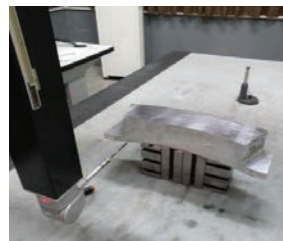


Fig. 12. First measurement



Fig. 13. Machining the 1st tooth space

Fig. 12 shows the first measurement after the split gear blank is ready. Fig. 13 shows the machining of the first tooth space, and Fig. 14 shows the second measurement after machining the first tooth space. Fig. 15 shows the machining of the remaining tooth spaces on the right side.

Fig. 16 shows the third measurement. Fig. 17 shows the machining of the remaining tooth spaces on

the left side, and Fig. 18 shows the fourth measurement. The measurement results are illustrated in Table 2.



Fig. 14. Second measurement



Fig. 15. Machining the right half tooth spaces



Fig. 16. Third measurement



Fig. 17. Machining the left half tooth spaces



Fig. 18. Fourth measurement

In the first measurement, the gear-cutting process has not been done, so the measurement data in Table 2 is sparse. However, with the continuous machining, the shape and position tolerance and inner and outer diameter of the gear blank have changed significantly.

The angle between the left and right end faces decreases continuously during the machining; the angle after machining is reduced by 0.02° compared with that before machining. It is obvious that the curvature of the gear blank is reduced, and the opening deformation occurs. After machining, the diameters of the inner and outer circle increase by about 0.07 mm. This indicates that the deformation of the gear blank is about 0.035 mm along the negative direction of the Y-axis in Fig. 7. The perpendicularity tolerance of the left and right ends of gear blank to its bottom surface has been increased slightly, and the flatness of bottom surface also continues to increase in the machining process, and the flatness tolerance is far greater than its perpendicularity tolerance.

4 CONCLUSION

The main research results and conclusions are as follows:

1. The finite element model for the deformation prediction of the split straight bevel gear is established by the birth and death element technology, and the results of finite element calculation are in good agreement with the experimental. The finite element simulation can effectively predict the machining deformation of the split straight bevel gear caused by the residual stress.
2. In the process of gear cutting, the change of initial residual stress near the upper and lower surfaces is the greatest, and the change and redistribution of stress is independent of the cutting tooth sequence. The internal stress change near the cutting area is greater than that far away from the cutting area. In an inner of the machined tooth, the tensile and compressive stress in X-direction decreases obviously, and the stress in Y-direction changes little. The performance and change of Z-direction stress in the whole machining process are relatively minor.
3. After gear cutting, the deformation of the split straight bevel gear in all directions is symmetrical about the middle of its length direction. The split

Table 2. Experimental data

Measuring order	Flatness of bottom surface [mm]	Perpendicularity of left end plane [mm]	Perpendicularity of right end plane [mm]	Outer diameter [mm]	Inner diameter [mm]	Angle between two end planes [$^\circ$]
1st	0.038	0.016	0.016	1200.001	1000.001	36.009
2nd	0.077	0.019	0.017	1200.028	1000.002	36.005
3rd	0.121	0.026	0.025	1200.049	1000.049	35.996
4th	0.161	0.031	0.028	1200.072	1000.071	35.989

gear blank mainly presents a bending deformation state, and the tooth-cutting sequence will not affect the final deformation result. In the XOZ plane, the Z-direction bending deformation in the middle of split straight bevel gear is the largest. In the XOY plane, the Z-direction deformation near an outer is larger than an inner, and the difference of deformation is especially obvious in the middle of the X-direction. The X-direction deformation of the split straight bevel gear basically does not change in the facewidth direction, and the closer to the middle of length direction, the smaller the deformation is. The deformation in Y-direction is smaller in the middle position, the deformation is slightly different in facewidth direction, and the deformation at an outer is slightly greater than that at an inner.

5 ACKNOWLEDGEMENTS

This work was supported by the National Natural Science Foundation of China (No. 51775171).

6 REFERENCES

- [1] Zhang, F.S., Xu, M.N., Zhang, B., Wang, J.S. (2017). Machining and Modification of the Large Modulus Straight Bevel Gear. *Machinery Design and Manufacture*, no. 2, p. 1-4, (in Chinese)
- [2] Qi, Z.C., Wang, X.X., Chen, W.L. (2019). A new forming method of straight bevel gear using a specific die with a flash. *The International Journal of Advanced Manufacturing Technology*, vol. 100, p. 3167-3183, DOI:10.1007/s00170-018-2862-4.
- [3] Cao, X.M., Sun, N., Deng, X.Z. (2016). Design for straight bevel gear based on low installation error sensitivity and experiment tests. *Journal of Aerospace Power*, no. 1, p. 227-232, DOI:10.13224/j.cnki.jasp.2016.01.029. (in Chinese)
- [4] Yan, P.Q., Lu, W.Z., Zhang, D., Liu, S., Pan, H.F., Zuo, D.W. (2015). Case-based reasoning method and realization of design system for large gear ring processing method. *Machine Building and Automation*, vol. 44, no. 6, p. 15-17, DOI:10.19344/j.cnki.issn1671-5276.2015.06.004. (in Chinese)
- [5] Zhang, J.Q., Zhang, Z.Y., Zhang, Y.G., Fu, Y.X. (2014). Design and application of manufacturing process of large-scale spiral bevel gear. *Manufacturing Technology and Machine Tool*, no. 5, p. 84-86, DOI:10.3969/j.issn.1005-2402.2014.05.030. (in Chinese)
- [6] Kang, Z.Z., Teng, L.X. (1998). Manufacturing technology of split large gear. *Machinery*, no. 1, p. 27-28.
- [7] Cheng, Q.L., Ke, Y.L., Dong, H.Y., Bi, Y.B.; Huang, Z.G. (2007). Distortion prediction for milling process of aerospace monolithic components. *Journal of Zhejiang University (Engineering Science)*, vol. 41, no. 5, p. 799-803, DOI:10.3785/j.issn.1008-973X.2007.05.020. (in Chinese)
- [8] Nasr, Mohamed N.A. (2017). On the role of different strain components, material plasticity, and edge effects when predicting machining-induced residual stresses using finite element modeling. *Journal of Manufacturing Science and Engineering*, vol. 139, no. 7, art. ID 071014, DOI:10.1115/1.4036122.
- [9] Amouzegar, H., Schafer, B.W., Tootkaboni, M. (2016). An incremental numerical method for calculation of residual stresses and strains in cold-formed steel members. *Thin-Walled Structures*, vol. 106, p. 61-74, DOI:10.1016/j.tws.2016.03.019.
- [10] Liu, H.W., Zhang, Z.C., Jia, H.B., Liu, Y.J., Leng, J.S. (2020). A modified composite fatigue damage model considering stiffness evolution for wind turbine blades. *Composite Structures*, vol. 233, art. ID 111736, DOI:10.1016/j.compstruct.2019.111736.
- [11] Gong, H. (2011). *Research on Evolution and Evaluation Model of Residual Stress in Aluminum Alloy Thick Plate*. PhD Thesis. Central South University: Changsha, (in Chinese)
- [12] Sun, J., Ke, Y.L. (2005). Study on machining distortion of unitization airframe due to residual stress. *Journal of Mechanical Engineering*, vol. 41, no. 2, p. 117-122, DOI:10.3901/jme.2005.02.117. (in Chinese)
- [13] Wu, H.B. (2008). *Numerical Simulation and Experimental Study on Milling Deformation of Aviation Frame Integral Structure*. PhD Thesis. Zhejiang University, Hangzhou. (in Chinese)
- [14] Lu, D. (2007). *Deformation Prediction and Fixture Layout Optimization of Aerospace Monolithic Components*. PhD Thesis. Shandong University, Jinan. (in Chinese)
- [15] Zhou, W.C. (2015). *Research on Machining Distortion of Thin-Walled Rotary Part*. MSc Thesis. Nanjing University of Aeronautics and Astronautics, Nanjing. (in Chinese)
- [16] Huang, X.M. (2015). *Deformation Mechanism and Prediction of Aluminum Alloy Monolithic Component in the Milling*. PhD Thesis. Shandong University, (in Chinese)
- [17] Nervi, S. (2005). *A mathematical model for the estimation of effects of residual stresses in aluminum parts*, PhD Thesis. Washington University. St. Louis.
- [18] Wu, Q., Li, D.P., Zhang, Y.D. (2016). Detecting milling deformation in 7075 aluminum alloy aeronautical monolithic components using the quasi-symmetric machining method. *Metals*, vol. 6, no. 4, art. ID 80, DOI:10.3390/met6040080.
- [19] Zhang, J.W., Yu, L.M., Liu, Y.C., Ma, Z.Q., Li, H.J., Liu, C.X., Wu, J.F., Ma, J.G., Li, Z.I. (2018). Analysis of the effect of tungsten inert gas welding sequences on residual stress and distortion of CFETR vacuum vessel using finite element simulations. *Metals*, vol. 8, no. 11, art. ID 912, DOI:10.3390/met8110912.
- [20] Keith, A.Y., Sebastian, N., Barna, S. (2005). *Machining-Induced Residual Stress and Distortion*. Washington University, St. Louis.
- [21] Ratchev, S., Liu, S., Huang, W., Becker, A.A. (2006). An advanced FEA based force induced error compensation strategy in milling. *International Journal of Machine Tools and Manufacture*, vol. 46, no. 5, p. 542-551, DOI:10.1016/j.ijmactools.2005.06.003.
- [22] Bremec, B., Kosel, F. (2002). Determination of the buckling loads of circular annular plates in the elastic-plastic region. *Strojniški vestnik - Journal of Mechanical Engineering*, vol. 48, no. 11, p. 613-620.

Hot Incremental Forming of Biocomposites Developed from Linen Fibres and a Thermoplastic Matrix

Sandino Torres^{1,*} – Roberto Ortega¹ – Pablo Acosta¹ – Edisson Calderón²

¹ Central Technic Higher Technological Institute (ISTCT), Industrial Mechanics & Electronics, Ecuador

² Chimborazo Higher Polytechnic School (ESPOCH), Maintenance Research GROUP (GIMAN), Ecuador

The use of biodegradable materials has a growing field of application due to environmental concerns, however, scientific research on incremental forming using biomaterials is scarce. Thus, this study focuses on the single point incremental forming (SPIF) process applied to a composite sheet that combines a biodegradable thermoplastic matrix (Solanyl) reinforced with linen fibres. The influence of the process parameters on the final geometry is determined, evaluating the effect of the following factors: step depth, wall angle and temperature reached during the process. Additionally, a heated aqueous medium is incorporated which facilitates the formability of the composite sheets. This method is especially useful for materials that have poor formability at room temperature. The benefits of using controlled heat include the reduction of forming forces applied to the plate, improved accuracy due to the reduction of elastic recovery, and the manipulation of the samples remarkably close to the glass transition temperatures. Through this experimental study with the variables analysed, a maximum shaping depth of 31 mm is obtained. These results confirm that the single point shaping used with bioplastic materials is possible and has positive outcomes for incremental forming.

Keywords: incremental forming, bio-composites, hot formability, analysis of variance, deformation

Highlights

- The factors that contribute to improve the hot incremental forming of composites with a thermoplastic matrix and their efficacy are identified.
- This article gathers the experimental results of the single point forming process in sheets of composite material (Solanyl-linen fibres).
- The main factors that influence the hot incremental forming of biodegradable composite materials are established.
- The methodology used is validated due to the small differences that exist between the different results, showing the significance of each of the factors analysed with the part depth reached during the conformation process.

0 INTRODUCTION

Material processing methods are being continuously modified due to technological development and the need to process materials faster. One method of processing materials, called incremental forming, is a technique that progressively deforms a sheet of material, using a tool operated by numerical control machines. The trajectory of the tool is generated with a computer aided manufacturing (CAM) software from a three-dimensional model that reproduces the desired geometry. Initially, the single point incremental forming (SPIF) process was applied to metallic materials for small batch production. This technique is focused on creating prototypes of materials; however, the complex methods of conventional tooling for forming processes represent a limitation due to the high investment for the manufacturing process.

Currently, there are several practical applications of incremental forming in the automotive and aeronautical sector. In Japan, for example, incremental forming is used as an alternative process to add certain features to previously stamped vehicle panels [1]. The fields of application also include the medical sector,

where several studies have been carried out for the implementation of this process in the manufacture of a femoral component of titanium-tantalum [2]. In addition, the design and manufacturing process has been analysed for using the same technique in a cranial prosthesis [3], obtaining quite encouraging results. Also, the performance of the forming process is important from the perspective of geometric precision. The manufacture of biomedical implants, through the incremental forming process, has reached deviations in the range of 1 mm to 2 mm, using the variation of the tool path as a method to improve the dimensional accuracy of the final product [4]

Recently, innovative proposals have been made to the incremental forming process, especially to improve the formability. One of the variations utilised is the application of heat, where incremental forming processes have been carried out by means of localised heating, achieving a high degree of deformation [5]. The heat-assisted incremental sheet forming (HA-ISF) has been applied to titanium alloys and high strength steel, reaching 600 °C with localized heat that comes from methods such as: laser heat, friction heat, electrical heat and induction heating [6]. In addition,

*Corr. Author's Address: Instituto Superior Tecnológico Central Técnico, Mecánica Industrial-Electrónica, El Inca, Quito, Ecuador, Itorres@istct.edu.ec

there are studies of incremental shaping applied to stainless steel dental prostheses with a plate thickness of 0.5 mm, allowing to improve the production of custom-made components [7]. The initial tests, where higher temperatures were assigned to the areas to be shaped, showed the viability of this technique [8]. There are different techniques for the application of heat, one of which is to use fluid as a heating medium to form magnesium parts. In this case, reduced forces were required for formation at elevated temperatures and improved formability was achieved [9]. It has also been determined that incremental forming with hot air is a suitable method for parts production of prostheses and orthoses, which are implemented in medical applications [10].

Moreover, the incremental forming of polymers with materials such as polyoxymethylene (POM), polytene (PE), polyamide (PA), polyvinyl chloride (PVC), polycarbonate (PC) and its manufacture of complex components has been investigated with the application of heat [11]. Studies show that with polystyrene sheets, where hot air is applied using a nozzle to raise the temperature towards the forming area, the formability is improved [9]. Temperature plays a particularly important role in the behaviour of plastic materials due to their glass transition, fluidity, morphology, and degradation characteristics. In addition, studies of incremental forming in composite materials and their preliminary viability have been carried out using glass fibre reinforced polyamide [12], which is a widely used material in the automotive sector.

Clear identification of strain conditions during the incremental forming process defines the degree of formability of a thermoplastic material. The evolution of the process shows stretching conditions and through-thickness shear deformation. Unfortunately, the physical mechanism of deformation in thermoplastics subjected to incremental shaping is not yet fully understood [13]. In the field of nanocomposites with a thermoplastic matrix, the addition of alloying materials directly influences the characteristics of the resulting composite material. PA 12 combined with 1 % to 3 % Cloisite 93A, for example, improves the mechanical strength of the composite material by 4 % to 6 % [14].

One of the other main variables of the incremental forming process is the spindle speed. However, the spindle can consume a large amount of energy. It has been said that the energy consumption will reduce if the tool does not rotate, and if the machining repetitions are decreased [15]. The spindle speed is important as it has the ability to reduce the maximum

forming forces needed and increase the formability of the sheet [16].

This study analyses the effects of various parameters (in-depth tool feed and force) on the forming behaviour of a biodegradable thermoplastic matrix (manufacture name: Solanyl), which has been combined with short linen fibres, with a length of no more than 3 mm, and linen fibres reinforcement with a concentration of 10 %. The granulated material is transformed into plates of material of 3 mm thickness and size of 180 mm × 150 mm by means of the injection process: The plasticizing unit of the injection machine is in charge of heating the material to a temperature of 150 °C and introducing it into the mold that reproduces the geometry of the plates. The plates are used in the incremental forming process, using a fluid heat source to improve its formation. Polymers reinforced with natural fibres can be used to make lightweight constructions due to their increased strength [17].

The challenge is to present the main forming parameters for prototype production. Therefore, the present study focuses mainly on the evaluation of the maximum forming depth under the influence of a heat source. For this reason, a hot environment is used through a fluid (water), at a temperature based on the obtained working range of the material. In this way, it is determined how the material behaves with the different process parameters, both constant and variables such as feed rate, tool diameter, material elasticity, temperature, spindle speed and step depth.

1 METHODS

The experimental methodology is based on simultaneous sampling of force and temperature applied to the material to analyse the deformation in a sheet of thermoplastic material of natural origin, and in a sheet of composite material, during the incremental forming process. The force [N] that the tool exerts on the material and the temperature applied to the sheet is recorded. The conical geometry formed is shown in Fig. 1; where $\varnothing D$ is the largest diameter of the cone, β is the angle of inclination, and h is the total length reached in the forming process. This is the geometry profile used for the tool trajectory, taking into account that the tool diameter will cause the formation of tracks in the corners of the model.

A spherical-tipped tool was selected, which creates a descending circular path to form the desired geometry. The forming process is carried out inside of an aqueous medium, using an electric heater to increase the water temperature; consequently, the

testing sheets are completely submerged into the fluid. The temperature is controlled through an electronic circuit that maintains the selected temperature ranges. The presence of the aqueous heating medium guarantees the heat transfer by convection in a homogeneous way towards the composite sheet. The fluid temperature is monitored by a thermocouple, and the data is collected in real time through a remote-control system. Different parameters were selected that intervene in the incremental forming process, and through this work the impacts caused by these variables and their interactions in the forming of this type of material are studied.

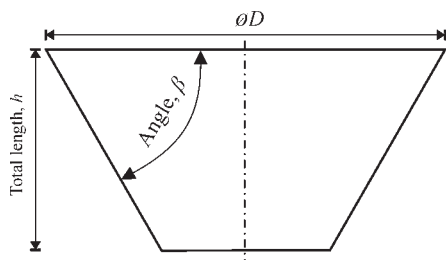


Fig. 1. Geometry profile for the incremental forming process

2 EXPERIMENTAL

This experiment aims to determine the influence of the different parameters involved in the incremental forming process, and to understand their interactive effects. These experiments focus on different forming parameters based on previous research [12] and [16]. These previous investigations show the main factors that influence the viability of the incremental forming process and provides a general criterion regarding the results. For this reason, the following parameters are evaluated: wall angle (β), step depth and temperature. For best results, the spindle is disconnected from the machine in such a way as to limit the effects of friction and avoid possible bending or twisting defects. Additionally, the maximum speed of the machine is established using a tool with a 6 mm diameter, to analyse the influence of these parameters on the total depth.

Table 1 shows a summary of the variables and parameters involved in the process.

In this study, plates injected with a starch-based thermoplastic (Solanyl C1201 from Rodenburg Biopolymers) or a composite material formed by this thermoplastic matrix with 10 % of its weight in linen fibres, were used. The linen fibre is cut with a length less than 3 mm, to improve the processing conditions of the composite material.

Table 1. Parameters involved in the incremental forming process

Parameters	Constant	
Tool diameter [mm]	6	
Feed rate [mm/min]	500	
Spindle speed (rpm)	0	
Parameters	Variables	
Step depth [mm]	0.2	0.4
Wall angle [°]	45	60
Temperature [°C]	80	90

Previously, tensile tests are carried out to analyse the mechanical behaviour of these materials [18].

The results of the mechanical properties of these materials are presented in Table 2.

Table 2. Results of the mechanical properties of the materials used

Material	Ultimate tensile strength [MPa]	Elastic modulus [-]	Percentage of deformation at break [%]
Biopolymer	10.14	2857.25	0.34
Biopolymer + 10 % linen fibre	10.16	3075.54	2.15

Through these results, the behaviour of these materials and the influence of its properties on the incremental forming process are analysed. For this reason, the elastic modulus is used as a reference to analyse its interaction with other parameters of the forming process, quantifying the improvement in formability.

The manufacturing process of this compound alternates the extrusion and injection process, as presented in [23]. The tooling and tooling design are made according to similar configurations shown in other studies of incremental shaping [3]. In this case, the main apparatus incorporates the fluid (water) at different controlled temperatures. Fig. 3 shows the apparatus used in the study.

The material used is a thermoplastic, for this reason a thermal characterization technique called differential scanning calorimetry (DSC) is carried out. DSC is a dynamic procedure that incorporates a thermo analysis technique, which determines the amount of heat that a substance absorbs or releases when it is subjected to a variation of heat flow. Thanks to this procedure, it is possible to establish at what temperature physical or chemical changes occur, including boiling points, crystallization, glass transitions, hydration effect, phase changes, curing, among others. This procedure simplifies the analysis of any type of polymer material, such as cement, ceramics, metals, pure organic matter,

pharmaceuticals, liquid crystals, biological systems, electrical and metallurgical industry [19] to [23].

Fig. 2 shows a change or energy jump that indicates a change in the properties of the material, so for example at 150 °C the curve falls into a sink that, under references of similar materials, indicates the process of fusion. But at exactly 82 °C the last decline in the graph can be seen, which suggests the glass transition temperature, the temperature necessary to be able to form the material, without losing its viscoelastic properties. This test was performed with an instrument DSC Q2000 V24.9 (origin USA) using the Sapphire method. The characterization of the material makes it possible to determine the glass transition and melting temperatures; The first is important to carry out the plastic deformation of the composite material; the second, intervenes directly in the shaping of the material. Consequently, the test is carried out to determine the thermal parameters of the polymeric material.

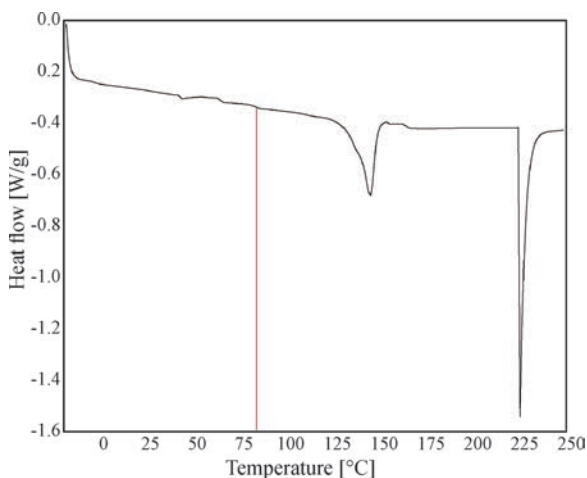


Fig. 2. DSC thermal test results for the sheet of thermoplastic, trade name Solanyl

2.1 Experimental Equipment

The tool is built using AISI 4340 alloy steel with a spherical tip and 6mm diameter shank, for the forming process; additionally, a SIEG CNC (China), milling machine is used. The machining program is carried out in the Autodesk HSM software, where toolpaths are generated, with Z-level strategy. The steps are made in the direction of the Z-axis, the information is post processed and the machining program is generated in G code, for a FANUC controller.

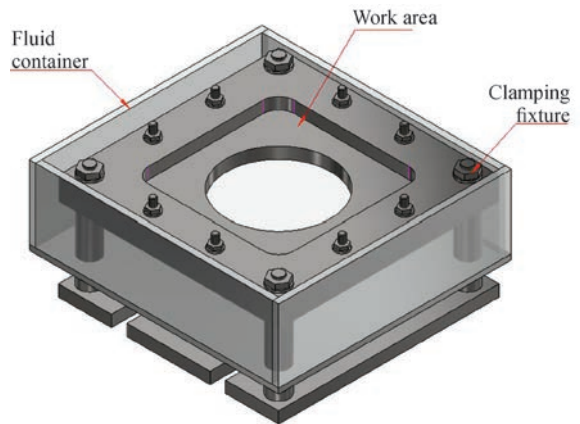


Fig. 3. Fluid container used for the hot incremental forming process

The characterization of the biodegradable materials used in this study, allowed us to understand the physical, chemical, and mechanical properties, in particular, the temperature parameters that are needed to process the material [24], where the elastic modulus is also selected as a reference in order to evaluate the results of the interaction of this parameter with the temperature, wall angle, and step down variables. In Figure 4, below, the components for the incremental forming process in biodegradable plates are shown, for which a source of heat is applied within an aqueous environment.

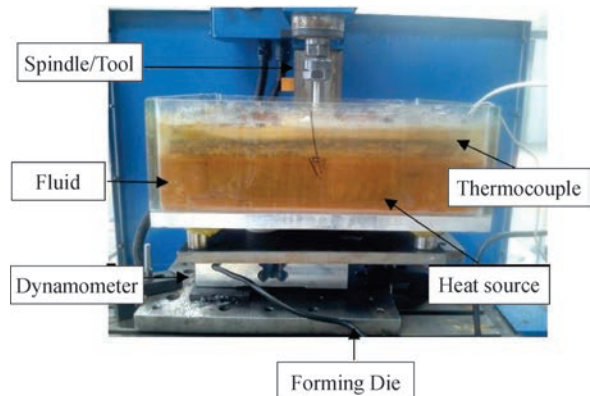


Fig. 4. Experimental configuration for hot incremental forming process

2.2 Electronic Device

To obtain and transmit data, an electronic circuit consisting of sensors, actuators and a remote-control system that displays data in real time through a user-friendly, human-machine interface has been designed and implemented. For data collection, a K type

thermocouple is placed inside the fluid area, which measures the temperature in a range of 0 °C to 800 °C, as well as a weight sensor with a capacity of 40 kN, which is responsible for recording the force generated during the process between the machine table and the forming die, which weighs the whole system, and this data is then transformed into a force value. The sensors are controlled by an electronic “Arduino Uno” card, and the programming is done in C language, using the Arduino IDE environment. Temperature and weight data are obtained by direct connection to the Arduino card; this data is sent to a local server, a Raspberry Pi 3 card programmed in Python. Fig. 5 shows the data collection diagram.

The information collected is sent via ethernet or wi-fi to a remote client, in this case a personal computer (PC), which receives the data through

a program carried out in a virtual instrumentation software: Labview, where the value of temperature is received and shown in degrees Celsius [°C] and weight is transformed into force and shown in Newtons [N]. The LabView program is used for data collection (Fig. 6).

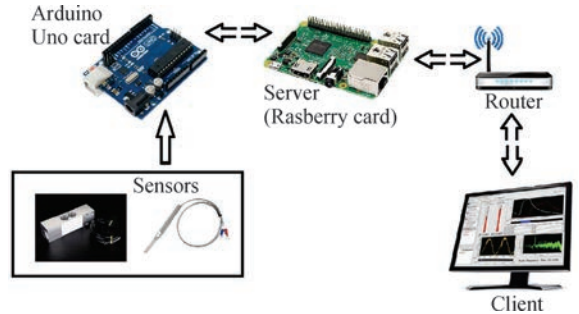


Fig. 5. Data collection diagram

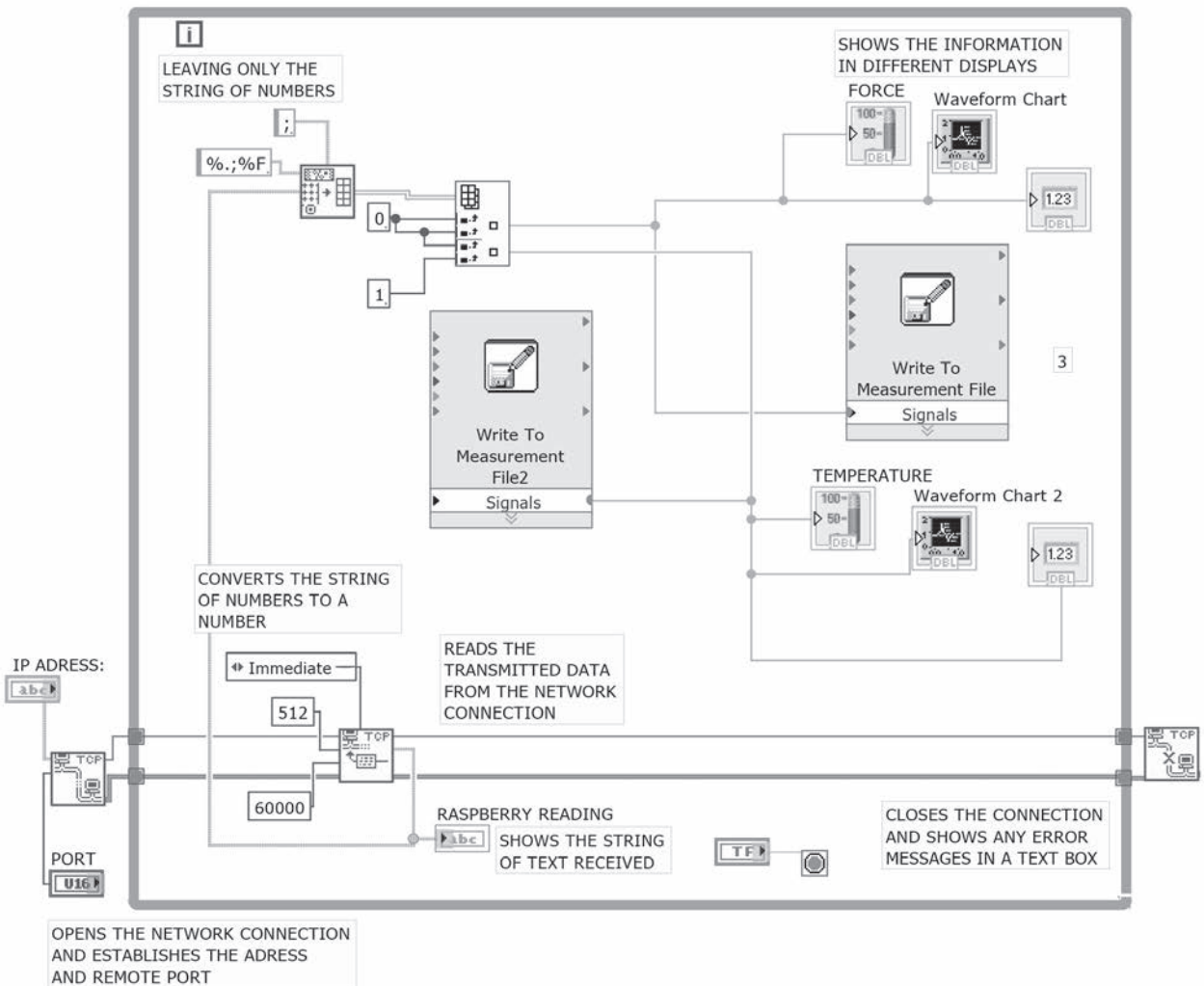


Fig. 6. Data collection diagram

3 RESULTS

The experiments are carried out to determine the most influential factors on the total part depth with the incremental forming process. For this, the parameters of step depth, wall angle and temperature of the aqueous medium are manipulated. In addition, the behaviour of the force in the incremental forming process is studied. The results obtained from the depth are taken directly from the CNC machine controller, once the material breaks. The depth value is recorded once it fails, that is, when a crack or fracture occurs in the sheet. In the event that the test meets the total depth of the proposed geometry, the length obtained is measured and that value as the maximum depth reached.

To obtain precise results, a 2⁴ factorial design with three replicas is made in Statgraphics. The results are evaluated by analysing the variance (ANOVA), which establishes the level of relationship between the variables. The response variable constitutes the total length reached after the incremental forming process. The factors for the ANOVA are presented in Table 3.

Table 3. Factors for analysis of variance

Factors	Low (-1)	High (1)	Continuous
A: Temperature	80 °C	90 °C	Yes
B: Wall angle	45 °	60 °	Yes
C: Step down	0.2 mm	0.4 mm	Yes
D: Elastic modulus	2857 MPa	3076 MPa	Yes

The purpose of carrying out the tests, shown in Table 3, is to analyse the impact caused by each of these interactions with the response variable. This procedure performs a multifactor analysis of variance for in-depth feed (pitch) of the tool. Several tests and graphs are constructed to determine which factors have a statistically significant effect on the response variable. This study also provides sufficient data to test for significant interactions between the factors. For statistical analysis, a significance level of 0.05 is used with a confidence interval of 95 %.

Table 4. Tests performed for analysis of variance

Run	A [°C]	B [°]	C [mm]	D [MPa]
1	-	-	-	+
2	-	+	-	-
3	-	-	-	-
4	+	+	+	-
5	+	-	+	-
6	+	+	-	+
7	+	-	-	-
8	+	+	+	+
9	+	-	+	+
10	-	+	+	+
11	+	-	-	-
12	-	-	+	-
13	-	+	+	-
14	+	+	-	+
15	-	-	+	+
16	-	+	-	+

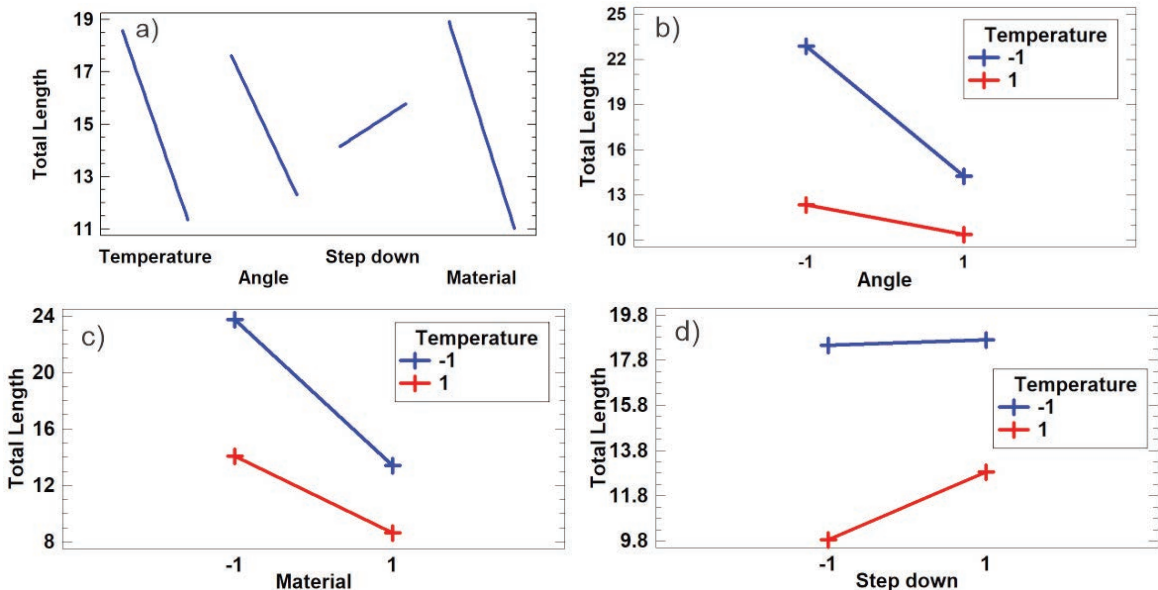


Fig. 7. Variable interaction graphics; a) main effects plot for total length, b) interaction plot for total length and angle, c) interaction plot for total length and material, d) interaction plot for total length and step down

The results of the model obtained through the ANOVA are shown in Table 4, where the level of significance of each factor is established. Fig. 7a presents the effects of the factors with respect to the response variable and their impact on the total part length. The Figs. 7b, c and d show the interaction of two factors with the experimental factor; if two factors do not interact with each other, the lines on the graph are almost parallel.

The ANOVA table (Table 5) shows the different factors such as the wall angle, temperature of the heating chamber, elastic modulus of the materials, step down, and its effect on the response variable (depth), as well as the interaction with the different factors. The *P* values prove the statistical significance of each of the factors, *P* < 0.05 values have a significant effect on the response variable (total length) with a 95 % confidence level. Table 5 also shows the value for *R*² (94.66 %), which indicates the variability related to the response variable (total length). The significant values are shown in Fig. 7, which relate all the factors. The results indicate that the use of temperatures of 80 °C (-1), angles of inclination of the geometry of 45° (-1) and the thermoplastic material in a natural state have statistical significance, demonstrating that for incremental forming processes the results are not as encouraging with the use of fragile materials.

Table 5. Data obtained through ANOVA analysis

Source	Sum of Squares	Df	Mean Square	<i>F</i> -Ratio	<i>P</i> -Value
<i>A</i>	624.963	1	624.963	195.41	0.0000
<i>B</i>	338.141	1	338.141	105.73	0.0000
<i>C</i>	31.3633	1	31.3633	9.81	0.0035
<i>D</i>	745.763	1	745.763	233.19	0.0000
<i>AB</i>	132.668	1	132.668	41.48	0.0000
<i>AC</i>	22.9633	1	22.9633	7.18	0.0112
<i>AD</i>	74.0033	1	74.0033	23.14	0.0000
<i>BC</i>	0.44083	1	0.44083	0.14	0.7127
<i>BD</i>	13.4408	1	13.4408	4.20	0.0479
<i>CD</i>	085.333	1	0.85333	0.27	0.6087
<i>T</i> error	111.935	35	3.19814	1.954	
<i>T</i> (corr.)	2097.39	47			
<i>R</i> -squared	94.6631 per	1			

It is evident that some factors are significant in the case of forming, as shown in the results. The result of this analysis shows that not all the parameters influence the final result, however, it is possible to determine how the different variables interact in order

to maximize the result, that is, to obtain the maximum depth of the sheet. Furthermore, it is shown that bidirectional interactions are also relevant within the process.

Incremental forming test with heat source in Solanyl thermoplastic material sheet, achieving 31 mm in depth, as shown in Fig. 8.

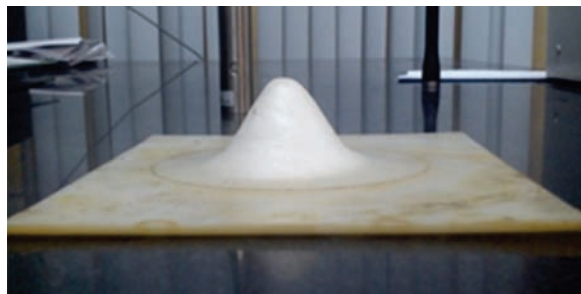


Fig. 8. Incremental forming test with heat source in Solanyl thermoplastic material sheet

The maximum step depth reached is 31 mm with a force of 35.25 N for the Solanyl material without any fibrous reinforcement. On the other hand, the lowest formability achieved is with values of total part length of 4.6 mm and with a force of 172.74 N. The combination of the parameters of wall angle (*β*), step down (*Fz*), and temperature (*T*) is described in Table 6.

Table 6. Formability parameters for unreinforced Solanyl and 10 % reinforced Solanyl

Material	<i>β</i> [°]	<i>Fz</i> [mm]	<i>T</i> [°C]
Solanyl	45	0.4	80
Solanyl (10 %)	60	0.2	90

The individual effects of the temperature, wall angle, step depth and elastic modulus factors on each material in the case of the maximum forming depth do not result in a significant effect on the response variable. However, the effect on the depth of each cited factor can be differentiated. Fig. 9 shows the contribution of each of the factors with the predominance of temperature for shaping the material as proposed in this work.

High strength sheet metal materials can barely be formed by conventional single-point incremental forming process [25]. The formed pieces produced using this process, exhibit diminished geometric precision and low forming values; thus, the application of temperature is convenient.

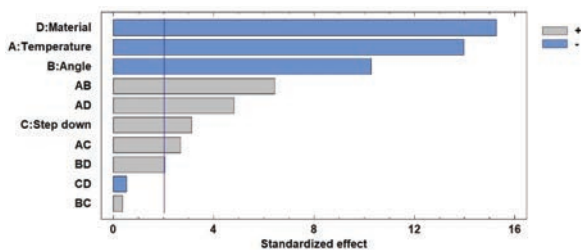


Fig. 9. Pareto diagram for contributing factors in the case of depth

In the same way, in polymer forming it has been shown that the increase in temperature will improve ductility [26], which contributes to the forming of thermoplastic materials. In this study, a homogeneous temperature was applied on the biodegradable material plate, obtaining a uniform distribution of stress and heat in the process. Unlike cold plastic deformation [9], with controlled temperatures, bio-polymeric plates can result in large deformations when analysing the displaced depth.

4 DISCUSSION

The results show that the thermoplastic matrix in its original state has the largest formability, because the material reaches a greater step depth compared to the composite sheet. The depth achieved in the composite material is fully congruent with the formability expected in less ductile materials (higher elastic modulus); this, without limiting the factors analysed that have statistical significance.

The results presented are summarized to provide an overview of the interaction between the different process parameters and their variables. This information presents an initial model for the forming of composite materials with a thermoplastic matrix. The results highlight factors that contribute to the forming of these types of materials and their efficacy are identified, as in the case of the forming force. Shown in Fig. 10, the forces obtained in the incremental forming process using the parameters that reach maximum forming depth, and the factors with minimum forming depth are shown in Tables 5 and 6 respectively. It is remarkable that a small increase in the temperature value of the sheet can cause some modifications in the molecular structure of the polymer. In the case of the thermoplastic matrix (Solanyl), the temperature of the glass transition shown in the DSC tests is 82 °C, when this value increases, the results of the forming decrease. The temperatures applied (80 °C, 90 °C) during the tests take the glass transition temperature as a reference and were reached after an iterative process with the

variables involved not affecting the integrity of the biomaterial and composite material plates.

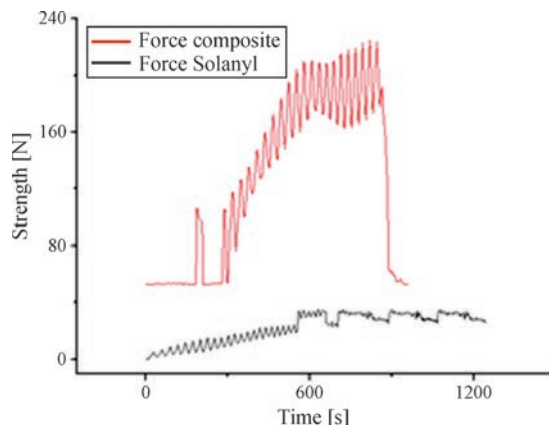


Fig. 10. Relation of forces for parameters of the maximum and minimum formability

This study shows that the improvement of the forming in thermoplastic sheets depends on the variation of certain parameters such as temperature, the angle of inclination of the geometry, and the elastic modulus of the material to be shaped.

5 CONCLUSIONS

This article gathers the experimental results of the single point forming process in sheets of Solanyl and composite material (Solanyl-linen fibres). According to the multifactor analysis of the variance, it is observed that the temperature of the aqueous medium has a significant effect on the forming process of sheets of the composite material with greater depths achieved at a temperature of 80 °C.

Additionally, the elastic modulus directly influences the deformation of the composite material, and therefore it is necessary to use less fragile and more ductile composite materials. The main factors that influence the forming of biodegradable composite materials are established, for which it would be important to develop a composite material with better forming properties, since this technique could achieve good results in the manufacture of products with these materials.

The methodology used is validated due to the small differences that exist between the different results, showing the significance of each of the factors analysed with the depth reached during the conformation process. The heating method used (plates in an aqueous medium) guarantees uniform temperature distribution throughout the thickness of

the plate; however, future research must be carried out to determine the impact of hygroscopicity on polymer properties during immersion.

6 ACKNOWLEDGEMENTS

This study has been developed with the grant and subsidy of the project called: “Combined process of incremental forming and injection molding in sheets of biodegradable thermoplastic material”, where the following academic and administrative public institutions from Ecuador are involved: “Secretaría de Educación Superior, Ciencia, Tecnología e Innovación” (SENESCYT), “Instituto Tecnológico Superior Central Técnico (ISTCT)” and “Escuela Politécnica Nacional (EPN)”.

7 REFERENCES

- [1] Amino, M., Mizoguchi, M., Terauchi, Y., Maki, T. (2014). Current status of ‘Dieless’ Amino’s incremental forming. *Procedia Engineering*, vol. 81, p. 54-62, DOI:10.1016/j.proeng.2014.09.128.
- [2] Bhojar, P.K., Borade, A.B. (2015). The use of single point incremental forming for customized implants of unicondylar knee arthroplasty: A review. *Research on Biomedical Engineering*, vol. 31, no. 4, p. 352-357, DOI:10.1590/2446-4740.0705.
- [3] Centeno, G., Morales-Palma, D., Gonzalez-Perez-Somarrriba, B., Bagudanch, I., Egea-Guerrero, J.J., Gonzalez-Perez, L.M., García-Romeu, M-L., Vallengano, C. (2017). A functional methodology on the manufacturing of customized polymeric cranial prostheses from CAT using SPIF. *Rapid Prototyping Journal*, vol. 23, no. 4, p. 771-780, DOI:10.1108/RPJ-02-2016-0031.
- [4] Cheng, Z., Li, Y., Xu, C., Liu, Y., Ghafoor, S., Li, F. (2020). Incremental sheet forming towards biomedical implants: a review. *Journal of Materials Research and Technology*, vol. 9, no. 4, p. 7225-7251, DOI:10.1016/j.jmrt.2020.04.096.
- [5] Al-Obaidi, A., Kräusel, V., Landgrebe, D. (2016). Hot single-point incremental forming assisted by induction heating. *The International Journal of Advanced Manufacturing Technology*, vol. 82, no. 5-8, p. 1163-1171, DOI:10.1007/s00170-015-7439-x.
- [6] Liu, Z. (2018). Heat-assisted incremental sheet forming: a state-of-the-art review. *The International Journal of Advanced Manufacturing Technology*, vol. 98, no. 9-12, p. 2987-3003, DOI:10.1007/s00170-018-2470-3.
- [7] Milutinović, M., Lendjel, R., Baloš, S., Zlatanović, D.L., Sevršek, L., Pepelnjak, T. (2021). Characterisation of geometrical and physical properties of a stainless steel denture framework manufactured by single-point incremental forming. *Journal of Materials Research and Technology*, vol. 10, p. 605-623, DOI:10.1016/j.jmrt.2020.12.014.
- [8] Gagliardi, F., Ambrogio, G., Filice, L. (2017). Incremental forming with local induction heating on materials with magnetic and non-magnetic properties. *Procedia Engineering*, vol. 183, p. 143-148, DOI:10.1016/j.proeng.2017.04.037.
- [9] Al-Obaidi, A., Graf, A., Kräusel, V., Trautmann, M. (2019). Heat supported single point incremental forming of hybrid laminates for orthopedic applications. *Procedia Manufacturing*, vol. 29, p. 21-27, DOI:10.1016/j.promfg.2019.02.101.
- [10] Galdos, L., De Argandoña, E.S., Ulacia, I., Arruebarrena, G. (2012). Warm incremental forming of magnesium alloys using hot fluid as heating media. *Key Engineering Materials*, vol. 504-506, p. 815-820, DOI:10.4028/www.scientific.net/KEM.504-506.815.
- [11] Centeno, G., Silva, M.B., Cristino, V.A.M., Vallengano, C., Martins, P.A.F. (2012). Hole-flanging by incremental sheet forming. *International Journal of Machine Tools and Manufacture*, vol. 59, p. 46-54, DOI:10.1016/j.ijmactools.2012.03.007.
- [12] Conte, R., Ambrogio, G., Pulice, D., Gagliardi, F., Filice, L. Incremental Sheet forming of a composite made of thermoplastic matrix and glass-fiber reinforcement. *Procedia Engineering*, vol. 207, p. 819-824, DOI:10.1016/j.proeng.2017.10.835.
- [13] Zhu, H., Ou, H., Popov, (2020). Incremental sheet forming of thermoplastics: a review. *The International Journal of Advanced Manufacturing Technology*, p. 565-587, DOI:10.1007/s00170-020-06056-5.
- [14] Borić, A., Kalendová, A., Urbanek, M., Pepelnjak, T. (2019). Characterisation of polyamide (PA) 12 nanocomposites with montmorillonite (MMT) filler clay used for the incremental forming of sheets. *Polymers*, vol. 11, no. 8, art. ID 1248, DOI:10.3390/polym11081248.
- [15] Bagudanch, I., Garcia-Romeu, M.L., Sabater, M. (2016). Incremental forming of polymers: Process parameters selection from the perspective of electric energy consumption and cost. *Journal of Cleaner Production*, vol. 112, p. 1013-1024, DOI:10.1016/j.jclepro.2015.08.087.
- [16] Bagudanch, I., Garcia-Romeu, M.L., Centeno, G., Elías-Zúñiga, A., Ciurana, J. (2015). Forming force and temperature effects on single point incremental forming of polyvinylchloride. *Journal of Materials Processing Technology*, vol. 219, p. 221-229, DOI:10.1016/j.jmatprotec.2014.12.004.
- [17] Sanal, I., Verma, D. (2019). Construction materials reinforced with natural products. *Handbook of Ecomaterials*, vol. 3, p. 2119-2142, DOI:10.1007/978-3-319-68255-6_75.
- [18] Calderón Freire, E.F., TorresGallegos, L., Ortega Espín, A. (2019). Manufacture of biodegradable material based on thermoplastic polymers combined with short flax fibers. *FIGEMPA Research And Development*, vol. 1, no. 1, p. 32-38, DOI:10.29166/revfig.v1i1.1402. (in Spanish)
- [19] Venegas Vásconez, D. (2017). Calorimetria diferencial de barrido, *Termodinámica*, University of the Bío Bío, Concepción, p. 1-6, DOI:10.13140/RG.2.2.12849.79204. (in Spanish)
- [20] Romero Carrión, V., Tirado Rengifo, A., Dávalos Prado, J. (2015). Experimental determination using DSC of the thermal stabilities and the calorific capacities: quinoa, kiwicha and cañihua. *Cátedra Villarreal*, vol. 1, no. 2, p. 47-52, DOI:10.24039/cv20153144. (in Spanish)
- [21] Granados Cristancho, Y.A. (2015). Proyecto presentado como prerrequisito para optar al título de Ingeniero Topográfico /

Project presented as a prerequisite to qualify for the title of Topographic Engineer.

- [22] Ma, S., Yu, J.Y. (2017). Transition-based versus state-based reward functions for MDPs with Value-At-Risk. *55th Annual Allerton Conference on Communication, Control, and Computing*, p. 974-981, DOI:10.1109/ALLERTON.2017.8262843.
- [23] Xie, X.Q., Moring, J., Makriyanni, A. (1997). Differential scanning calorimetry and small angle X-ray diffraction study of the interaction of (R)-PAF, (R)-ET-18-OMe and (R)-Lyso-PAF with model membranes. *Life Sciences*, vol. 61, no. 9, p. 909-923, DOI:10.1016/S0024-3205(97)00593-6.
- [24] Torres Gallegos, L. (2019). *Characterization of biodegradable materials for incremental forming*. *5th International Congress of Science, Technology and Innovation for Society*, p. 290-299.
- [25] Silva, M.B., Skjoedt, M., Martins, P.A.F., Bay, N. (2014). *Single Point incremental forming of metal sheets*. *Annual Winter Meeting of Danish Society for Metallurgy*, p. MBS1-MBS14.
- [26] Hughes, S.E. (2009). *Materials and Their Weldability. A Quick Guide to Welding and Weld Inspection*, ASME Press, p. 36-48, DOI:<https://doi.org/10.1115/1.859506.ch4>.

Vsebina

Strojniški vestnik - Journal of Mechanical Engineering
letnik 67(2021 , številka 3
Ljubljana, marec 2021
ISSN 0039-2480

Izhaja mesečno

Razširjeni povzetki (extended abstracts)

- Yong Wang, Xiaolin Wang, Zilong Zhang, Yu Li, Houlin Liu, Xiang Zhang, Marko Hočevar: Optimizacija samozbujenega curka zrak-voda na osnovi metode odzivnih ploskev SI 13
- Manuel Javier Rosel Solis, José Omar Dávalos Ramírez, Javier Molina Salazar, Juan Antonio Ruiz Ochoa, Antonio Gómez Roa: Optimizacija listnate tekaške proteze z vraninim iskalnim algoritmom in podporo umetne nevrnske mreže SI 14
- Omar Dávalos, Uzziel Caldiño-Herrera, Delfino Cornejo-Monroy, Oscar Tenango-Pirin, Juan Carlos García, M.A. Basurto-Pensado: Zmanjšanje mase in napetosti v gumijastem nosilcu motorja pod vplivom mehanskih vibracij SI 15
- Bin Wang, Chenxiao Yan, Jubo Li, Peiyao Feng, ShuaiPu Wang, Shuo Chen, Jianxin Su: Analiza preostalih napetosti in deformacije po obdelavi segmenta stožčastega zobnika z ravnimi zobmi SI 16
- Sandino Torres, Roberto Ortega, Pablo Acosta, Edisson Calderón: Vroče inkrementalno preoblikovanje biokompozitov iz lanenih vlaken in termoplastične matrice SI 17

Optimizacija samozbujenega curka zrak-voda na osnovi metode odzivnih ploskev

Yong Wang¹ – Xiaolin Wang¹ – Zilong Zhang¹ – Yu Li¹ – Houlin Liu^{1,*} – Xiang Zhang² – Marko Hočevar³

¹Jiangsu univerza, Raziskovalni center za strojništvo, tekočinske stroje in tehnologijo, Kitajska

²Univerza Xihua, Ključni laboratorij za tekočinske in pogonske stroje, Kitajska

³University of Ljubljana, Faculty of Mechanical Engineering, Slovenija

Uporaba samozbujenega curka zrak-voda za čiščenje površin ima številne prednosti pred kontinuirnim curkom, zato se pojavlja v številnih praktičnih in industrijskih aplikacijah. Samozbujeni curek zrak-voda je novost, ki združuje prednosti različnih vrst curkov. Njegova najpomembnejša značilnost je namesto kontinuirne kvazi-periodično dovajanje mase vode na čiščeno površino. Periodičen dvofazni tok samozbujenega curka zrak-voda nastane v nihajni komori zaradi pojava mejne in strižne plasti, sesanja zraka iz lukenj v steni komore, oblikovanje turbulentnih vrtincev dvofaznega toka zraka in vode ter trganja zračnih mehurčkov in mešanja zraka z glavnim tokom. Občasni in kvazi-periodični udar samozbujenega curka zrak-voda temeljiteje odstrani madeže na čiščeni površini. Njegova prostorska porazdelitev je široka in enakomerna, kar bistveno izboljša čistilni učinek.

Da bi bolje razumeli postopek delovanja samozbujenega vodnega curka, smo izvedli postopek eksperimentalne analize in statističnega modeliranja z metodo odzivnih ploskev. S tem smo optimirali delovanje samozbujenega curka zrak-voda preko parametrov dolžine nihajne komore, višine nihajne komore in premera šobe ter modelirali spremenljivki povprečno udarno silo in fluktuacijo udarne sile.

Metodologija dela je vsebovala načrtovanje in izdelavo merilne postaje, izvedbo meritev v izbranih delovnih točkah, vrednotenje rezultatov in eksperimentalno modeliranje z metodo odzivnih ploskev. Glavni deli merilne postaje so oskrba in priprava vode, šoba, sistem za vrednotenje čiščenja, merjenje sile, vizualizacija toka s hitro kamero in nadzorni sistemi. Učinkovitost čiščenja smo vrednotili z razmerjem očiščene površine. Slike preostale umazanije smo posneli periodično vsakih 10 s. Razmerje očiščene površine je bilo izračunano iz posnetih slik s pomočjo programske opreme za analizo slik s pomočjo predhodne obdelave, sivenja, segmentacije slik, kalibracije in izračuna površine. Eksperiment je bil izveden v 17 delovnih točkah. Metoda odzivnih ploskev omogoča vrednotenje spremembe posameznega vhodnega parametra na izbrani izhodni parameter, kar določa povezavo med vodnimi in izhodnimi spremenljivkami. V prispevku je bila uporabljena Box-Behnkenova metoda drugega reda. Izvedena je bila analiza variance, ki je ena od tehnik podatkovnega rudarjenja. Da bi ocenili učinek posamezne spremenljivke, smo celotno varianco modela razstavili na prispevek vsake spremenljivke in na njihove interakcije. Ta metoda se uporablja za prepoznavanje nepotrebnih izrazov v funkciji modela.

Model odzivnih ploskev in analiza variance sta za povprečno udarno silo sta pokazali, da imata vstopni premer šobe (A) in dolžina komore (B) kot dva posamezna dejavnika zelo pomemben vpliv na velikost povprečne udarne sile. Vrstni red vpliva posameznih dejavnikov na povprečno udarno silo je dolžina komore (B) > vstopni premer spodnje šobe (A) > višina komore (C). Vrstni red vpliva interakcije posameznih spremenljivk na povprečno udarno silo je višina dolvodne šobe in komore (AC) > dolžina komore in višina komore (BC) > dolžina dolvodne šobe in komore (AB). Podane so optimirane vrednosti za optimizacijske parametre in za izhodne spremenljivke.

Izvedena je bila vizualizacija curka. Zaradi nestabilnosti toka v curku in površinske napetosti vode, se v curku izoblikujejo zgoščenine, ki sčasoma povzročijo nastanek kapljic različnih velikosti. Rezultati kažejo, da z optimizacijo samozbujenega curka zrak-voda kapljice nastanejo mnogo bližje šobi, to je že na razdalji 12 cm stran od šobe.

Postopek statističnega modeliranja z metodo odzivnih ploskev je bil uporabljen za modeliranje nastanka samozbujenega curka zrak-voda za čiščenje površin. Rezultat modeliranja je množica parametrov za spremenljivke procesa in sicer premer šobe, dolžina komore in višina komore. Na ta način se je izboljšalo čiščenje in sicer se je očiščena površina po 50 s delovanja povečala za 22 %.

Čeprav je bila večparametrična optimizacija samozbujenega curka zrak-voda uspešna, je bilo v model vključenih omejeno število ključnih optimizacijskih parametrov. V prihodnosti bo mogoče izvesti večparametrsko optimizacijo za dodatne spremenljivke kot so velikost odprtin in kot nagiba vstopa in izstopa iz mešalne komore, ter velikost odprtine šobe.

Ključne besede: večfazni tok, udarna sila, curek, učinek čiščenja, optimizacija, metoda odzivnih ploskev

Optimizacija listnate tekaške proteze z vraninim iskalnim algoritmom in podporo umetne nevronske mreže

Manuel Javier Rosel Solis¹ – José Omar Dávalos Ramírez^{2,*} – Javier Molina Salazar² –
Juan Antonio Ruiz Ochoa¹ – Antonio Gómez Roa¹

¹Avtonomna univerza Baja California, Mehika

²Avtonomna univerza Ciudad Juárez, Mehika

V članku je predstavljena metodologija za konstruiranje listnatih tekaških protez za ljudi, ki so izgubili spodnje ude. Proteze jim bodo pomagale, da se bodo lahko ponovno lotili rekreativnih dejavnosti, kot je tek. Izdelana je bila listnata tekaška proteza z jedrom iz akrilonitril butadien stirena in več plasti epoksi smole z ogljikovimi vlakni.

Razvit je bil postopek za optimizacijo, ki uporablja vranin iskalni algoritem. V podporo postopku so bile vključene umetne nevronske mreže, ki znatno skrajšajo računski čas. Za učenje umetne nevronske mreže so bili uporabljeni izračuni po metodi končnih elementov.

Cilj optimizacije je bil povečanje pomika proteze med procesom hoje. Pomik je omejen z mehanskim odporom proteze, ki je bil ocenjen s kriterijem porušitve Tsai-Wu za kompozitne materiale. Analizirane so bile tri različne usmeritve plasti ogljikovih vlaken ($-45^\circ/45^\circ$, $0^\circ/90^\circ$) in primer z mešano usmeritvijo plasti vlaken. Za določitev relativnega pomena konstrukcijskih spremenljivk je bila uporabljena Garsonova enačba. Ta enačba uporablja koeficiente umetne nevronske mreže.

Rezultati optimizacije so pokazali, da ima proteza z usmeritvijo vlaken $0/90^\circ$ najboljše razmerje med pomikom (9,19 mm) in varnostnim faktorjem (1,34) med vsemi tremi različicami. Usmeritev $-45/45^\circ$ sicer daje večje pomike, ker pa je varnostni faktor manjši od 1, pri njej pride do porušitve. Pri mešani orientaciji plasti vlaken je pomik samo 5 mm, varnostni faktor pa znaša 1,45. Škoda na protezi je koncentrirana v območju stika s podlago. Največji vpliv med konstrukcijskimi parametri imata število plasti in širina proteze.

V prihodnje bo mogoče izdelati fizično protezo in jo preizkusiti. Ostaja tudi raziskava možnosti optimizacije z enosmernimi vlakni v primerjavi z usmeritvijo plasti $0/90^\circ$. Naslednja možnost za analizo pomikov je povečanje širine proteze.

V članku je opisana metoda za hitro in preprosto konstruiranje listnate tekaške proteze, ki bo uporabna za izdelavo ortopedskih pripomočkov po meri. Izdelava proteze je poceni in nezahtevna.

Ključne besede: optimizacija, vranin iskalni algoritem, umetne nevronske mreže, tekaške listnate proteze, kriterij Tsai-Wu, metoda končnih elementov

Zmanjšanje mase in napetosti v gumijastem nosilcu motorja pod vplivom mehanskih vibracij

Omar Dávalos¹ – Uzziel Caldiño-Herrera¹ – Delfino Cornejo-Monroy¹ –
Oscar Tenango-Pirin¹ – Juan Carlos García^{2,*} – M.A. Basurto-Pensado²

¹ Autonomna univerza Ciudad Juárez, Mehika

² Autonomna univerza Estado de Morelos, Mehika

V članku je predstavljena metodologija za zmanjšanje napetosti, pomikov in mase gumijastega nosilca motorja, izpostavljenega mehanskim vibracijam. Cilj je podaljšanje njegove življenjske dobe in zmanjšanje prenosa vibracij na šasijo za udobnejšo vožnjo.

Za optimizacijo mase, napetosti in pomikov nosilca motorja pod vplivom mehanskih vibracij je bil uporabljen optimizacijski algoritem GODLIKE. Na podlagi izračuna odziva napetosti in pomikov v določenem frekvenčnem območju po metodi končnih elementov je bila izdelana baza podatkov. Ta je bila nato uporabljena za učenje umetne nevronske mreže, s katero je bila optimizirana ciljna funkcija.

Frekvenčno območje, znotraj katerega deluje motor, je bilo določeno z eksperimentalnimi meritvami. Odziv napetosti in pomika nad tem območjem je bil določen s frekvenčnim korakom 1 Hz. Podan je predlog tehnike za določitev povprečja frekvenčnega odziva v tem območju. V postopku optimizacije je bilo to povprečje za skrajšanje računskega časa napovedano z umetnimi nevronskimi mrežami. Umetna nevronska mreža je bila ocenjena z determinacijskim koeficientom in s korenem povprečne kvadratne napake. Uporabljena je bila večciljna optimizacija. Numerični model je bil validiran z meritvami lastne frekvence nosilca motorja.

Rezultati kažejo zmanjšanje mase za 15,3 %, pomik pa se je zmanjšal za 12,46 %. Največje zmanjšanje je bilo ugotovljeno pri napetostnem odzivu, in sicer za 21,5 % v primerjavi z izhodiščno konstrukcijo. Tudi ob razširitvi delovnega območja je bil ugotovljen konstanten trend nižanja odzivov oz. njihove amplitude. Nevronska mreža je lahko učinkovito napovedala odzive in maso. Primerjava je pokazala dobro ujemanje numeričnih in eksperimentalnih rezultatov.

Numerični model je bil validiran pred optimizacijo, preostaja pa še eksperimentalna potrditev končnih rezultatov.

V članku je predstavljena metoda za konstruiranje nosilca motorja z gumijastim jedrom. Metoda omogoča izboljšanje udobja za potnike, podaljšanje življenjske dobe komponent in znižanje proizvodnih stroškov zaradi zmanjšanja mase.

Ključne besede: večciljna optimizacija, nosilec motorja, umetna nevronska mreža, MKE, določitev globalnega optimuma, vibracije

Analiza preostalih napetosti in deformacije po obdelavi segmenta stožčastega zobnika z ravnimi zobmi

Bin Wang^{1,2} – Chenxiao Yan^{1,*} – Jubo Li¹ – Peiyao Feng³ – Shuairu Wang¹ – Shuo Chen¹ – Jianxin Su¹

¹Šola za mehatroniko, Znanstveno-tehniška univerza v Henanu, Kitajska

²Sodelovalno inovacijsko središče za napredno proizvodnjo strojne opreme, Kitajska

³Xinxiang letalska industrija, Kitajska

Med obdelavo segmenta stožčastega zobnika z ravnimi zobmi se spremeni togost in se prerazporedijo notranje napetosti, posledično pa pride do velike deformacije zobnika. Razvit je bil ustrezen model s pretvorbo informacij o obdelavi surovca v informacije za simulacijo s končnimi elementi. Nato je bila opravljena simulacija obdelave segmenta stožčastega zobnika z ravnimi zobmi. Ob upoštevanju materiala, konstrukcije in procesa obdelave surovca so bile preučene lastnosti in zakonitosti sprememb notranjih napetosti med obdelavo zobnika. Preučeni so bili notranji mehanizmi in deformacija zobniškega segmenta. Končno so bile opravljene še eksperimentalna obdelava in meritve zobnika. Rezultati kažejo, da se zakon deformacije iz simulacij ujema s tistim, določenim eksperimentalno. Lastnosti deformacije segmenta stožčastega zobnika z ravnimi zobmi so skladne z zakonom spremembe začetnih preostalih napetosti.

Simulacija po metodi končnih elementov omogoča učinkovito napovedovanje deformacije segmenta stožčastega zobnika z ravnimi zobmi po obdelavi zaradi preostalih napetosti. Sprememba začetnih preostalih napetosti je največja v bližini zgornje in spodnje površine, sprememba in prerazporeditev napetosti pa nista odvisni od zaporedja rezanja zob. Sprememba notranjih napetosti v bližini območja odrezavanja je večja kot daleč od njega. V notranjosti obdelanega zoba pride do znatnega zmanjšanja nateznih in tlačnih napetosti v smeri X, medtem ko je sprememba v smeri Y majhna. Sprememba napetosti v smeri Z med celotnim procesom obdelave ostane majhna. Deformacija segmenta stožčastega zobnika z ravnimi zobmi po obdelavi je v vseh smereh simetrična glede na središče po dolžini. V surovcu zobniškega segmenta je prisotno predvsem upogibno deformacijsko stanje, zaporedje rezanja zob pa ne vpliva na končno deformacijo. V ravnini XOZ je upogibna deformacija Z največja na sredini zobniškega segmenta. V ravnini XOY je deformacija v smeri Z na zunanji strani večja kot na notranji strani, razlika deformacij pa je še posebej očitna na sredini v smeri X. Deformacija segmenta stožčastega zobnika v smeri X se ne spreminja po širini. Deformacija se po dolžini zmanjšuje proti sredini. Deformacija v smeri Y je manjša na sredini in nekoliko odstopa po širini. Deformacija na zunanji strani je nekoliko večja kot na notranji strani.

Rezultati raziskave so bili uporabljeni pri obdelavi velikega segmenta stožčastega zobnika z ravnimi zobmi. Ker pa deformacije surovca ni mogoče točno napovedati, bo to predmet prihodnjih raziskav. Raziskava podaja teoretično osnovo za napovedovanje deformacije po obdelavi velikih stožčastih zobnikov z ravnimi zobmi ter postavlja temelje za njeno obvladovanje. Na ta način bo mogoče doseči izboljšanje natančnosti obdelave velikih segmentov stožčastih zobnikov z ravnimi zobmi.

Ključne besede: segment stožčastega zobnika z ravnimi zobmi, preostale napetosti, deformacija po obdelavi, model s končnimi elementi, simulacija obdelave, meritve deformacije

Vročje inkrementalno preoblikovanje biokompozitov iz lanenih vlaken in termoplastične matrice

Sandino Torres^{1,*} – Roberto Ortega¹ – Pablo Acosta¹ – Edison Calderón²

¹ Osrednji tehnični inštitut, Industrijsko strojništvo in elektrotehnika, Ekvador

⁴ Chimborazo višja politehnična šola, Raziskovalna skupina za vzdrževanje, Ekvador

Uporaba biorazgradljivih materialov je v porastu zaradi okoljskih vidikov, toda znanstvenih raziskav procesa inkrementalnega preoblikovanja biomaterialov do sedaj ni bilo veliko. Pričujoča študija zato obravnava proces točkovnega inkrementalnega preoblikovanja (SPIF) kompozitne folije iz biorazgradljive termoplastične matrice (Solanyl), ojačene z lanenimi vlakni. Trajektorija orodja je bila pripravljena s programsko opremo za računalniško podprto proizvodnjo (CAM) na osnovi tridimenzionalnega modela, ki reproducira želeno geometrijo. Geometrijska natančnost preoblikovalnega procesa je pomembna za aplikacije v medicini, kot so biomedicinski vsadki. Pri tem obstaja tudi možnost uporabe ogrevanega medija na vodni osnovi, ki izboljšuje preoblikovalnost kompozitne folije. Metoda je še posebej uporabna za materiale, ki se slabo preoblikujejo pri sobni temperaturi. Med prednostmi nadzorovanega ogrevanja so zmanjšanje preoblikovalnih sil, ki delujejo na ploščo, izboljšanje natančnosti zaradi zmanjšanja elastične histereze in manipulacija s preizkušanci blizu temperaturi steklastega prehoda.

V zadnjem času je bilo podanih več inovativnih predlogov v zvezi s procesi inkrementalnega preoblikovanja, zlasti za izboljšanje preoblikovalnosti. Ena od predstavljenih možnosti je bila uporaba lokalnega ogrevanja pri inkrementalnem preoblikovanju titanovih zlitin in visokotrdnih jekel. Prav temperatura ima še posebej pomembno vlogo pri vedenju termoplastičnih materialov, saj vpliva na njihov steklasti prehod, fluidnost, morfologijo in degradacijo. Pričujoča študija analizira vpliv različnih parametrov (temperatura, koti sten, prehodi, elastični modul) na preoblikovanje biorazgradljive termoplastične matrice (blagovna znamka Solanyl), kombinirane z 10 odstotki kratkih lanenih vlaken dolžine največ 3 mm. Izkazalo se je, da je bila največja globina preoblikovanja dosežena v prisotnosti toplotnega vira v ogrevanem okolju (voda). Zabeležen je bil tudi potek sile (N) in temperature med nastajanjem stožčaste geometrije v procesu inkrementalnega preoblikovanja.

Izvedeni so bili eksperimenti za določitev najpomembnejših dejavnikov, ki vplivajo na celotno globino vdolbine po procesu inkrementalnega preoblikovanja. Rezultati so bili ovrednoteni z analizo variance (ANOVA), ki določa moč relacij med spremenljivkami. Odvisna spremenljivka je bila skupna globina, dosežena po procesu inkrementalnega preoblikovanja. Določiti je mogoče povezave med različnimi spremenljivkami za doseganje maksimalne globine vdolbine v foliji. Predstavljene informacije oblikujejo prvi model preoblikovanja kompozitnih materialov s termoplastično matrico. Rezultati osvetljujejo različne dejavnike in njihov prispevek pri preoblikovanju tovrstnih materialov, kot so npr. sile pri preoblikovanju. V prihodnjih študijah se bo mogoče posvetiti spremenljivkam v procesu preoblikovanja, ki vplivajo na dimenzijsko natančnost biokompatibilnih polimernih izdelkov za medicinske namene.

Ključne besede: inkrementalno preoblikovanje, biokompoziti, vročje preoblikovanje, analiza variance, deformacija

Guide for Authors

All manuscripts must be in English. Pages should be numbered sequentially. The manuscript should be composed in accordance with the Article Template given above. The maximum length of contributions is 12 pages (approx. 5000 words). Longer contributions will only be accepted if authors provide justification in a cover letter. For full instructions see the Information for Authors section on the journal's website: <http://en.sv-jme.eu>.

SUBMISSION:

Submission to SV-JME is made with the implicit understanding that neither the manuscript nor the essence of its content has been published previously either in whole or in part and that it is not being considered for publication elsewhere. All the listed authors should have agreed on the content and the corresponding (submitting) author is responsible for having ensured that this agreement has been reached. The acceptance of an article is based entirely on its scientific merit, as judged by peer review. Scientific articles comprising simulations only will not be accepted for publication; simulations must be accompanied by experimental results carried out to confirm or deny the accuracy of the simulation. Every manuscript submitted to the SV-JME undergoes a peer-review process.

The authors are kindly invited to submit the paper through our web site: <http://ojs.sv-jme.eu>. The Author is able to track the submission through the editorial process - as well as participate in the copyediting and proofreading of submissions accepted for publication - by logging in, and using the username and password provided.

SUBMISSION CONTENT:

The typical submission material consists of:

- A **manuscript** (A PDF file, with title, all authors with affiliations, abstract, keywords, highlights, inserted figures and tables and references),
 - Supplementary files:
 - a **manuscript** in a WORD file format
 - a **cover letter** (please see instructions for composing the cover letter)
 - a ZIP file containing **figures** in high resolution in one of the graphical formats (please see instructions for preparing the figure files)
 - possible **appendices** (optional), cover materials, video materials, etc.
- Incomplete or improperly prepared submissions will be rejected with explanatory comments provided. In this case we will kindly ask the authors to carefully read the Information for Authors and to resubmit their manuscripts taking into consideration our comments.

COVER LETTER INSTRUCTIONS:

Please add a **cover letter** stating the following information about the submitted paper:

1. Paper title, list of **authors** and their **affiliations**. **One** corresponding author should be provided.
2. **Type of paper**: original scientific paper (1.01), review scientific paper (1.02) or short scientific paper (1.03).
3. A **declaration** that neither the manuscript nor the essence of its content has been published in whole or in part previously and that it is not being considered for publication elsewhere.
4. State the **value of the paper** or its practical, theoretical and scientific implications. What is new in the paper with respect to the state-of-the-art in the published papers? Do not repeat the content of your abstract for this purpose.
5. We kindly ask you to suggest at least two **reviewers** for your paper and give us their names, their full affiliation and contact information, and their scientific research interest. The suggested reviewers should have at least two relevant references (with an impact factor) to the scientific field concerned; they should not be from the same country as the authors and should have no close connection with the authors.

FORMAT OF THE MANUSCRIPT:

The manuscript should be composed in accordance with the Article Template. The manuscript should be written in the following format:

- A **Title** that adequately describes the content of the manuscript.
- A list of **Authors** and their **affiliations**.
- An **Abstract** that should not exceed 250 words. The Abstract should state the principal objectives and the scope of the investigation, as well as the methodology employed. It should summarize the results and state the principal conclusions.
- 4 to 6 significant **key words** should follow the abstract to aid indexing.
- 4 to 6 **highlights**; a short collection of bullet points that convey the core findings and provide readers with a quick textual overview of the article. These four to six bullet points should describe the essence of the research (e.g. results or conclusions) and highlight what is distinctive about it.
- An **Introduction** that should provide a review of recent literature and sufficient background information to allow the results of the article to be understood and evaluated.
- A **Methods** section detailing the theoretical or experimental methods used.
- An **Experimental section** that should provide details of the experimental set-up and the methods used to obtain the results.
- A **Results** section that should clearly and concisely present the data, using figures and tables where appropriate.
- A **Discussion** section that should describe the relationships and generalizations shown by the results and discuss the significance of the results, making comparisons with previously published work. (It may be appropriate to combine the Results and Discussion sections into a single section to improve clarity.)
- A **Conclusions** section that should present one or more conclusions drawn from the results and subsequent discussion and should not duplicate the Abstract.
- **Acknowledgement** (optional) of collaboration or preparation assistance may be included. Please note the source of funding for the research.
- **Nomenclature** (optional). Papers with many symbols should have a nomenclature that defines all symbols with units, inserted above the references. If one is used, it must contain all the symbols used in the manuscript and the definitions should not be repeated in the text. In all cases, identify the symbols used if they are not widely recognized in the profession. Define acronyms in the text, not in the nomenclature.
- **References** must be cited consecutively in the text using square brackets [1] and collected together in a reference list at the end of the manuscript.
- **Appendix(-ies)** if any.

SPECIAL NOTES

Units: The SI system of units for nomenclature, symbols and abbreviations should be followed closely. Symbols for physical quantities in the text should be written in italics (e.g. v , T , n , etc.). Symbols for units that consist of letters should be in plain text (e.g. ms^{-1} , K, min, mm, etc.). Please also see: <http://physics.nist.gov/cuu/pdf/sp811.pdf>.

Abbreviations should be spelt out in full on first appearance followed by the abbreviation in parentheses, e.g. variable time geometry (VTG). The meaning of symbols and units belonging to symbols should be explained in each case or cited in a **nomenclature** section at the end of the manuscript before the References.

Figures (figures, graphs, illustrations digital images, photographs) must be cited in consecutive numerical order in the text and referred to in both the text and the captions as Fig. 1, Fig. 2, etc. Figures should be prepared without borders and on white grounding and should be sent separately in their original formats. If a figure is composed of several parts, please mark each part with a), b), c), etc. and provide an explanation for each part in Figure caption. The caption should be self-explanatory. Letters and numbers should be readable (Arial or Times New Roman, min 6 pt with equal sizes and fonts in all figures). Graphics (submitted as supplementary files) may be exported in resolution good enough for printing (min. 300 dpi) in any common format, e.g. TIFF, BMP or JPG, PDF and should be named Fig1.jpg, Fig2.tif, etc. However, graphs and line drawings should be prepared as vector images, e.g. CDR, AI. Multi-curve graphs should have individual curves marked with a symbol or otherwise provide distinguishing differences using, for example, different thicknesses or dashing.

Tables should carry separate titles and must be numbered in consecutive numerical order in the text and referred to in both the text and the captions as Table 1, Table 2, etc. In addition to the physical quantities, such as t (in italics), the units [s] (normal text) should be added in square brackets. Tables should not duplicate data found elsewhere in the manuscript. Tables should be prepared using a table editor and not inserted as a graphic.

REFERENCES:

A reference list must be included using the following information as a guide. Only cited text references are to be included. Each reference is to be referred to in the text by a number enclosed in a square bracket (i.e. [3] or [2] to [4] for more references; do not combine more than 3 references, explain each). No reference to the author is necessary.

References must be numbered and ordered according to where they are first mentioned in the paper, not alphabetically. All references must be complete and accurate. Please add DOI code when available. Examples follow.

Journal Papers:

Surname 1, Initials, Surname 2, Initials (year). Title. Journal, volume, number, pages, DOI code.

- [1] Hackenschmidt, R., Alber-Laukant, B., Rieg, F. (2010). Simulating nonlinear materials under centrifugal forces by using intelligent cross-linked simulations. *Strojniški vestnik - Journal of Mechanical Engineering*, vol. 57, no. 7-8, p. 531-538, DOI:10.5545/sv-jme.2011.013.

Journal titles should not be abbreviated. Note that journal title is set in italics.

Books:

Surname 1, Initials, Surname 2, Initials (year). Title. Publisher, place of publication.

- [2] Groover, M.P. (2007). *Fundamentals of Modern Manufacturing*. John Wiley & Sons, Hoboken.

Note that the title of the book is italicized.

Chapters in Books:

Surname 1, Initials, Surname 2, Initials (year). Chapter title. Editor(s) of book, book title. Publisher, place of publication, pages.

- [3] Carbone, G., Ceccarelli, M. (2005). Legged robotic systems. Kordić, V., Lazinica, A., Merdan, M. (Eds.), *Cutting Edge Robotics*. Pro literatur Verlag, Mammendorf, p. 553-576.

Proceedings Papers:

Surname 1, Initials, Surname 2, Initials (year). Paper title. Proceedings title, pages.

- [4] Štefanić, N., Martinčević-Mikić, S., Tošanović, N. (2009). Applied lean system in process industry. *MOTSP Conference Proceedings*, p. 422-427.

Standards:

Standard-Code (year). Title. Organisation. Place.

- [5] ISO/DIS 16000-6.2:2002. *Indoor Air - Part 6: Determination of Volatile Organic Compounds in Indoor and Chamber Air by Active Sampling on TENAX TA Sorbent, Thermal Desorption and Gas Chromatography using MSD/FID*. International Organization for Standardization. Geneva.

WWW pages:

Surname, Initials or Company name. Title, from <http://address>, date of access.

- [6] Rockwell Automation. Arena, from <http://www.arenasimulation.com>, accessed on 2009-09-07.

EXTENDED ABSTRACT:

When the paper is accepted for publishing, the authors will be requested to send an **extended abstract** (approx. one A4 page or 3500 to 4000 characters or approx. 600 words). The instruction for composing the extended abstract are published on-line: <http://www.sv-jme.eu/information-for-authors/>.

COPYRIGHT:

Authors submitting a manuscript do so on the understanding that the work has not been published before, is not being considered for publication elsewhere and has been read and approved by all authors. The submission of the manuscript by the authors means that the authors automatically agree to transfer copyright to SV-JME when the manuscript is accepted for publication. All accepted manuscripts must be accompanied by a Copyright Transfer Agreement, which should be sent to the editor. The work should be original work by the authors and not be published elsewhere in any language without the written consent of the publisher. The proof will be sent to the author showing the final layout of the article. Proof correction must be minimal and executed quickly. Thus it is essential that manuscripts are accurate when submitted. Authors can track the status of their accepted articles on <http://en.sv-jme.eu/>.

PUBLICATION FEE:

Authors will be asked to pay a publication fee for each article prior to the article appearing in the journal. However, this fee only needs to be paid after the article has been accepted for publishing. The fee is 380 EUR (for articles with maximum of 6 pages), 470 EUR (for articles with maximum of 10 pages), plus 50 EUR for each additional page. The additional cost for a color page is 90.00 EUR (only for a journal hard copy; optional upon author's request). These fees do not include tax.

Strojniški vestnik - Journal of Mechanical Engineering
Aškerčeva 6, 1000 Ljubljana, Slovenia, e-mail: info@sv-jme.eu



<http://www.sv-jme.eu>

Contents

Papers

- 75 Yong Wang, Xiaolin Wang, Zilong Zhang, Yu Li, Houlin Liu, Xiang Zhang, Marko Hočevar:
Optimization of a Self-Excited Pulsed Air-Water Jet Nozzle Based on the Response Surface Methodology
- 88 Manuel Javier Rosel Solis, José Omar Dávalos Ramírez, Javier Molina Salazar, Juan Antonio Ruiz Ochoa, Antonio Gómez Roa:
Optimization of Running Blade Prosthetics Utilizing Crow Search Algorithm Assisted by Artificial Neural Networks
- 101 Omar Dávalos, Uzziel Caldiño-Herrera, Delfino Cornejo-Monroy, Oscar Tenango-Pirin, Juan Carlos García, M.A. Basurto-Pensado:
Reduction of Stresses and Mass of an Engine Rubber Mount Subject to Mechanical Vibrations
- 114 Bin Wang, Chenxiao Yan, Jubo Li, Peiyao Feng, Shuaipu Wang, Shuo Chen, Jianxin Su:
Residual Stress and Deformation Analysis in Machining Split Straight Bevel Gears
- 123 Sandino Torres, Roberto Ortega, Pablo Acosta, Edisson Calderón:
Hot Incremental Forming of Biocomposites Developed from Linen Fibres and a Thermoplastic Matrix